Remote Sensing of Inherent and Apparent Optical Properties in Optically Complex Shelf Seas

Catherine Mitchell

Department of Physics

University of Strathclyde

A thesis submitted to the University of Strathclyde in accordance with the requirements for the degree of Doctor of Philosophy.

Declaration

This thesis is the result of the authors original research. It has been composed by the author and has not been previously submitted for examination which has led to the award of a degree.

Signed:

Date:

Abstract

Variability in the patterns of ocean colour is frequently observed in shelf seas, where a combination of phytoplankton cells, mineral particles and coloured dissolved organic matter are driving the optical properties of the water column. Understanding the contributions of each material to the total optical properties is essential for understanding and monitoring the processes which affect shelf sea ecosystems. Lee et al. (2002, 2005b, 2007, 2009, 2013) developed a method for the recovery of the absorption, backscattering and mean diffuse attenuation coefficients and the euphotic depth from the remote sensing reflectance. Using the Irish Sea as a study site, the procedure of Lee et al. and two empirical methods for recovering the euphotic depth (Cunningham et al., 2013 and Zhao et al., 2013), were evaluated. The methods were initially adjusted based on a regional bio-optical model, then validated against field data with excellent recoveries of all parameters. By considering the backscattering to absorption ratios of phytoplankton and mineral particles, a new method for separating the total absorption coefficient recovered by the quasi-analytical algorithm into the phytoplankton and mineral components was developed. Application of this method to the bio-optical model created for the Irish Sea recovered phytoplankton and mineral absorption coefficients which were well correlated with the modelled values. The sensitivity of the absorption partitioning procedure to the assumption made about CDOM variability was evaluated, demonstrating the phytoplankton and mineral absorption coefficients could be recovered within the Irish Sea with root mean square errors of 0.02 m^{-1} and 0.009 m^{-1} respectively. The inversion methods developed

and validated were applied to eight years of MODIS data. This showed both spatial and temporal variability for all parameters, which corresponded to different mixing regimes and were explained in terms of phytoplankton cells and mineral particles. The results obtained from the satellite imagery have demonstrated that optical remote sensing can be used to provide an insight into shelf sea ecosystems.

Contents

List of Tables

List of Figures

Publications

Mitchell, C., and Cunningham, A., (2015). Remote sensing of spatio-temporal relationships between the partitioned absorption coefficients of phytoplankton cells and mineral particles and euphotic zone depths in a partially mixed shelf sea. *Remote Sensing of Environment*, doi:10.1016/j.rse.2015.01.015

Mitchell, C., Cunningham, A., and McKee, D. (2014b). Remote sensing of particulate absorption coefficients and their biogeochemical interpretation: A case study in the Irish Sea. *Remote Sensing of Environment*, 152,74 - 82.

Mitchell, C., Cunningham, A., and McKee, D. (2014a). Remote sensing of shelf sea optical properties: Evaluation of a quasi-analytical approach for the Irish Sea. *Remote Sensing of Environment*, 143,142 – 153.

Acknowledgements

I would like to take this opportunity to thank the people who have helped me throughout my PhD. Firstly, to my supervisor, Prof. Alex Cunningham who has supported and guided me from the first day I stepped into his office, I couldn't have got through it without you. To Dr. David McKee, for always shining a different light on discussions and always attempting to lighten the mood with his humour. To all the PhD and project students from the Marine Optics and Remote Sensing Group who I have shared my time, be it in the office, lab or eating cake, especially to Ina for accompanying me for countless trips upstairs for a cup of tea.

I would like to thank my family, who have continually supported me from when I first left the farm to come to Glasgow. Mum and Dad, thank you for all the support you have given me through university and providing a good two-week distraction from studies by insisting on my presence for lambing time. To Peter, for the numerous rugby outings and the times we have spent together (whilst not bickering) which have added fun to my weekends. To Rachel, for your company in Glasgow and infectious laughter which always makes things seem better.

Finally, to Mike, who provided endless distractions (from boardgames to climbing and camping trips), accompanied me on adventures out of Glasgow when the farm seemed so far away and for always giving me a hug and making me smile when I needed it. Thank you.

1. Introduction

Background

Shelf seas and shallower coastal waters are highly productive regions, providing approximately 90% of the global fish catch and 25% of the marine primary production (Robinson et al., 2008). With over half the population living within the coastal zone, shelf seas provide a major resource for fisheries, recreation and tourism. However, the proximity of shelf seas to the land leads to increased pressures on the marine environments and these are consequently among the most endangered areas. Pressures include, land use and river run-off altering mineral and nutrient levels which can affect biogeochemical cycles (Tang et al., 2005; Chen et al., 2007), the resuspension of sediments into the surface layer due to coastal developments (Song and Wang, 2013) and eutrophication of the water column (Druon et al., 2004). Therefore, understanding and monitoring these processes is important for predicting how the marine ecosystems will be affected and respond to external impacts, and for the conservation and management of the coastal zone which is important for the human population.

The sun provides energy to marine ecosystems, sustaining phytoplankton, the first link in the oceanic food web. The solar radiation which reaches the earth is mainly in the visible and infrared regions of the electromagnetic spectrum. However, as water is nearly opaque to infrared radiation, it is the visible wavelengths which are important for marine photosynthesis (Bisset et al., 2001). As light propagates through the water, it is absorbed and scattered by phytoplankton and other microscopic material present, altering the underwater light field and

the colour of the water (Yentsch, 1960; Morel and Prieur, 1977; Gordon et al., 1988). Therefore measurements of the spectral shape of the light which has been scattered out of the water column can provide an insight into the materials present in the water. The measurement of the emergent light, or the colour of the water, can be done using remote platforms such as aircrafts or satellites and is known as ocean colour remote sensing (IOCCG, 2000, 2008).

One of the major advantages of using satellites to monitor ocean colour is that they provide almost daily coverage of the planet, allowing variability in ocean colour to be measured at high temporal and spatial scales compared to field campaigns aboard ships. The first satellite launched for the purpose of monitoring ocean colour was the Coastal Zone Color Scanner (CZCS), in 1978. This was a "proof-of-concept" mission, the main objective of which was to determine if different organic and non-organic materials could be identified and quantified using ocean colour (NASA, 1996). Due to the success of this mission and the early studies and algorithms developed to interpret the satellite imagery, further missions were launched (Mitchell, 1994) providing constant coverage since the launch of NASA's SeaWiFS in 1997. Currently, both ESA and NASA have missions in planning, with ESA's Sentinel-3 due to be launched in 2015, which are set to provide ocean colour data for the foreseeable future.

The initial movement in ocean colour research was aimed at measuring chlorophyll concentrations as an indicator of phytoplankton biomass in the open oceans (Smith and Baker, 1982; Feldman et al., 1984). This soon expanded into the estimation of different biogeochemical and optical properties, linking these to solar heating (Lewis et al., 1990) and primary production (Sathyendranath et al., 1991b) in the oceans. These ocean basin waters, where all the optically significant materials present co-vary with phytoplankton, are known as Case-1 waters

(Morel and Prieur, 1977) and the algorithms developed to interpret the signals measured via satellite were based on this assumption of co-variance (Morel, 1980; Gordon et al., 1988; Sathyendranath et al., 1989a). However, shelf sea waters are optically complex and classified as Case-2 due to the presence of material and sediments which do not co-vary with the phytoplankton biomass. These additional materials significantly alter the optical signals from those typically found in open oceans, causing large variability in the optical properties of the water column (Babin et al., 2003; McKee and Cunningham, 2006; Oubelkheir et al., 2006; Aurin et al., 2010). Due to these optical complexities, the traditional algorithms developed for Case-1 waters tend to fail when applied to Case-2 waters (Morel, 1980; Carder et al., 1991).

Much progress has been made in the development of different methods for the analysis of ocean colour in Case-2 waters (Roesler et al., 1989; Garver and Siegel, 1997; Carder et al., 1999; Maritorena et al., 2002; Lee et al., 2002). However, even with this improvement, the accurate retrieval of the concentrations of suspended mineral particles, phytoplankton and coloured dissolved organic matter is still a major problem in coastal waters (Aurin and Dierssen, 2012; Odermatt et al., 2012). The alternative approach of retrieving the optical properties of the water column, which are dependent on the material concentrations, has therefore gained more focus. Optical properties can be used to provide valuable insights into marine environments, including:

i) The derivation of further properties of the water column, including the depth of penetration of light which is available for photosynthesis (Cunningham et al., 2013),
ii) Estimations of phytoplankton concentrations in regions where mineral par-

ticles degrade the traditional algorithms (Tilstone et al., 2012),

iii) Derivations of phytoplankton absorption for primary production calculations (Barnes et al., 2014),

iv) Estimations of the contribution of individual materials to the optical properties (Le et al., 2013),

v) The effect of freshwater mixing on underwater light distributions in coastal waters (Cherukuru et al., 2014).

Thesis Aims

The aim of this thesis is to interpret ocean colour signals in optically complex environments, with the Irish Sea and surrounding waters chosen as a study site. This study will concentrate on the retrieval of inherent and apparent optical properties of the water column rather than the retrieval of the concentrations of the main optically significant materials. In particular, the following questions will be addressed:

1. Can ocean colour remote sensing be used in Case-2 shelf seas to quantitatively measure the optical properties of the water column?

2. Can methods for identifying different particle types, such as suspended minerals and phytoplankton cells, be developed?

3. Can the role of different types of particle on the attenuation of light in the water column be determined?

4. Can ocean colour data be used to determine the temporal and spatial variability of optical properties in shelf seas, providing insights into the underlying physical dynamics of the region?

The Irish Sea

The Irish Sea is a semi-enclosed sea on the European shelf bounded by Great Britain to the east, Ireland to the west and the Celtic Sea to the south (Figure 1.1). A deep trench runs approximately north to south, from the North Channel, west of the Isle of Man, through the St George's Channel towards the Celtic Sea, with a depth of approximately 100 m. The eastern Irish Sea is shallower, with depths generally less than 50 m. These shallower eastern waters receive the majority of the freshwater river input from Liverpool and Morecambe Bays, and consequently are the waters with lowest salinity (Bowers et al., 2013; Gowen et al., 2008).

The Irish Sea is generally well-mixed through the winter by wind and tidal stirring (Bowers, 2003) with regions of seasonal stratification forming over the summer (Simpson and Hunter, 1974). In the deep channel west of the Isle of Man, the tidal flows are weakest across the whole region and thermal stratification occurs typically from late April/early May for approximately four to five months (Gowen et al., 1995), with the transition from the stratified to the fully mixed waters marked by a front (Simpson and Hunter, 1974). In the eastern Irish Sea, Simpson (1997) observed intermittent freshwater-induced stratification. The Celtic Sea stratifies over the summer months and the boundary between the southern Irish Sea and northern Celtic Sea is indicated by a prominent front across St George's Channel (Simpson and Bowers, 1981).

Gowen et al. (1995) studied the effect of the different mixing regimes in the Irish Sea on phytoplankton growth, demonstrating the effects of a fully mixed water column and a stratified water column on the production season of phytoplankton. In particular, they noted nutrient availability, rather than light availability

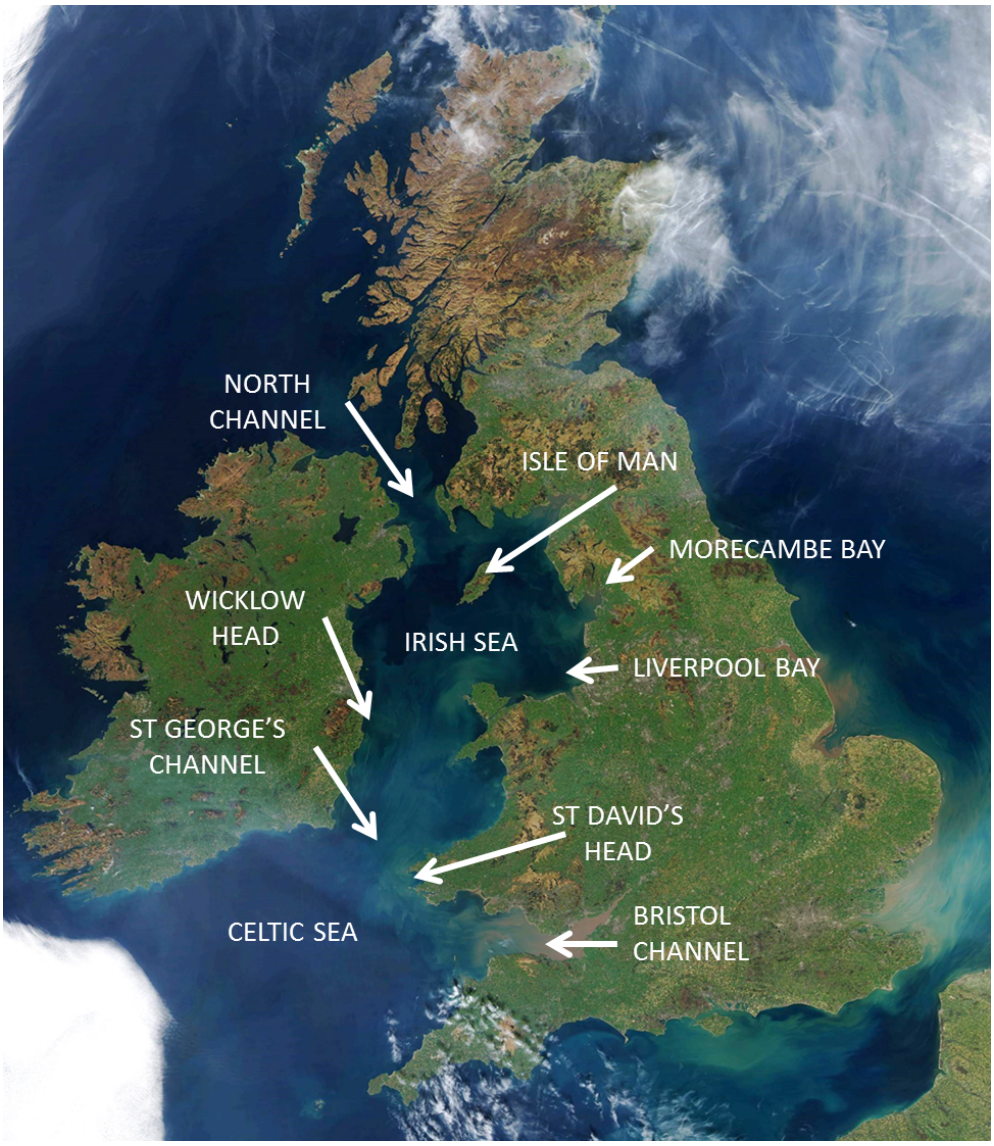

Figure 1.1: The Irish Sea and surrounding waters. Image courtesy of NERC Satellite Receiving Station, Dundee University, Scotland, http://www.sat.dundee.ac.uk/.

limits phytoplankton growth in the summer stratified regions.

Satellite imagery of the Irish Sea has revealed three patches which have consistently higher reflectance than neighbouring regions (Weeks and Simpson, 1991; Bowers et al., 1998, 2005). Ship based surveys have shown that the high reflectance patches correspond to elevated levels of suspended particulate matter throughout the year, with suspended particulate matter concentrations reaching 2 to 3 times the concentrations observed in the rest of the Irish Sea during the winter months (Bowers et al., 2002). The locations of the turbidity maxima correspond to the areas of highest tidal currents: off the north west coast of Anglesey, the eastern Irish coast at Wicklow Head, and the south-west tip of Wales at St David's Head. There is no source of fine sediment near Anglesey to keep up a continual supply of suspended particles. However, Bowers et al. (2005) postulated the net movement of finer particles out of the turbidity maxima, and larger aggregated particles into the region. These aggregated particles, or flocs, are groups of mineral sediments held together by organic material. Flocs can form when particles are brought together in relatively low levels of turbulence, however as the turbulence increases, the flocs break-up. Modelling studies of Bowers et al. (2005) and Ellis et al. (2008) demonstrated how the high tidal currents in these regions can break-up the aggregates which are brought into these regions, potentially providing the source of fine sediment causing the turbidity maxima.

Changes in the optical properties of the Irish Sea are driven predominately by phytoplankton and mineral particles and coloured dissolved organic matter (CDOM). Gowen et al. (2008) observed concentrations of phytoplankton chlorophyll ranging from <0.1 mg m^{-3} to approximately 16 mg m^{-3} with means of 3.4 mg m^{-3} in western coastal waters, 2.2 mg m^{-3} in western offshore waters and 1.8 mg m^{-3} in eastern offshore waters. These findings were consistent with McKee

and Cunningham (2006) who found relatively low levels of phytoplankton during extensive sampling of mostly offshore waters, with 90% of their chlorophyll samples below 2 mg m^{-3}. However, during the spring bloom, the concentrations of chlorophyll inshore does reach significantly higher levels, often reaching approximately 30 mg m^{-3} in Liverpool Bay (Gowen et al., 2008).

The measurements of McKee and Cunningham (2006) also showed the concentration of suspended mineral solids to be generally below 14 g m^{-3}, with the most observations < 4 g m^{-3}, and the absorption of CDOM at 440 nm to be no higher than 0.25 m^{-1}, with the most occurrences in the range of 0.1 - 0.15 m^{-1}. This is slightly lower than Bowers et al. (2013), who found the mean absorption of CDOM at 440 nm in the Irish Sea to be 0.17 m^{-1} with a standard deviation of 0.02 m^{-1}.

Due to the range of optical and hydrological properties, including concentrations of phytoplankton and the seasonal patterns of mixing and stratification, the Irish Sea is an ideal study site for testing remote sensing methods in shelf seas.

Thesis Structure

Chapter 2 gives an overview of the relevant optical theory, covering three main areas. The first is a discussion on the optical properties of the water column and how these affect the underwater light field. The second is an overview of satellite remote sensing. Finally, different inversion methods are reviewed, with particular focus on the quasi-analytical approach of Lee et al. (2002, 2005b, 2007, 2009).

Chapter 3 introduces the main methods used throughout this study. The first part of this Chapter focuses on the acquisition of field data and the processing required to obtain the relevant properties. This is followed by a discussion on how

the inherent optical properties and resultant light fields are modelled for algorithm validation and development. The programs and methods used to process and analyse satellite data are covered in the last part of the Chapter.

In Chapter 4, the quasi-analytical algorithm of Lee et al. (2002, 2009), which aims to retrieve the spectral absorption and backscattering coefficients from the remote sensing reflectance, is evaluated on a bio-optical model of the Irish Sea. The algorithms are adjusted to improve performance in the Irish Sea and these new versions are validated against field data. Three semi-analytical algorithms which recover the diffuse attenuation coefficient, and three algorithms which estimate the euphotic depth, are also validated using the Irish Sea field data.

A method for estimating the absorption coefficient for phytoplankton cells and mineral particles from the total absorption and backscattering coefficients is developed in Chapter 5. Using these inherent optical properties as a starting point allows this procedure to be appended to the quasi-analytical algorithm, ultimately estimating the separate particulate contributions to the total absorption coefficient from remote sensing. The procedure is initially tested on modelled data and the procedure's sensitivity to the assumptions made in its development are evaluated. The inherent optical properties derived from satellite data for the Irish Sea are examined and the absorption partitioning technique is applied to investigate the temporal variability observed in the total absorption of the water column.

In Chapter 6, the inversion methods developed and validated in Chapters 4 and 5 are applied to eight years of satellite acquired remote sensing reflectance data from the Irish Sea. Furthermore, these methods are extended to estimate the contribution of phytoplankton and mineral particles to the attenuation of light in the water column. The time series at three different locations are considered

to investigate the temporal variability and seasonality of the different parameters and particle classes. Monthly composite maps of the whole region are determined to show the spatial variability, and how this can change for different months.

Finally, Chapter 7 outlines the main conclusions drawn from this investigation, with suggestions of future work.

All symbols and terms frequently used throughout this thesis are listed in Table 1.1.

Symbol	**Definition**	**Units**
$a(\lambda)$	absorption coefficient at wavelength λ	m^{-1}
$a_{\mathrm{CDOM}}(\lambda)$	absorption coefficient for CDOM at wavelength λ	m^{-1}
$a_{\mathrm{CHL}}(\lambda)$	absorption coefficient for phytoplankton cells at wavelength λ	m^{-1}
$a_{\mathrm{MSS}}(\lambda)$	absorption coefficient for mineral particles at wavelength λ	m^{-1}
$a^*_{\mathrm{CDOM}}(\lambda)$	mass specific absorption coefficient for CDOM at wavelength λ	dimensionless
$a^*_{\mathrm{CHL}}(\lambda)$	mass specific absorption coefficient for phytoplankton cells at wavelength λ	$m^2\ mg^{-1}$
$a^*_{\mathrm{MSS}}(\lambda)$	mass specific absorption coefficient for mineral particles at wavelength λ	$m^2\ g^{-1}$
$a_{nw}(\lambda)$	non-water absorption coefficient at wavelength λ	m^{-1}
$a_w(\lambda)$	absorption coefficient for water at wavelength λ	m^{-1}
AOP	apparent optical property	-
$b(\lambda)$	scattering coefficient at wavelength λ	m^{-1}
$b_f(\lambda)$	forward scattering coefficient at wavelength λ	m^{-1}
$b_b(\lambda)$	backscattering coefficient at wavelength λ	m^{-1}
$b_{b\mathrm{CHL}}(\lambda)$	backscattering coefficient for phytoplankton cells at wavelength λ	m^{-1}

Table 1.1: Definitions of the symbols and terms used throughout this thesis.

Symbol	Definition	Units
$b_{b\mathrm{MSS}}(\lambda)$	backscattering coefficient for mineral particles at wavelength λ	m^{-1}
$b^*_{b\mathrm{CHL}}(\lambda)$	mass specific backscattering coefficient for phytoplankton cells at wavelength λ	$\mathrm{m}^2\ \mathrm{mg}^{-1}$
$b^*_{b\mathrm{MSS}}(\lambda)$	mass specific backscattering coefficient for mineral particles at wavelength λ	$\mathrm{m}^2\ \mathrm{g}^{-1}$
$b_{bp}(\lambda)$	particulate backscattering coefficient at wavelength λ	m^{-1}
$b_{bw}(\lambda)$	backscattering coefficient for water at wavelength λ	m^{-1}
$c(\lambda)$	attenuation coefficient at wavelength λ	m^{-1}
[CDOM]	concentration of coloured dissolved organic matter (CDOM) at $a(440)$	m^{-1}
[CHL]	concentration of chlorophyll-a	$\mathrm{mg\ m}^{-3}$
$E_d(\lambda, z)$	downwelling planar irradiance at wavelength λ and depth z	$\mathrm{Wm}^{-2}\ \mathrm{nm}^{-1}$
$E_u(\lambda, z)$	upwelling planar irradiance at wavelength λ and depth z	$\mathrm{Wm}^{-2}\ \mathrm{nm}^{-1}$
IOP	inherent optical property	-
$K_d(\lambda, z)$	the diffuse attenuation coefficient for the downwelling planar irradiance at wavelength λ and depth z	m^{-1}
$\overline{K}_d(\lambda, z_1 \leftrightarrow z_2)$	the mean (or depth-averaged) diffuse attenuation coefficient for the downwelling planar irradiance between depths z_1 and z_2 at wavelength λ	m^{-1}
$L(\lambda, z, \theta, \phi)$	radiance at wavelength λ, depth z, zenith angle θ and azimuthal angle ϕ	$\mathrm{Wm}^{-2}\ \mathrm{sr}^{-1}\ \mathrm{nm}^{-1}$
$L_u(\lambda)$	below surface upward radiance at wavelength λ	$\mathrm{Wm}^{-2}\ \mathrm{sr}^{-1}\ \mathrm{nm}^{-1}$
$L_w(\lambda)$	water leaving radiance at wavelength λ	$\mathrm{Wm}^{-2}\ \mathrm{sr}^{-1}\ \mathrm{nm}^{-1}$
[MSS]	concentration of mineral suspended solids	$\mathrm{g\ m}^{-3}$
PAR	photosynthetically available radiation	photons $\mathrm{m}^{-2}\ \mathrm{s}^{-1}$

Table 1.1 (Continued): Definitions of the symbols and terms used throughout this thesis.

Symbol	Definition	Units
$R(z,\lambda)$	irradiance reflectance = $E_u(z,\lambda)/E_d(z,\lambda)$	dimensionless
$R_{rs}(\lambda)$	above surface remote sensing reflectance = $L_w(\lambda)/E_d(\lambda)$	sr^{-1}
$r_{rs}(\lambda)$	subsurface remote sensing reflectance = $L_u(\lambda)/E_d(\lambda)$	sr^{-1}
Z_{eu}	euphotic depth = depth at which PAR falls to 1% of its surface value	m
κ_{CHL}	fractional contribution of phytoplankton cells to the mean diffuse attenuation coefficient	dimensionless
κ_{MSS}	fractional contribution of mineral particles to the mean diffuse attenuation coefficient	dimensionless
$\rho_1(\lambda)$	the ratio of the backscattering to absorption coefficients for mineral particles at wavelength λ	dimensionless
$\rho_2(\lambda)$	the ratio of the backscattering to absorption coefficients for phytoplankton cells at wavelength λ	dimensionless

Table 1.1 (Continued): Definitions of the symbols and terms used throughout this thesis.

2. Optical Theory

2.1 Basic Principles

Ocean colour remote sensing involves inferring information about the composition of the water column from the light leaving the water body, relying on knowledge of radiative transfer processes in the water column. Radiative transfer theory describes how the composition of a medium affects the propagation of light through the medium. Hence an understanding of both the optical properties of water and the geometric nature of light itself is needed. Natural waters contain a mix of dissolved and particulate matter, which can have a significant effect on the underwater light field. These materials, known as optically significant materials, effect the bulk optical properties of the water column, which are grouped into two classes: the inherent and apparent optical properties (Preisendorfer, 1976). The inherent optical properties are those which depend solely on the composition of the water body, whereas the apparent optical properties depend on both the water body composition and the light field.

The theory outlined in the next few sections follows that of Mobley (1994), unless otherwise stated.

Radiometery

In optical oceanography, the radiance is a fundamental parameter for describing the light field. The amount of radiant energy (Q), per unit area (A), per unit

solid angle (Ω), within a water body is defined as the radiance,

$$L(\lambda, z, \theta, \phi) = \frac{\mathrm{d}^3 Q}{\mathrm{d}A \mathrm{d}\Omega \mathrm{d}\lambda} \tag{2.1}$$

$$\text{Units} : \mathrm{Wm}^{-2}\mathrm{sr}^{-1}\mathrm{nm}^{-1}$$

for a particular wavelength (λ), depth (z), and zenith (θ) and azimuthal (ϕ) angles of the incoming light. The downwelling ($E_d(\lambda, z)$) and upwelling ($E_u(\lambda, z)$) irradiance are then defined as the light from all angles travelling in the downward or upward direction respectively, per unit area:

$$E_d(\lambda, z) = \int_{\phi=0}^{2\pi} \int_{\theta=0}^{\pi/2} L(\lambda, z, \theta, \phi) \cos\theta \sin\theta \ \mathrm{d}\theta \mathrm{d}\phi \tag{2.2}$$

$$E_u(\lambda, z) = \int_{\phi=0}^{2\pi} \int_{\theta=\pi/2}^{\pi} L(\lambda, z, \theta, \phi) \cos\theta \sin\theta \ \mathrm{d}\theta \mathrm{d}\phi \tag{2.3}$$

$$\text{Units} : \mathrm{Wm}^{-2}\mathrm{nm}^{-1}$$

The $\cos\theta$ term arises from the cosine law for irradiance, which states that a beam of photons hitting a plane surface produces an irradiance that is proportional to the cosine of the angle between the photon direction and the normal to the surface.

Inherent Optical Properties (IOPs)

As light travels through a small volume of water, some of the incident radiant power (Φ_i) is absorbed within the volume of water (Φ_a) and some is scattered out of the beam path (Φ_b), leaving any remaining power to be transmitted through the sample. The absorption coefficient is defined as the limit of the fraction of incident power which is absorbed within the water volume as the thickness of the

sample (i.e. the length of the beam path, Δr) approaches zero,

$$a(\lambda) = \lim_{\Delta r \to 0} \frac{\Phi_a / \Phi_i}{\Delta r} \tag{2.4}$$

Units : m^{-1}

The scattering coefficient is similarly defined:

$$b(\lambda) = \lim_{\Delta r \to 0} \frac{\Phi_b / \Phi_i}{\Delta r} \tag{2.5}$$

Units : m^{-1}

with the attenuation coefficient the sum of the two,

$$c(\lambda) = a(\lambda) + b(\lambda). \tag{2.6}$$

By considering the angular distribution of the scattered radiant power in the water volume, another inherent optical property can be defined: the volume scattering function. For the fraction of incident power which was scattered out of the beam path at an angle of (θ, ϕ), into a solid angle, $\Delta\Omega$, the volume scattering function is expressed as,

$$\beta(\theta, \phi, \lambda) = \lim_{\Delta r \to 0} \lim_{\Delta\Omega \to 0} \frac{\Phi_b / \Phi_i}{\Delta r \Delta\Omega} \tag{2.7}$$

Units : $\mathrm{m}^{-1}\mathrm{sr}^{-1}$

Therefore, by integrating $\beta(\theta, \phi, \lambda)$ over all directions (all solid angles), we obtain the scattering coefficient, which can be expressed as

$$b(\lambda) = \int_{\Xi} \beta(\theta, \phi, \lambda)\ \mathrm{d}\Omega(\theta, \phi) = 2\pi \int_0^{\pi} \beta(\theta, \phi, \lambda) \sin\theta\ \mathrm{d}\theta. \tag{2.8}$$

It is often useful to think of the scattered light in terms of the overall direction in which it was scattered, allowing the scattering coefficient to be split into two parts, the forward scattering coefficient ($b_f(\lambda)$) and the backward scattering (or backscattering) coefficient ($b_b(\lambda)$),

$$b_f(\lambda) = 2\pi \int_0^{\pi/2} \beta(\theta, \phi, \lambda) \sin\theta \, \mathrm{d}\theta \tag{2.9}$$

$$b_b(\lambda) = 2\pi \int_{\pi/2}^{\pi} \beta(\theta, \phi, \lambda) \sin\theta \, \mathrm{d}\theta. \tag{2.10}$$

These bulk inherent optical properties (IOPs) describe the combined effects of the water and all the individual constituents present in the water column. The particulate material can either be phytoplankton cells, inorganic suspended sediments or non-phytoplankton organic particles. The phytoplankton component consists of all the different species, with the main pigment, chlorophyll-a, used as an indicator to phytoplankton biomass. Sediments suspended in the surface layer of the water column can be fine mineral particles such as slit and clay, or larger groups known as flocs, which consist of inorganic particles bound together by organic material. Previous studies have shown, compared to the phytoplankton cells and inorganic sediments, the non-phytoplankton organic materials may have a negligible effect on the total absorption and scattering in shelf seas (Bowers and Mitchelson-Jacob, 1996). In addition to the marine particles, dissolved particles affect the water colour. In particular, coloured dissolved organic matter originating from decaying phytoplankton and terrestrial sources can make the water yellow in colour. Hence, the main optically significant materials can be classified into these three main sources (IOCCG, 2000)

1. phytoplankton, conventionally as chlorophyll-a concentration (CHL),
2. mineral suspended solids (MSS), and

3. coloured dissolved organic matter (CDOM).

Each of theses materials absorb and scatter light in a different manner. Phytoplankton are strong absorbers of light, particularly in the blue and red wavelengths, and weakly scatter light. Whereas, suspended sediment particles are strong scatterers of light but do absorb, particularly in the blue. CDOM is dissolved in the water column and is a strong absorber, especially in the shorter wavelengths, however the scattering due to CDOM is a small proportion of the total scattering in coastal waters and is often taken as negligible (Kirk, 1994; Mobley, 1994).

The bulk IOPs are simply the sum of the contributions from all the different optically significant materials and water itself:

$$a(\lambda) = a_w(\lambda) + a_{\mathrm{CHL}}(\lambda) + a_{\mathrm{MSS}}(\lambda) + a_{\mathrm{CDOM}}, \tag{2.11}$$

$$b(\lambda) = b_w(\lambda) + b_{\mathrm{CHL}}(\lambda) + b_{\mathrm{MSS}}(\lambda), \tag{2.12}$$

$$b_b(\lambda) = b_{bw}(\lambda) + b_{b\mathrm{CHL}}(\lambda) + b_{b\mathrm{MSS}}(\lambda), \tag{2.13}$$

where the subscripts CHL, MSS and CDOM represent the IOP for each constituent, and w represents the water component.

Apparent Optical Properties (AOPs)

Reflectances

Reflectances are useful apparent optical properties in ocean colour remote sensing as they provides a measure of how much of the downwelling light eventually leaves the water surface. The irradiance reflectance is defined as the ratio

of upwelling to downwelling planar irradiances,

$$R(z,\lambda) = \frac{E_u(z,\lambda)}{E_d(z,\lambda)}. \tag{2.14}$$

The irradiance reflectance is often determined just below the surface, whereas a second ratio, remote sensing reflectance (R_{rs}), is usually evaluated just above the water surface. The remote sensing reflectance is defined as the ratio of water-leaving radiance (the radiance emerging from the water surface in a particular direction) to the downwelling planar irradiance,

$$R_{rs}(\theta,\phi,\lambda) = \frac{L_w(0^+,\theta,\phi,\lambda)}{E_d(0^+,\lambda)}, \tag{2.15}$$

Units : sr^{-1}

where 0^+ represents the position just above the surface. The remote sensing reflectance can also be considered just beneath the water's surface, at depth $z = 0^-$, and in this case is denoted r_{rs} to distinguish it from R_{rs}. The two ratios, R and R_{rs}, are related by the factor Q, which is the ratio of the water-leaving radiance to the upwelling planar irradiance. Taking both just above the surface ($z = 0^+$) and dropping the z argument for brevity,

$$R_{rs}(\lambda) = Q(\lambda)R(\lambda) = \frac{L_w(\lambda)}{E_u(\lambda)}\frac{E_u(\lambda)}{E_d(\lambda)}. \tag{2.16}$$

Diffuse Attenuation Coefficients

The diffuse attenuation coefficients describe how light in the water column decreases with depth. Typically, the downward radiances and irradiances decrease exponentially with depth, and each has a diffuse attenuation coefficient asso-

ciated with it, for example, the diffuse attenuation coefficient for downwelling planar irradiance, $K_d(z, \lambda)$ and the diffuse attenuation coefficient for radiance, $K(z, \lambda, \theta, \phi)$. The diffuse attenuation coefficient for, say the downwelling planar irradiance $K_d(z, \lambda)$, at depth z from the surface, is defined as

$$K_d(z, \lambda) = -\frac{d(\ln E_d(z, \lambda))}{dz} = -\frac{1}{E_d(z, \lambda)} \frac{dE_d(z, \lambda)}{dz}. \tag{2.17}$$

However, obtaining a value for $K_d(z, \lambda)$ at a specific depth requires $E_d(z, \lambda)$ to be measured at infinitesimal differences in depth. This has led to the introduction of an alternative quantity, $\overline{K}_d(z_1 \leftrightarrow z_2, \lambda)$ (Lee et al., 2005b),

$$\overline{K}_d(z_1 \leftrightarrow z_2, \lambda) = \frac{1}{z_2 - z_1} \ln \left(\frac{E_d(z_1, \lambda)}{E_d(z_2, \lambda)} \right), \tag{2.18}$$

which is the diffuse attenuation coefficient averaged between two depths, z_1 and z_2. All other diffuse attenuation coefficients can be similarly defined.

Typically, z_1 is taken at the surface, with $z_1 = 0$. The depth selected for z_2 varies across the literature, with Lee et al. (2005b) using the depth at which the downwelling irradiance has fallen to 10% of its surface value, and Mueller (2000) using the depth at which the downwelling irradiance has fallen to $1/e$ of its surface value.

Radiative Transfer Theory

The way in which the optical properties of the water column effect the underwater radiance distribution is described through radiative transfer theory and the radiative transfer equation. Consider a beam of light entering a volume of water from the direction (θ, ϕ), then the number of photons in the beam will change

due to absorption and scattering processes occurring along the path through the sample. Photons will either be scattered, elastically or inelastically, into and out of the beam path, absorbed as they travel along the beam path or emitted through processes such as bioluminescence (see Figure 2.1).

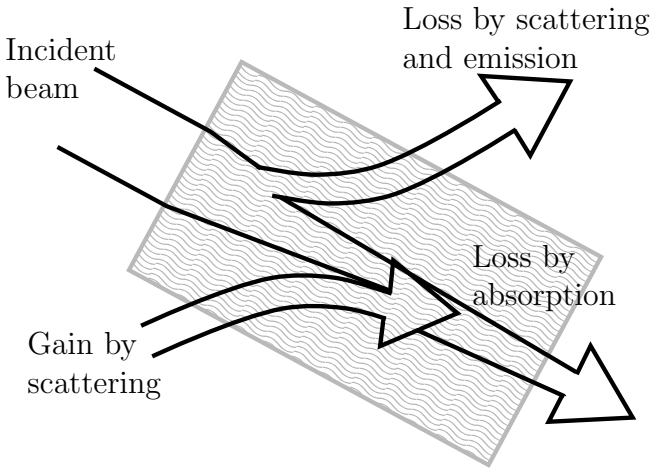

Figure 2.1: The processes which modify the radiance of a beam along a path though a water volume.

The radiative transfer equation for unpolarised, monochromatic radiation can be stated as: the rate of change of radiance along a path is equal to the sum of the increases and decreases in radiance from all the different sources. Mathematically, for radiance $L(z, \theta, \phi, \lambda)$ along a path of distance r,

$$\frac{\mathrm{d}L(z,\theta,\phi,\lambda)}{\mathrm{d}r} = -c(\lambda)L(z,\theta,\phi,\lambda) + L_*^E(z,\theta,\phi,\lambda) + L_*^I(z,\theta,\phi,\lambda) + L_*^S(z,\theta,\phi,\lambda), \tag{2.19}$$

where $c(\lambda)$ is the attenuation coefficient and $L_*^E(z,\theta,\phi,\lambda),\ L_*^I(z,\theta,\phi,\lambda),\ L_*^S(z,\theta,\phi,\lambda)$ are the path functions for elastic scattering, inelastic scattering and emission.

The path functions are radiances generated per unit distance along a path in the direction defined by (θ, ϕ) and the scattering path functions will be proportional to the incident radiance and a function of the scattering angle, which can

be described by the volume scattering function (Eq. (2.7)). Whereas, the emission path function will be different for each emission process, but generally will be proportional to the radiant power of the source ($S_0(\theta, \phi)$) and its directional distribution ($\widetilde{\beta}^s(\theta, \phi)$). Therefore the path functions take the following forms:

$$L_*^E(z, \theta, \phi, \lambda) = \int_\Xi L(z, \theta', \phi')\beta(z, \theta', \phi' \to z, \theta, \phi)\ \mathrm{d}\Omega(\theta', \phi') \tag{2.20}$$

$$L_*^I(z, \theta, \phi, \lambda) = \int_\Xi \int_\Lambda L(z, \theta', \phi', \lambda')\beta(z, \theta', \phi', \lambda' \to z, \theta, \phi, \lambda)\ \mathrm{d}\lambda' \mathrm{d}\Omega(\theta', \phi') \tag{2.21}$$

$$L_*^S(z, \theta, \phi, \lambda) = S_0(\lambda, z)\widetilde{\beta}^s(\theta, \phi), \tag{2.22}$$

where the prime ($'$) indicates the original direction and wavelength before scattering and the arrow denotes the change due to the scattering events. It is convenient to combine the path functions due to inelastic scattering and emission into one term, the effective source function, $S(z, \theta, \phi, \lambda)$. Assuming the water body is horizontally homogeneous and considering the change in radiance as a function of depth, z, then

$$\frac{\mathrm{d}L}{\mathrm{d}r} = \cos\theta \frac{\mathrm{d}L}{\mathrm{d}z}, \tag{2.23}$$

and the radiative transfer equation can be expressed as,

$$\begin{aligned} \cos\theta \frac{\mathrm{d}L(z, \theta, \phi, \lambda)}{\mathrm{d}z} \ &= \ -c(\lambda)L(z, \theta, \phi, \lambda) + \\ &\int_\Xi L(z, \theta', \phi')\beta(z, \theta', \phi' \to z, \theta, \phi)\ \mathrm{d}\Omega(\theta', \phi') + S(z, \theta, \phi, \lambda). \end{aligned} \tag{2.24}$$

The radiative transfer equation is a linear integrodifferential equation as it involves both an integral and a derivative of the radiance. Hence there are no fully analytical solutions, except for special cases such as non-scattering waters.

Solutions to the full equation can be derived through various numerical methods, such as invariant imbedding methods or Monte Carlo methods.

Relationship Between IOPs and AOPs

Early studies of radiative transfer theory using Monte Carlo numerical methods led to two approximate relationships between the reflectance and the absorption and backscattering coefficients.

Gordon (1973) used the quasi-single-scattering approximation to simplify the radiative transfer equation. This approximation modifies the phase function so that all of the scattering from particles in the forward direction is concentrated into one beam along the direction of propagation, as if there was no forward scattering at all. Using the single-scattering approximation and a modification to the beam attenuation coefficient, an exact, but complex, expression for the irradiance reflectance can be derived from the radiative transfer equation. This expression is difficult to simplify analytically, but it is proportional to the backscattering fraction. Gordon et al. (1975) used Monte Carlo simulations to model radiance distributions for a range of inherent optical properties and demonstrated

$$R(0^-, \lambda) \propto \frac{b_b(\lambda)}{a(\lambda) + b_b(\lambda)}. \tag{2.25}$$

In 1988, Gordon et al. showed that for a range of different solar zenith angles, the relationship between the subsurface remote sensing reflectance, $a(\lambda)$ and $b_b(\lambda)$ can be approximated by

$$r_{rs}(\lambda) = g_0 \frac{b_b(\lambda)}{a(\lambda) + b_b(\lambda)} + g_1 \left(\frac{b_b(\lambda)}{a(\lambda) + b_b(\lambda)} \right)^2. \tag{2.26}$$

The coefficients g_0 and g_1 are variable, but can be taken as constants under certain conditions, with $g_0 = 0.0949$, and $g_1 = 0.0794$ for solar zenith angles greater than 20°.

An alternative approach combines the analysis of the two-flow equations, which are a simplified form of the radiative transfer equation dealing with irradiance transfer, with the Preisendorfer (1976) 1-D model for undecomposed irradiance fields, leading to the following expression for the irradiance reflectance:

$$R(0^-, \lambda) \propto \frac{\frac{1}{2}\frac{b_b(\lambda)}{a(\lambda)}}{1 + \frac{1}{2}\frac{b_b(\lambda)}{a(\lambda)}}. \tag{2.27}$$

Morel and Prieur (1977) used modelling results for radiative transfer calculations to demonstrate that this could be simplified to

$$R(0^-, \lambda) = \frac{f}{Q}\frac{b_b(\lambda)}{a(\lambda)}. \tag{2.28}$$

The f/Q term is variable, but Morel and Prieur (1977) found it to be 0.33 from the successive order scattering method, with variations in its value less than 5%, without specifying the solar angles considered.

The variability in g_0, g_1, and f/Q has been shown to depend on the solar angle, radiance distribution, the volume scattering function and other water characteristics such as the single-scattering albedo and the backscattering efficiency.

Equations (2.26) and (2.28) are both used in ocean colour remote sensing as the foundation of many algorithms because of high solar and viewing angles accompanying satellite observations.

2.2 Satellite Imagery and Remote Sensing Methods

Backscattering events in the water column result in part of the underwater light field propagating back towards the surface and emerging from the water body. This emergent light can be measured by sensors, placed on satellites, which are directed towards a point on the Earth's surface. The sensors have a narrow field of view, typically covering an area of 1 km^2 of the surface. However, instruments which incorporate rotating mirrors scan perpendicularly to the direction of the satellite orbit, ending up with total swath widths ranging between 1000 - 3000 km for different sensors.

There has been a series of ocean colour sensors launched, starting with the Coastal Zone Colour Scanner (CZCS) in 1978. Currently, NASA have two operational sensors: the Moderate Resolution Imaging Spectroradiometer (MODIS) and the Visible and Infrared Imager/Radiometer Suite (VIIRS), with all satellite data for this study taken by MODIS.

MODIS was launched in 2002 aboard the Aqua satellite, which orbits the Earth every 99 minutes, covering the whole of the planet every 1-2 days. The orbit of the satellite is sun-synchronous, meaning it is operating during the daylight and it crosses the equator south to north in the early afternoon. The satellite is at an altitude of 705 km and with a scanning mirror rotating $\pm 55°$, the resultant swath width is 2330 km. MODIS is a multispectral sensor, with 36 spectral bands, 9 of which are used for ocean colour imaging at a 1 km resolution (see Table 2.1, however note that the 551 nm waveband has drifted and the central wavelength is actually 547 nm (Bailey, 2009)).

Central Wavelength (nm)	Bandwidth (nm)
412.5	405 – 420
443	438 – 448
488	483 – 493
531	526 – 536
551*	546 – 556
667	662 – 672
678	673 – 683
748	743 – 753
867	862 – 877

Table 2.1: The MODIS wavebands which are used for ocean colour imagery. The asterisk denotes that the 551 nm waveband has drifted and the central wavelength is 547 nm for that band.

The sensors on board satellites can receive light from three sources: emergent light from the water column, light which has been scattered in the atmosphere and light reflected off the water's surface. Satellites are angled so as to avoid the majority of the surface reflections, however there is no way to avoid light from atmospheric scattering. The contribution of the atmosphere to the upwelling light must be corrected for as it can account for more than 80 % of the signal received by the satellite (Morel, 1980). Both air molecules and aerosol particles scatter light in the atmosphere, and several atmospheric correction techniques have been developed to remove the light which reaches the satellite that has its origin in the atmosphere (Gordon and Wang, 1994; Stumpf et al., 2003; Ruddick et al., 2000).

The satellite data has to be processed from the raw photon counts measured by the satellite sensors to the products required by the end-user, such as the remote sensing reflectance or water-leaving radiance. This is done in multiple steps, hence various levels of data are available:

Level 0: unprocessed data at full resolution.

Level 1A: time-referenced, unprocessed data at full resolution with radiometric and geometric calibration coefficients and georeferencing parameters appended.

Level 1B: the Level 1A data with the radiometric and geometric calibrations applied.

Level 2: geophysical variables, known as products, with atmospheric corrections applied, at the same resolution as the Level 1 data (e.g. $R_{rs}(\lambda)$).

Level 3: geophysical variables/products that have been aggregated or projected over a set time period, for example a monthly composite of a product mapped across a region of interest.

2.3 Inversion Methods

The theory outlined in Section 2.1 demonstrates how with a priori knowledge of the system and the composition of the water column, the resultant light fields and reflectances can be modelled. However, the satellites have no a priori knowledge of the system, and the difficulty in ocean colour remote sensing arises in the so-called "inverse problem": attempting to infer information about the water column from the measured light signals (IOCCG, 2006). Various algorithms have been developed to estimate different quantities from the signals received by the satellites. Initially, work focussed on the open ocean, Case-1 waters, where phytoplankton were the main contributor to the optical properties and simple empirical band-ratio algorithms were found to work fairly well. However, in the

shelf sea, coastal, Case-2 regions, where minerals and CDOM play a major role in the attenuation of light, these empirical algorithms tend to fail (Aurin and Dierssen, 2012; Odermatt et al., 2012).

For the Case-2 waters, this has led to a movement away from the empirical methods toward model-based approaches (IOCCG, 2000), some of which are listed below:

Non-linear optimisation: A forward model is used to created radiances for a particular water composition and then by minimising the differences between the measured and modelled radiances, the composition of the water column is adjusted until the best match is obtained. This approach is expensive in terms of computational time, however it does retrieve concentrations of all the optically significant materials simultaneously.

Principal component analysis: Estimation functions for different parameters are generated from multi-dimensional analysis on a dataset with known constituents, IOPs and radiances. Then, by applying the estimation functions to radiances, the resultant parameters can be obtained. Deriving the estimation functions is initially computationally expensive, but once they have been derived the application of them to radiances is very quick, and one of the major advantages is the top-of-atmosphere radiance can be used as a starting point, removing the need for performing an atmospheric correction. The estimation functions are linear in nature, but the relationships between the concentrations of optically significant materials and the resultant radiances are actually non-linear, and so the analysis may not capture all of the variability of the data.

Neural networks: These are used to perform multiple non-linear regressions between reflectances in different spectral bands and the concentrations of the main constituents in the water column. The neural network needs to be initially trained on a dataset to obtain coefficients which can be used to describe the non-linear relationships between the different inputs and outputs. As with principle components analysis, the initial training of the neural network can be very time-consuming, however with the correct training, the neural network is a very powerful tool for retrieving the water constituents.

Semi-analytical methods: These use known optical properties and theoretical models to derive relationships between the IOPs and AOPs but require some empirical approximations to simplify solutions to the radiative transfer equation. Due to the fact that radiative transfer theory is used as the starting point and the algorithms are generally simple to understand and quick to implement, these methods have become popular in the field.

The focus of this thesis is on the use of semi-analytical algorithms for recovering both inherent and apparent optical properties, in particular the quasi-analytical approach of Lee et al. (2002, 2005b, 2007, 2009) and Lee (2012), which is outlined below.

The Quasi-Analytical Algorithm, QAA

Lee et al. (2002) presented an algorithm for retrieving the spectral absorption and backscattering coefficients from the remote sensing reflectance, known as the quasi-analytical algorithm or QAA. Over the years, this algorithm has been updated, however, the basic structure is still the same:

1. Estimation of the absorption coefficient at a particular wavelength $a(\lambda_0)$ from remote sensing reflectance spectra (details given on the following page, specifically Eqs. (2.32) and (2.33)).

2. $b_b(\lambda_0)$ is then estimated from the Gordon et al. (1988) relationship:

$$r_{rs}(\lambda) = g_0 \frac{b_b(\lambda)}{a(\lambda) + b_b(\lambda)} + g_1 \left(\frac{b_b(\lambda)}{a(\lambda) + b_b(\lambda)} \right)^2 \tag{2.26}$$

   where, g_0 and g_1 are 0.0895 and 0.01249 respectively, which are the average of the values found by Gordon et al. (1988) and Lee et al. (1999).

3. The backscattering coefficient is then extrapolated spectrally via

$$b_b(\lambda) = b_{bw}(\lambda) + b_{bp}(\lambda_0) \left(\frac{\lambda_0}{\lambda} \right)^{\eta}, \tag{2.29}$$

   where

$$\eta = 2 \left(1 - 1.2 \exp \left(-0.9 \frac{r_{rs}(443)}{r_{rs}(\lambda_0)} \right) \right). \tag{2.30}$$

4. Finally, the spectral b_b values can be used to evaluate a spectrally by Eq. (2.26) again.

Note the use of r_{rs}, the subsurface remote sensing reflectance, rather than R_{rs} in

the QAA. The two quantities can be related by (Lee et al., 2002),

$$r_{rs}(\lambda) = \frac{R_{rs}(\lambda)}{0.52 + 1.7R_{rs}(\lambda)}. \tag{2.31}$$

The value of λ_0 in the initial estimation of the absorption coefficient is usually a green wavelength dependent on the waveband of the sensor and is 547 nm for MODIS. It is this estimation which has been updated, as well as the inclusion of a switch in λ_0 to a longer wavelength for more turbid waters. The current version of the QAA is QAAv6, which uses the same equation to estimate the $a(\lambda_0)$ in the green as the previous version, QAAv5, but includes a switch in λ_0 to 667 nm for $R_{rs}(667) > 0.0015$ sr^{-1}. For $\lambda_0 = 547$ nm (Lee et al., 2009),

$$a(\lambda_0) = a_w(\lambda_0) + 10^{p_1 + p_2\chi + p_3\chi^2} \quad \text{where} \quad \chi = \log\left(\frac{r_{rs}(443) + r_{rs}(488)}{r_{rs}(\lambda_0) + 5\frac{r_{rs}(667)}{r_{rs}(488)}r_{rs}(667)}\right). \tag{2.32}$$

The coefficients of χ, (p_1, p_2, p_3), have numerical values of (-1.146, -1.366, -0.469), which were derived for the IOCCG synthetic dataset, a dataset created to test algorithms for the remote sensing of IOPs (IOCCG, 2006). The argument of the logarithm in the calculation of χ takes that specific form as it provides a smooth transition from open oceans to coastal waters (Lee et al., 2007). For $\lambda_0 = 667$ nm, Eq. (2.32) is replaced with (Lee, 2012)

$$a(667) = a_w(667) + q_1\left(\frac{R_{rs}(667)}{R_{rs}(443)}\right)^{q_2}, \tag{2.33}$$

where $q_1 = 0.07$ and $q_2 = 1.1$. The remaining steps are implemented as described above.

Diffuse Attenuation Coefficient, KdLee

Lee et al. (2005b) presented an algorithm, known as KdLee, to estimate the average diffuse attenuation coefficient for downwelling planar irradiance over the depth at which $E_d(\lambda)$ falls to 10% of its surface value, $z_{10\%}$, which is the midpoint of the euphotic zone. For brevity, this will be referred to as the mean, or depth-averaged, diffuse attenuation coefficient and denoted $\overline{K}_d(\lambda)$. The first step in the algorithm is to estimate $a(\lambda)$ and $b_b(\lambda)$ from QAA. Then a semianalytical expression is used to obtain $\overline{K}_d(\lambda)$,

$$\overline{K}_d(\lambda) = (1 + 0.005\theta_a)a(\lambda) + m_1(1 - m_2 e^{-m_3 a(\lambda)})b_b(\lambda), \tag{2.34}$$

where θ_a is the above surface solar zenith angle, $m_1 = 4.18$, $m_2 = 0.52$ and $m_3 = 10.8$. Lee et al. (2005b) simplified this expression to

$$\overline{K}_d(\lambda) = (1 + 0.005\theta_a)a(\lambda) + 3.47 b_b(\lambda), \tag{2.35}$$

which matches the form of earlier studies (Gordon, 1989; Sathyendranath and Platt, 1988). The original KdLee expression (Eq. (2.34)) was later updated to include the effect of changing scattering agents (Lee et al., 2013)

$$\overline{K}_d(\lambda) = (1 + 0.005\theta_a)a(\lambda) + (1 - \gamma\eta_w(\lambda))m_1(1 - m_2 e^{-m_3 a(\lambda)})b_b(\lambda), \tag{2.36}$$

where γ is a model parameter taking the value 0.265 and $\eta_w(\lambda)$ is defined as

$$\eta_w(\lambda) = \frac{b_{bw}(\lambda)}{b_b(\lambda)}, \tag{2.37}$$

with $b_{bw}(\lambda)$ representing the backscattering coefficient for pure seawater. Therefore, $\eta_w(\lambda)$ provides a measure of the contribution of the molecular backscattering to the total backscattering.

Euphotic Depth

The euphotic depth, Z_{eu}, is conventionally defined as the depth at which photosynthetically available radiation (PAR) is 1% of its surface value (Kirk, 1994). The Lee et al. (2007) method for estimating the euphotic depth inititally considers the downwelling irradiance in the visible domain:

$$E_{VIS}(z) = E_{VIS}(0)e^{-K_{VIS}(z)z}, \tag{2.38}$$

where $K_{VIS}(z)$ is the diffuse attenuation coefficient of E_{VIS} and is a function of both z and the IOPs (Lee et al., 2005c),

$$K_{VIS} = K_1 + \frac{K_2}{(1+z)^{0.5}}, \tag{2.39}$$

with

$$\begin{aligned} K_1 &= \left[\chi_0 + \chi_1(a(490))^{0.5} + \chi_2 b_b(490)\right](1 + \alpha_0 \sin(\theta_a)), \\ K_2 &= \left[\zeta_0 + \zeta_1 a(490) + \zeta_2 b_b(490)\right](\alpha_1 + \alpha_2 \cos(\theta_a)), \end{aligned} \tag{2.40}$$

where $a(490)$ and $b_b(490)$ are the absorption and backscattering coefficients at 490 nm respectively, and the χ, ζ and α terms are model constants (Lee et al., 2005c).

The optical depth, τ_E for E_{VIS} is defined as

$$K_{VIS}(z)z = \tau_E. \tag{2.41}$$

Since the vertical distribution of $E_{VIS}(z)$ is nearly identical to that of PAR(z), the euphotic depth occurs for $\tau_E = -\ln(0.01) = 4.605$ (from Eqs. (2.38) and (2.41)). Combining Eqs. (2.39) and (2.41) gives

$$z^3 + y_1 z^2 + y_2 z + y_3 = 0, \tag{2.42}$$

where

$$\begin{aligned} y_1 &= \frac{K_1^2 - K_2^2 - 2\tau_E K_1}{K_1^2}, \\ y_2 &= \frac{\tau_E^2 - 2\tau_E K_1}{K_1^2}, \\ y_3 &= \frac{\tau_E^2}{K_1^2}. \end{aligned} \tag{2.43}$$

There are three possible solutions to Eq. (2.42), but it is the smaller, positive solution which agrees with radiative transfer theory (Lee et al., 2007). Hence to determine the euphotic depth via this method, the solar zenith angle and the absorption and backscattering coefficients must be known.

Zhao et al. (2013) Algorithm

Zhao et al. (2013) proposed a hyperbolic relationship between the euphotic depth and the diffuse attenuation coefficient at 490 nm, from a study based in the south Florida coastal waters and the Caribbean Sea,

$$Z_{eu} = 0.28 + \frac{395.92 \times 0.0092}{0.0092 + K_d(490)}. \tag{2.44}$$

Cunningham et al. (2013) Algorithm

Cunningham et al. (2013) observed a power law relationship between the euphotic depth and the diffuse attenuation coefficient at 490 nm in the Irish Sea

which takes the following form (for constants n_1 and n_2),

$$Z_{eu} = n_1 K_d(490)^{n_2}. \tag{2.45}$$

2.4 Summary

The main optical theory used in this study has been reviewed in this Chapter. The relevant inherent and apparent optical properties of the water column were defined and used to show how radiance distributions are generated through radiative transfer theory. Additionally, the theory behind two approximate relationships between the inherent and apparent optical properties, which are important in many remote sensing algorithms, was explained. The discussion was then extended to cover the use of satellites in measuring ocean colour and some of the difficulties encountered, such as signals originating in the atmosphere rather than from the water column. Finally, the inverse problem of retrieving the optical properties of the water column from the signals detected by satellites was discussed, with a detailed overview of some algorithms developed for this purpose.

3. Methodology

3.1 In Situ Observations

Data used in this study were acquired from 7 research cruises in the Irish Sea and the adjacent waters of the Firth of Clyde and Bristol Channel between 2001 and 2006 (Figure 3.1). On these field campaigns both inherent optical properties and radiometric quantities were determined, providing an ideal dataset for remote sensing algorithm validation and development.

Radiometry

The radiometry measurements were made with a Satlantic SeaWiFS Profiling Multichannel Radiometer (SPMR). Vertical upwelling radiance ($L_u(\lambda, z)$) and downward planar irradiance ($E_d(\lambda, z)$) profiles were determined for 1 m depth bins using the software provided by the manufacturer (ProSoft 7.7) in the instrument's 10 nm full width half maximum wavebands which are centred on 412, 443, 490, 510, 555, 667 and 700 nm. The ProSoft software processes the raw data collected by the instrument to different levels and ultimately to radiometric products including $L_u(\lambda, z)$, $E_d(\lambda, z)$, diffuse attenuation coefficients and reflectances.

In this study, only the profiles of $L_u(\lambda, z)$ and $E_d(\lambda, z)$ were obtained using the ProSoft software. Additional quantities including remote sensing reflectances, depth-averaged diffuse attenuation coefficients and the euphotic depths were derived from these profiles. For all these quantities, the subsurface downward planar

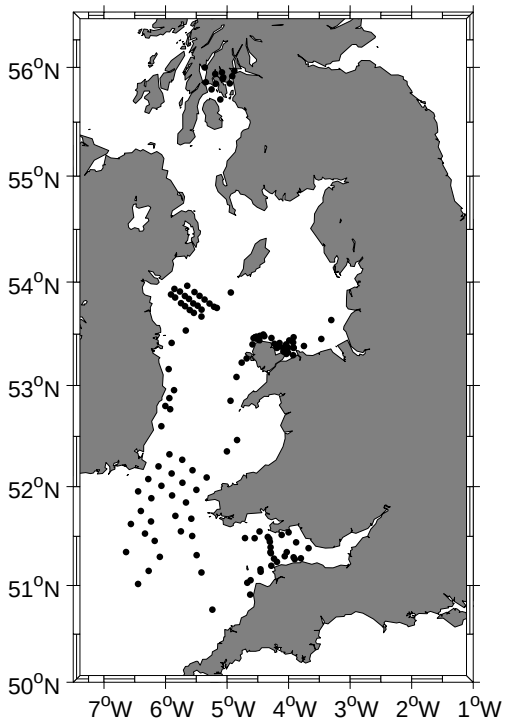

Figure 3.1: Map of stations from cruises in the Irish Sea and surrounding waters with coincident IOP and radiometry measurements collected during 2001-2006.

irradiance, $E_d(\lambda, 0^-)$, needed to be calculated due to practical difficulties in measuring the subsurface values with the SPMR. The downward planar irradiance was assumed to decrease exponentially with depth,

$$E_d(\lambda, z) = E_d(\lambda, 0^-)e^{-K_d(\lambda,z)z} \tag{3.1}$$

therefore, from a least-squares fit between the top 5 depths and the logarithm of $E_d(\lambda, z)$, the y-intercept was taken as the surface value. Only stations for which there were at least 10 depths within the profile were included in the analysis to avoid artefacts at the bottom of the casts. The subsurface value of the upwelling radiance, $L_u(\lambda, 0^-)$, was determined by the same procedure and the ratio of these

two values gave the subsurface remote sensing reflectance,

$$r_{rs}(\lambda) = \frac{L_u(\lambda, 0^-)}{E_d(\lambda, 0^-)}. \tag{3.2}$$

The depth-averaged diffuse attenuation coefficient was calculated over the depth at which $E_d(\lambda, z)$ falls to 10% of its surface value (Lee et al., 2005b). This depth, $z_{10\%}$, was determined from the profiles and then $\overline{K}_d(\lambda)$ was obtained from,

$$\overline{K}_d(\lambda) = \frac{1}{z_{10\%}} \log \left(\frac{E_d(\lambda, 0^-)}{E_d(\lambda, z_{10\%})} \right). \tag{3.3}$$

The euphotic depth is defined as the depth at which the surface photosynthetically available radiation (PAR) has fallen to 1% of its surface value (Kirk, 1994) hence $E_d(\lambda, z)$ was converted to PAR for the SPMR profiles by converting the SPMR data to quantum units and carrying out spectral integration. Then from examining each profile, the euphotic depth at a given station was determined.

Absorption and Attenuation Coefficients

The non-water absorption and attenuation coefficients were measured in nine wavebands (centred on 412, 440, 488, 510, 532, 555, 650, 676, 715 nm) using a WETLabs absorption and attenuation meter (both an ac-9 and an ac-9 plus were deployed on different research cruises). This instrument consists of a dual path optical configuration, where, in each, a light source passes through a flow tube containing a water sample (WetLabs, 2006). In the attenuation path, the internal wall of the flow tube is black, so any scattered photons that hit the tube walls are absorbed, leaving the light which is transmitted through the flow tube to have been subject to absorption and scattering by the water sample. Conversely, the

flow tube of the absorption path has reflective walls, therefore any light passing through the tube is absorbed by the water sample. The collection optics for each path also differ, with the attenuation path containing a lens and receiver and the absorption tube containing a diffuse collector. In practise, the attenuation sensor fails to exclude all scattered photons and the absorption sensor fails to collect all scattered photons, so these scattering errors need to be corrected for (Zaneveld et al., 1994; Stramski and Piskozub, 2003; Piskozub et al., 2004; McKee et al., 2008).

The measured coefficients were corrected for the temperature and salinity of the seawater using data from the CTD profiles which were obtained at the same time as the ac-9 deployments, with coefficients from Sullivan et al. (2006). The absorption measurements were scattering corrected using the method of Zaneveld et al. (1994) to retain consistency with previous work even though the validity of the negligible near-IR absorption by particles, which is assumed in this method, has been challenged (McKee et al., 2013). From $a_{nw}(\lambda)$ and $c_{nw}(\lambda)$ the non-water scattering coefficients were determined. By adding water absorption data from Pope and Fry (1997), the total absorption coefficients were obtained.

Backscattering Coefficients

Measurements of the backscattering coefficients in two wavebands, centred on 470 and 676 nm, were carried out using a HOBI Labs HydroScat-2 Backscattering and fluorescence Sensor (hs-2). The instrument contains two channels, each with a separate LED source and receiver. In each channel, the light beam enters the water approximately 20° from the normal and the receiver field-of-view is angled towards the source beam by a prism (HOBILabs, 2008). The geometry of the

HydroScat results in measurements centred on a scattering angle of 140°, from which the backscattering coefficient is estimated using the method of Maffione and Dana (1997).

The backscattering coefficients were corrected for absorption and scattering effects in the water sample using the sigma correction method recommended by the manufacturer, which incorporates the ac-9 measurements of a_{nw} and b_{nw}.

3.2 Radiative Transfer Modelling

Inherent Optical Properties (IOPs)

Total IOPs were assumed to be functions of three main optically significant constituents: phytoplankton (measured as chlorophyll-a (CHL)), mineral suspended solids (MSS) and coloured dissolved organic matter (CDOM). The IOPs of each constituent are often modelled assuming linear relationships between the constituent concentration and specific inherent optical properties (SIOPs), for example:

$$\begin{gathered} a_{\mathrm{MSS}}(\lambda) = [\mathrm{MSS}] \times a^*_{\mathrm{MSS}}(\lambda), \qquad b_{\mathrm{MSS}}(\lambda) = [\mathrm{MSS}] \times b^*_{\mathrm{MSS}}(\lambda) \\ \text{and} \qquad b_{b\mathrm{MSS}}(\lambda) = [\mathrm{MSS}] \times b^*_{b\mathrm{MSS}}(\lambda) \end{gathered} \tag{3.4}$$

where the square brackets denote constituent concentration and the asterisks represent the specific inherent optical property. However, Bricaud et al. (1995) observed a power law relationship between phytoplankton absorption and [CHL]. This is due to the package effect, which tends to increase from oligotrophic to eutrophic waters (Kirk, 1994). When comparing the absorption of a suspension of phytoplankton cells with that of a solution which contains a uniform distribution

of photosynthesising pigments, the suspension absorbs less than the solution, as the pigments in suspension are packaged together within the phytoplankton cells. This effect becomes more pronounced as the density of pigment molecules within the cells increases, and the peaks of the phytoplankton absorption spectra flatten and the specific absorption coefficient decreases (Kirk, 1975a,b). In this case $a_{\mathrm{CHL}}(\lambda)$ can be modelled by:

$$a_{\mathrm{CHL}}(\lambda) = a_{\mathrm{CHL}}(440)\frac{a^*_{\mathrm{CHL}}(\lambda)}{a^*_{\mathrm{CHL}}(440)} \tag{3.5}$$

where $a_{\mathrm{CHL}}(440)$ is obtained from the following power law (Bricaud et al., 1995):

$$a_{\mathrm{CHL}}(440) = A[\mathrm{CHL}]^B. \tag{3.6}$$

Initially, Bricaud et al. determined $A = 0.0403$ and $B = 0.668$, but these were later updated to include more data samples, resulting in $A = 0.0378$ and $B = 0.627$ (Bricaud et al., 1998). The IOCCG created a synthetic dataset for algorithm development and validation, in which $A = 0.05$ and $B = 0.626$, to generate a reasonable range of $a_{\mathrm{CHL}}(440)$ values (IOCCG, 2006).

For low concentrations of chlorophyll-a, the resultant absorption is similar when using either the power law (Eqs (3.5) and (3.6)) or a linear relationship between concentration and the SIOP (Eq (3.4)). For increasing concentrations of chlorophyll-a, the resultant absorption coefficient estimated by both methods deviates rapidly due to the nature of the power law.

Typical values of SIOPs for the Irish Sea were derived from the field measurements described by Neil et al. (2011), but with two modifications from their methodology. First, the absorption coefficients were linearly interpolated to in-

clude the MODIS wavebands, see Table 3.1. Second, the wavelength dependence of the particulate backscattering coefficients were assumed to have the form (Lee et al., 2002; Smith and Baker, 1981)

$$b_{bp}(\lambda) = b_{bp}(\lambda_0)\left(\frac{\lambda_0}{\lambda}\right)^{\eta}. \tag{3.7}$$

For the interpolations of $b_b(\lambda)$ between the wavebands measured by the Hydroscat 2 to the MODIS and SPMR wavebands, λ_0 was taken to be 470 nm and

$$\eta = \frac{\log(b_{bp}(676)/b_{bp}(470))}{\log(470/676)}.$$

λ (nm)	$a^*_{\mathrm{CHL}}(\lambda)$ ($\mathrm{m^2\ mg^{-1}}$)	$a^*_{\mathrm{MSS}}(\lambda)$ ($\mathrm{m^2\ g^{-1}}$)	$a^*_{\mathrm{CDOM}}(\lambda)$ (none)	$b^*_{\mathrm{CHL}}(\lambda)$ ($\mathrm{m^2\ mg^{-1}}$)	$b^*_{\mathrm{MSS}}(\lambda)$ ($\mathrm{m^2\ g^{-1}}$)	$b^*_{b\mathrm{CHL}}(\lambda)$ ($\mathrm{m^2\ mg^{-1}}$)	$b^*_{b\mathrm{MSS}}(\lambda)$ ($\mathrm{m^2\ g^{-1}}$)
412	0.061	0.071	1.39	0.12	0.4	0.0017	0.0163
440	0.077	0.054	1.00	0.12	0.4	0.00160	0.0160
443	0.075	0.052	0.95	0.12	0.4	0.00159	0.0159
488	0.057	0.034	0.57	0.12	0.4	0.00149	0.0155
510	0.041	0.028	0.44	0.12	0.4	0.00144	0.0152
531	0.031	0.022	0.34	0.12	0.4	0.00140	0.0150
547	0.023	0.019	0.28	0.12	0.4	0.00138	0.0149
555	0.019	0.018	0.25	0.12	0.4	0.00136	0.0148
667	0.038	0.0060	0.067	0.12	0.4	0.00119	0.0140

Table 3.1: Specific inherent optical properties used in radiative transfer modelling

The range of concentrations assumed for the optically significant materials were based on previous studies of the region as discussed in Chapter 1 (Bowers et al., 2013; Gowen et al., 2008; McKee and Cunningham, 2006).

HydroLight and EcoLight

HydroLight and EcoLight (Sequoia Scientific Inc.) are numerical radiative transfer models which solve different versions of the radiative transfer equation to obtain the light field (and associated quantities such as remote sensing reflectance)

within and leaving any plane-parallel water body (Mobley and Sundman, 2008). EcoLight solves the azimuthally-averaged radiative transfer equation, rather than for the full radiance distribution, which saves computational time if the outputs required are remote sensing reflectance and other quantities that do not require the full radiance distribution. A full description of the numerical methods used to solve the models is provided by Mobley (1994). Both models require similar inputs including

1. The inherent optical properties of the water body, which can either be provided directly or determined using the bio-optical models within the software.
2. The nature of the wind-blown sea surface, which is modelled using Cox-Munk capillary-gravity wave-slope statistics and hence requires the wind speed and refractive index of water.
3. The radiance distribution incident on the water surface due to the sun and sky conditions. This can be provided directly from measurements, determined from semi-empirical models within the software or from a user-supplied model. The inbuilt semi-empirical model requires the user to provide the position of the sun and cloud cover.
4. The nature of the bottom boundary, that is, if there is reflectance off the bottom of the sea-bed, and if there is, how to treat the nature of the surface (Lambertian or from a user-supplied bi-directional reflectance distribution function).

For this study, the light fields generated by the modelled IOPs were estimated using EcoLight (version 5) with the following set-up:

1. User-supplied IOPs (absorption, attenuation and backscattering), with Fourier-

Forand scattering phase functions selected using the backscatter fraction of the provided IOPs,

2. No inelastic scatter,
3. Solar angle = 45°,
4. Cloud free sky,
5. Wind speed = 5 ms^{-1},
6. Infinitely deep water column (no bottom reflectance)
7. Eight output wavebands, with a bandwidth of 10 nm, centred on: 412, 443, 488, 510, 531, 547, 555 and 667 nm.

The remote sensing reflectance spectra generated by EcoLight were then used for evaluating inversion algorithms in the Irish Sea.

3.3 Satellite Imagery Processing

SeaDAS Processing

Ocean colour satellite data from current and historic missions are distributed by NASA's Goddard Space Flight Centre Ocean Biology Processing Group via the OceanColor Web, a website which serves as the data access portal (http://oceancolor.gsfc.nasa.gov/). Data are available from point-and-click visual browsers and by direct access for bulk download orders. NASA have developed an image processing, analysis and visualisation package, the SeaWiFS Data Analysis System (SeaDAS), for working with the satellite data. The software has in-built programs for processing data through all the various levels, for different satellite missions. The visualisation software was originally developed on an IDL-based interface, however in 2013 this was transitioned to a Java based interface, ESA's

BEAM (Basic ENVISAT Toolbox for (A)ATSR and MERIS). The data processing code was unchanged in this update, but BEAM was extended to include an interface to allow access to these processing programs.

In this study, level 1A data covering the Irish Sea over an eight year time period (2005 - 2012) were downloaded. Initially only partially cloud-free images were manually selected and downloaded from the online browser, however this dataset was later extended by ordering all available data within the time period, irrespective of the cloud cover, increasing the data coverage from 322 images to 4782 images. The ordered level 1A satellite files were downloaded from the NASA distribution server and processed to level 2 data files, at 1 km resolution, in SeaDAS version 6.4 using the default two-band aerosol model with an iterative near infra-red correction (Gordon and Wang, 1994; Stumpf et al., 2003). The level 2 products, listed in Table 3.2, were mapped using a Mercator projection and then output as HDF files for further processing and analysis in MATLAB. For

Level 2 Product	Description
$R_{rs}(\lambda)$	Remote sensing reflectance (units: sr^{-1}) in the following wavebands: 412, 443, 488, 531, 547 and 667 nm
solz	the solar zenith angle (units: °)
sst	the sea surface temperature (units: °C)

Table 3.2: Level 2 products used in this study

handling such large quantities of data, a series of scripts which incorporated the relevant SeaDAS processing commands were written to automate the downloading and processing of level 1A data files to the mapped HDF files. The following summarises the scripts which were written:

download_untar: Downloads the data files which have been bundled into tar

files from the NASA distribution server and unpacks them into all the individual, zipped level 1A files.

unzipping_sorting: Unzips the individual level 1A files and then sorts each one into its own directory.

TimeSeriesL1AtoHDF: Processes each level 1A file to a mapped HDF file. This script calls the SeaDAS processing functions, initially processing the level 1A file to level 1B, then the level 1B file to level 2. A separate script is called which contains the commands for the final processing to a mapped HDF file.

OutputMappedHDF: Maps the level 2 data and outputs it in an HDF format. This script is called in the TimeSeriesL1AtoHDF script.

MATLAB Processing

All the mapped data were cleaned in MATLAB, first by identifying the pixels which were land or masked by cloud, and excluding these from further analysis. Additionally, only sea surface temperature pixels where there was a coincident remote sensing reflectance value were included in analysis as there were often erroneous SST values associated with the presence of thin cloud. Pixels from the Solway Firth, Morecambe Bay and the Bristol Channel were excluded due to their close proximity to land and the high turbidity of these regions. The northern limit of the region was taken as the North Channel (see Figure 3.2). The valid data were grouped by month and year and saved in individual MATLAB data files (known as mat files) for analysis.

Throughout this study, inversion algorithms were applied to the satellite data via the mat files, with the resultant products saved in a separate mat file, again

grouped by month and year. Therefore all the data for analysis, both level 2 products and inversion products, were saved within 192 individual mat files. Figure 3.3 shows a flow chart which summarises the processing steps.

Time Series Data

Analysis of the full time series required both temporal and spatial averaging of the dataset. When examining the full time series at a particular location, spatially averaging a patch of data reduced any features caused by erroneous pixels. Hence, for an 11 x 11 patch of data, if over half the patch contained valid pixels on a given day, the mean was used as a representative value, otherwise, no value was taken for that day.

Due to the relatively sparse coverage, particularly over the winter months, it was useful to consider a mean annual cycle for the various products. These were obtained by grouping all the observations at a given pixel or patch into a specified time interval (weekly, fortnightly or monthly) and taking the average value for that pixel. If there were more than 5 observations for a pixel, then the standard deviation was also calculated.

Data Visualisation

All data visualisation was done in MATLAB, including the mapping and generation of images of the Irish Sea. The mapping toolbox used was the freely available M_Map package from the University of Columbia Earth Observation Sciences Group (http://www.eos.ubc.ca/~rich/map.html).

Figure 3.2: A quasi-true colour MODIS image of the Irish Sea and surrounding waters on the 26th March 2012. The red lines indicate the boundaries of the region considered for time series analysis. (Image Credit: NERC Satellite Receiving Station, Dundee University, Scotland, http://www.sat.dundee.ac.uk/)

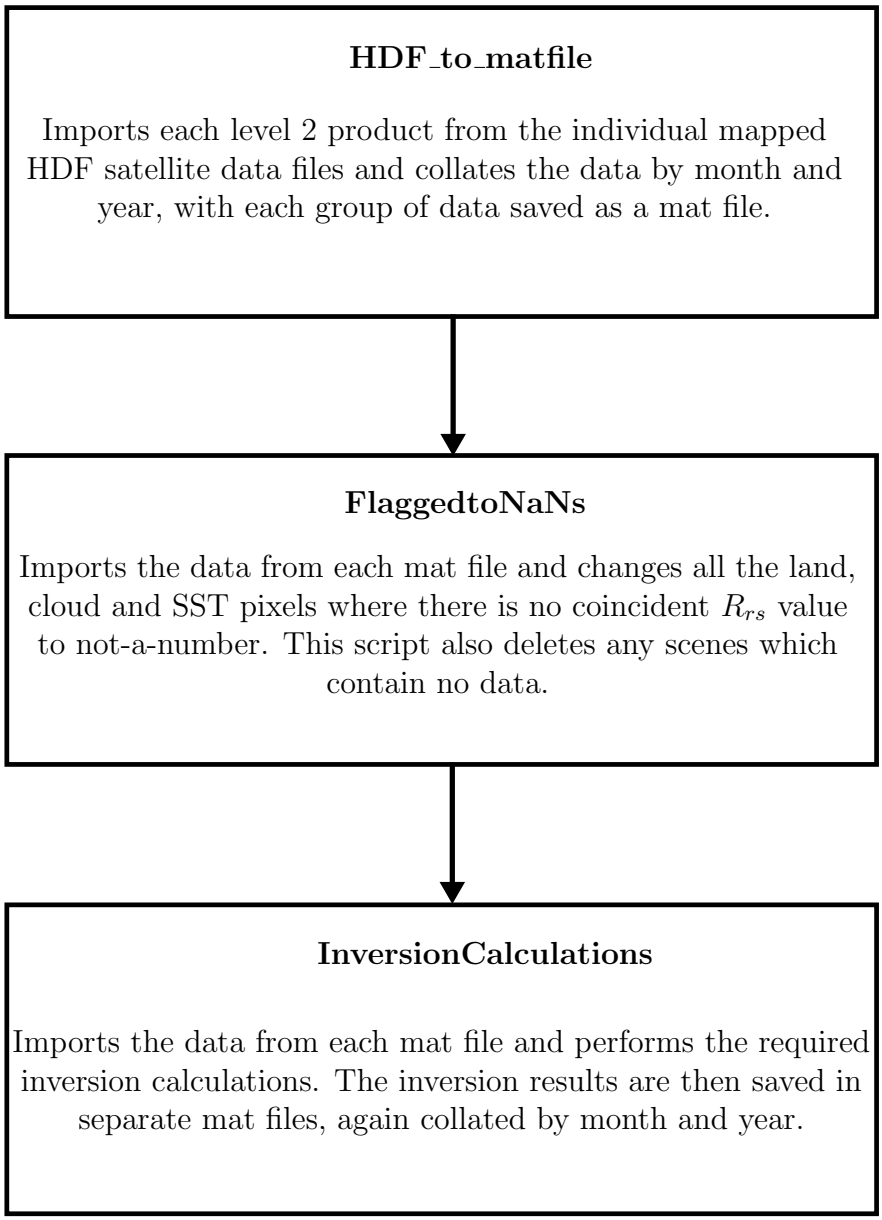

Figure 3.3: The MATLAB processing procedure.

Summary

The methods discussed in this chapter, cover three main areas:

1. In Situ Observations - an overview of the instruments used and details of the data processing.
2. Radiative Transfer Modelling - details of modelling the inherent optical properties and the method used to model the resultant light fields.
3. Satellite Imagery Processing - a discussion of the programs used and the methods applied for the processing and analysis of satellite data.

4. Evaluation of a Quasi-Analytical Approach to Remote Sensing of Optical Properties

In this chapter the absorption, backscattering and depth-averaged diffuse attenuation coefficients are estimated by the quasi-analytical approach of Lee et al. (2002, 2005b, 2007, 2009) and Lee (2012) and the resultant coefficients were used to estimate the euphotic depth by three different methods. The approach of Lee et al. has been modified over the years and the procedure evaluated here employs the following steps:

1. QAAv6 (the quasi-analytical algorithm version 6 (Lee, 2012)), to recover $a(\lambda)$ and $b_b(\lambda)$ from $R_{rs}(\lambda)$.
2. Three different versions of the Lee et al. (2005b) algorithm to recover $\overline{K}_d(\lambda)$ from $a(\lambda)$ and $b_b(\lambda)$ and the solar zenith angle
   i) the original KdLee (Eq. (2.34)),
   ii) KdLee_simp, the simplified version of KdLee (Eq. (2.35)),
   iii) KdLee_2013, the updated version of KdLee (Eq. (2.36)).
3. Three different algorithms to recover the euphotic depth, Z_{eu}, from $a(490)$, $b_b(490)$ and $\overline{K}_d(490)$

i) Z_Lee (the algorithm of Lee et al. (2007)), to recover the euphotic depth from $a(490)$ and $b_b(490)$,

ii) Z_Zhao (the algorithm of Zhao et al. (2013)), to recover the euphotic depth from $\overline{K}_d(490)$ using a hyperbolic function,

iii) Z_Cunningham (the algorithm of Cunningham et al. (2013)), to recover the euphotic depth from $\overline{K}_d(490)$ using a power law.

The performance of QAAv6 was initially evaluated on a bio-optical model of the Irish Sea, and adjusted to optimise its performance (see the following section). The regionally tuned QAA and the $\overline{K}_d(\lambda)$ and Z_{eu} algorithms were all tested and validated with field data from the Irish Sea.

4.1 Bio-optical Model of the Irish Sea

As discussed in Section 2.3, QAAv6 follows QAAv5, but includes a change in reference wavelength to 667 nm for more turbid waters. QAAv5 was developed using the IOCCG synthetic dataset (IOCCG, 2006), which was generated to cover a wide range of both Case-1 and Case-2 waters, providing a dataset for algorithm development and validation. However, a few assumptions were made in creating the IOCCG dataset:

1. CDOM was modelled to co-vary with CHL.
2. The detritus particulate component was restricted so that there were no large mineral contributions when the phytoplankton contribution was low.
3. Phytoplankton absorption was assumed to have a power law relationship with CHL concentration (Bricaud et al., 1995).
4. A 1% b_b/b Fournier-Forand phase function was used for phytoplankton.

5. The Petzold average phase function was used for the mineral component.
6. The backscattering coefficients for both phytoplankton and mineral particles were restricted to vary with CHL concentration but in a random fashion.

In the Irish Sea, these assumptions are not all valid:

1. There are CDOM rich estuaries feeding the Irish Sea, hence CDOM does not always co-vary with CHL (Tilstone et al., 2005).
2. The optical properties of much of the Irish Sea are driven by mineral particles in the surface layer in the winter and phytoplankton particles in the summer, therefore often a high mineral contribution coincides with a low phytoplankton contribution (Fig. 2 of Neil et al. 2011).
3. McKee and Cunningham (2006) observed the backscattering ratio of phytoplankton particles to be approximately 0.014 at 488 nm, which is slightly higher than the 1% assumed in the IOCCG synthetic dataset.
4. McKee and Cunningham (2006) observed the backscattering ratio of mineral particles to be approximately 0.04 at 488 nm, which is significantly higher than 0.0183, which is the value used for the Petzold average phase function.

It was necessary, therefore to use a specially constructed bio-optical model of the region to generate synthetic datasets to evaluate the inversion procedure for the Irish Sea. By randomly sampling concentrations of the optically significant materials (OSMs) from within typical ranges, the full gamut of possible combinations in the region could be covered. This allowed the extreme ranges of the constituent concentrations to be tested, but it produced distributions that were approximately uniform across the full range of available concentrations, which

does not represent in situ measurements. It could be argued that, characterising constituent concentrations with log-normal distributions is more representative of field observations.

One important assumption made in the IOCCG synthetic dataset is that phytoplankton absorption has a power law relationship with [CHL]. This effect has been well documented for oceanic waters, but coastal waters have received a less thorough examination. As part of an extensive study of light absorption in coastal waters Babin et al. (2003) investigated the power law relationship for phytoplankton absorption, finding significant variability and differences among the regions observed. In fact, Babin et al. advise against indiscriminate use of the power law relationship for phytoplankton absorption in coastal regions.

For these reasons, it was decided to create two modelled datasets specifically to test the validity of the products generated by QAAv6. Both datasets were generated as described in Section 3.2 using regional SIOPs but different distributions of optically significant materials. Additionally, each dataset modelled phytoplankton absorption differently, one using the power law of Bricaud et al. (1995) and one assuming a linear relationship between the CHL concentration and $a^*_{\mathrm{CHL}}(\lambda)$. The differences between the two synthetic datasets are outlined below:

IS-1 (Irish Sea Model 1): OSMs randomly sampled within the following ranges

[CHL]: 0 - 10 mg m^{-3}

[MSS]: 0 - 15 g m^{-3}

[CDOM]: 0 - 0.5 m^{-1} $a(440)$,

and phytoplankton absorption was assumed to follow the same power law as the IOCCG synthetic dataset (Eqs. (3.5) and (3.6)).

IS-2 (Irish Sea Model 2): OSMs were randomly sampled from the log-normal distributions (see Figure 4.1) described by the parameters in Table 4.1 and phytoplankton absorption was assumed to have a linear relationship with CHL concentration.

Constituent	Mean	Mode	Standard Deviation	Coefficient of Variation
CHL (mg m^{-3})	2.4	1.9	1.3	0.54
MSS (g m^{-3})	2.7	2.2	1.4	0.52
CDOM (m^{-1})	0.13	0.12	0.03	0.23

Table 4.1: Descriptive statistics for the distributions of the constituent concentrations in dataset IS-2.

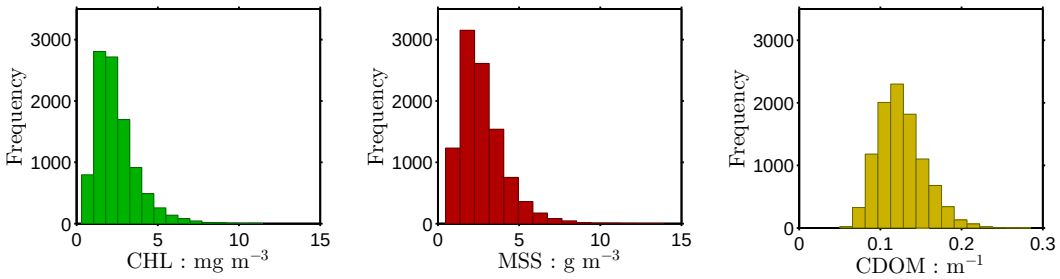

Figure 4.1: Distributions of the optically significant material concentrations used in dataset IS-2.

All versions of the QAA rely on the relationship of Gordon et al. (1988),

$$r_{rs}(\lambda) = g_0 \frac{b_b(\lambda)}{a(\lambda) + b_b(\lambda)} + g_1 \left(\frac{b_b(\lambda)}{a(\lambda) + b_b(\lambda)} \right)^2, \tag{2.26}$$

hence the $r_{rs}(\lambda)$ values derived through EcoLight for IS-1 were compared with those derived using Eq. (2.26), with $g_0 = 0.0895$ and $g_1 = 0.01249$. Additional EcoLight runs were included to investigate the effect of varying solar angles and level of cloud cover on this relationship. For both IS-1 and the data from the additional EcoLight runs, the $r_{rs}(\lambda)$ values calculated using Eq. (2.26) were highly correlated with those from EcoLight, with a linear regression giving a gradient

of 1. Hence, to save computational time, the $r_{rs}(\lambda)$ values for IS-2 were derived using the Gordon et al. (1988) relationship.

4.2 Performance of QAAv6 when Applied to Synthetic Dataset IS-1

QAA begins with an estimation of the absorption coefficient at a particular wavelength, and for QAAv6 this is either a sensor-dependent green wavelength, λ_0, (547 nm for MODIS) or 667 nm, with the following equations for the estimations (see Section 2.3 for full details):

$$a(\lambda_0) = a_w(\lambda_0) + 10^{p_1+p_2\chi+p_3\chi^2} \quad \text{where} \quad \chi = \log\left(\frac{r_{rs}(443)+r_{rs}(488)}{r_{rs}(\lambda_0)+5\frac{r_{rs}(667)}{r_{rs}(488)}r_{rs}(667)}\right), \tag{4.1}$$

and

$$a(667) = a_w(667) + q_1\left(\frac{R_{rs}(667)}{R_{rs}(443)}\right)^{q_2}, \tag{4.2}$$

When QAAv6 was applied to IS-1 both $a(\lambda)$ and $b_b(\lambda)$ were underestimated (see Table 4.2). The coefficients (p_1, p_2, p_3, q_1 and q_2) can all be optimised for the Irish Sea by performing a least squares fit to the synthetic dataset, IS-1, using the Levenberg-Marquardt technique. Table 4.3 shows the original and optimised coefficients.

The Irish Sea optimised QAAv6 was applied to IS-1 with the performance for the first 6 SPMR wavebands shown in Figures 4.2 and 4.3. Two additional wavebands matching the remaining MODIS wavebands (531 and 547 nm) were included in the analysis, with regression results for all eight wavelengths given in Table 4.2. The coefficients of determination, R^2, and root mean square errors,

RMSE, were similar for both the original and optimised algorithms, however the mean percentage errors (MPE) significantly reduced and the gradients of the regressions were closer to unity when applying the Irish Sea optimised QAAv6.

Parameter	Original Algorithm				Optimised Algorithm			
	gradient	R^2	RMSE (m^{-1})	MPE	gradient	R^2	RMSE (m^{-1})	MPE
$a(412)$	0.97	0.98	0.055	-4.2	1.02	0.98	0.058	2.5
$a(443)$	0.95	0.98	0.041	-5.7	1.00	0.98	0.043	1.1
$a(488)$	0.93	0.97	0.026	-7.2	0.98	0.98	0.027	-0.5
$a(510)$	0.93	0.97	0.022	-7.6	0.98	0.97	0.023	-1.0
$a(531)$	0.93	0.97	0.018	-8.0	0.99	0.97	0.019	-1.4
$a(547)$	0.94	0.97	0.016	-8.3	1.00	0.97	0.017	-1.7
$a(555)$	0.94	0.97	0.015	-8.6	1.00	0.97	0.016	-1.9
$a(667)$	0.52	0.37	0.023	-6.8	0.54	0.44	0.023	0.0
$b_b(412)$	0.95	0.99	0.007	-7.3	1.01	0.99	0.008	-0.8
$b_b(443)$	0.94	0.99	0.007	-7.9	1.01	0.99	0.007	-1.3
$b_b(488)$	0.94	0.99	0.006	-7.9	1.00	0.99	0.006	-1.3
$b_b(510)$	0.94	0.99	0.006	-7.8	1.01	0.99	0.006	-1.2
$b_b(531)$	0.94	0.99	0.006	-7.8	1.01	0.99	0.006	-1.0
$b_b(547)$	0.94	0.99	0.005	-7.7	1.01	0.99	0.006	-1.0
$b_b(555)$	0.94	0.99	0.005	-7.8	1.01	0.99	0.006	-1.1
$b_b(667)$	0.94	0.99	0.005	-7.8	1.01	0.99	0.005	-1.0

Table 4.2: Regression results for QAAv6 with the original and optimised coefficients on synthetic dataset IS-1

Algorithm	p_1	p_2	p_3	q_1	q_2
Original	-1.146	-1.366	-0.469	0.07	1.10
Optimised	-1.122	-1.338	-0.533	0.11	0.69

Table 4.3: Coefficients for the absorption estimation for the original and optimised QAAv6.

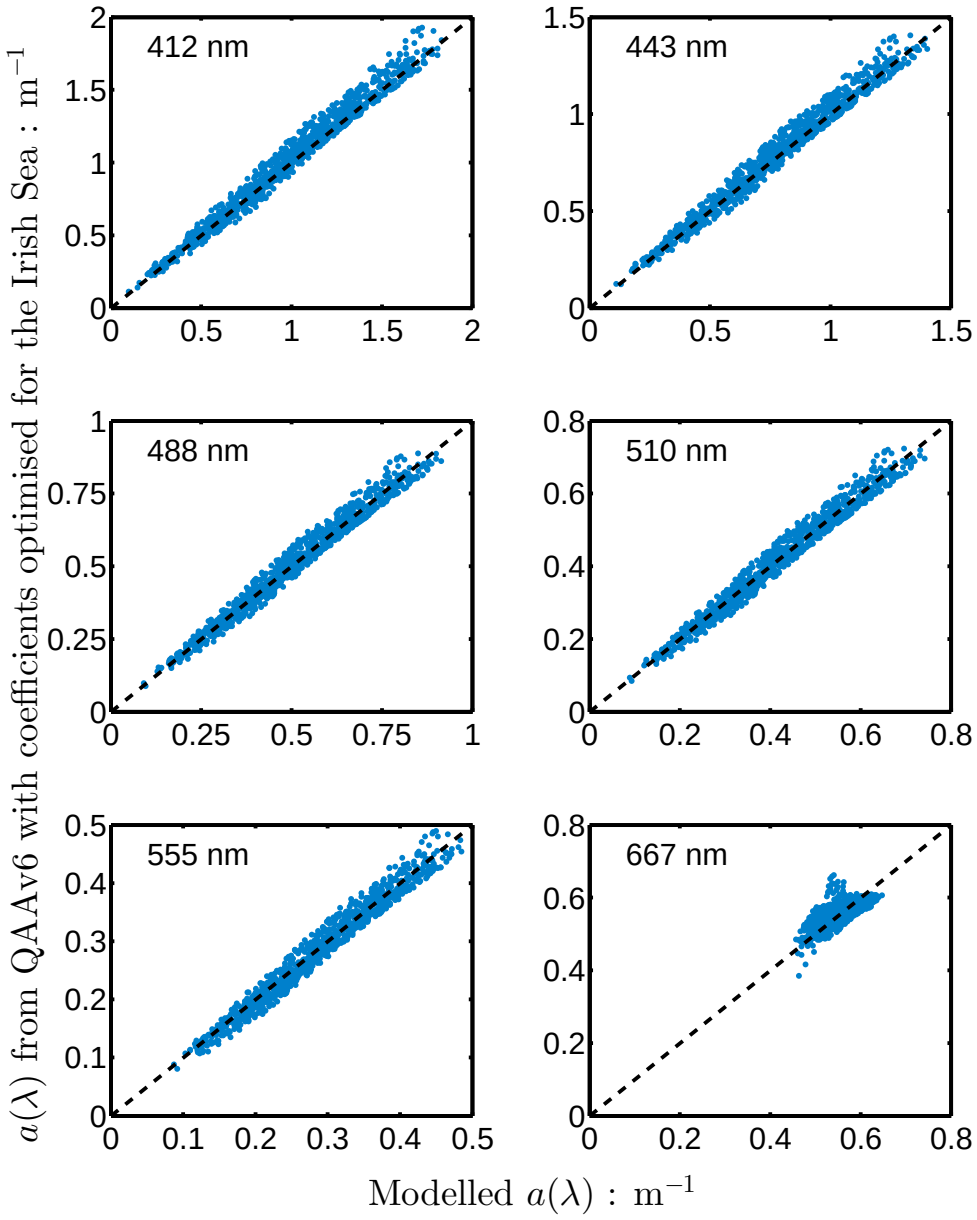

Figure 4.2: The performance of QAAv6 with coefficients optimised for the Irish Sea in recovering $a(\lambda)$ from remote sensing reflectance for IS-1. The dashed lines are one-to-one lines.

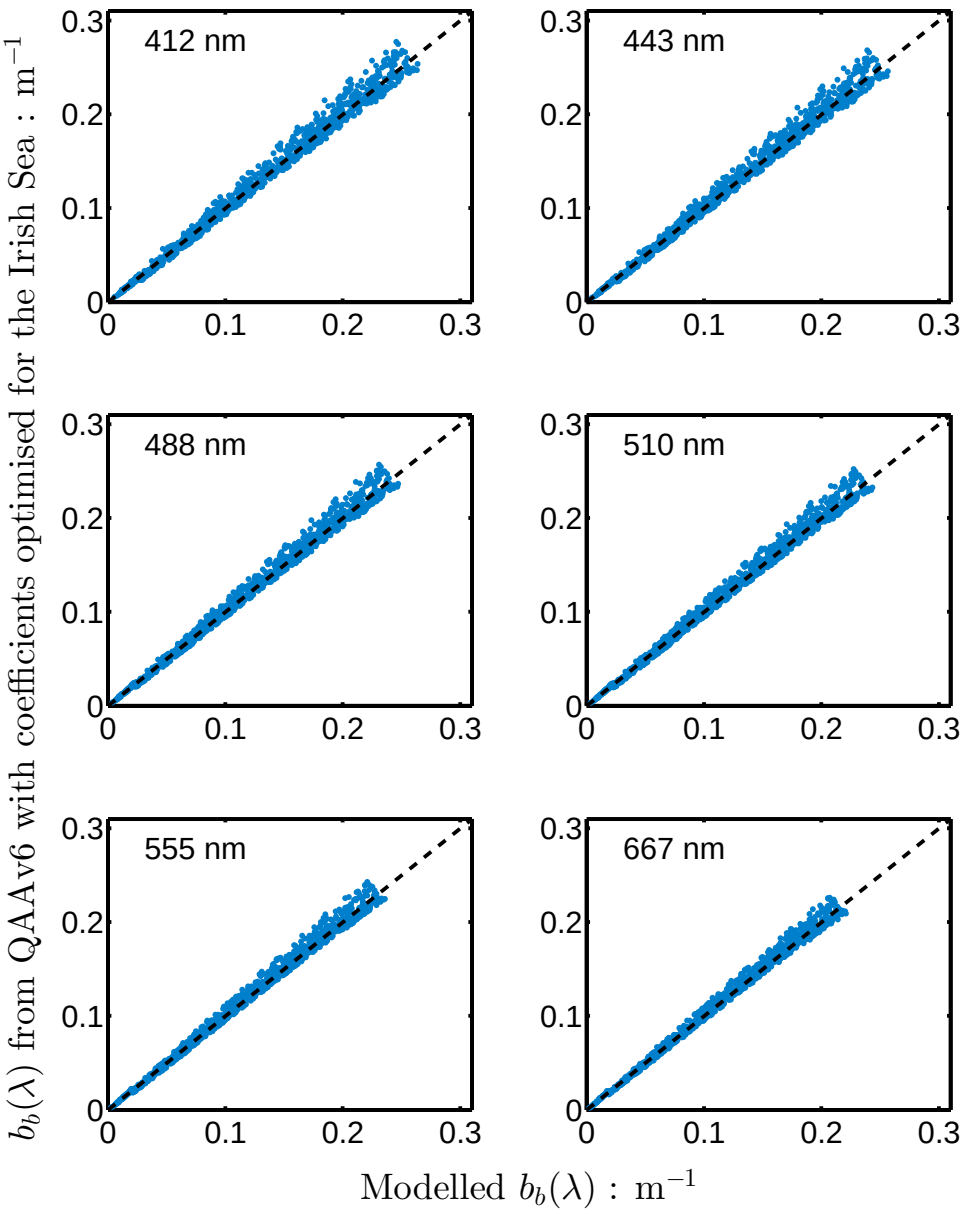

Figure 4.3: The performance of QAAv6 with coefficients optimised for the Irish Sea in recovering $b_b(\lambda)$ from remote sensing reflectance for IS-1. The dashed lines are one-to-one lines.

4.3 Performance of QAAv5 and QAAv6 when Applied to Synthetic Dataset IS-2

When the QAAv6 was applied to IS-2, the resultant recovery of $a(488)$ is shown in Figure 4.4 (a). The main aspects of the recovery were similar for all the wavelengths examined. For this dataset, the spread in the $a(488)$ recovery was a lot larger than for IS-1, particularly at the higher absorption values. On examining this result, it was found that the points which were obtained from an initial estimation of the absorption coefficient at the 'switched' waveband of 667 nm, rather than 555 nm, were the points which were under-performing. The estimation of $a(667)$ uses a simple band ratio which was tuned on the synthetic dataset created by Lee et al. (2002) in the initial QAA paper. This dataset was generated in a similar manner to the IOCCG synthetic dataset, with the same assumptions of covariance between [CHL] and both gelbstoff and detritus absorption. However, in the Irish Sea, high incidences of minerals tend to coincide with low levels of phytoplankton and vice versa. Therefore the dataset of Lee et al. (2002) does not fully capture the variability of the IOPs in the Irish Sea, and the empirical $a(667)$ estimation does not work when applied to this region.

QAAv5, which was tuned on the IOCCG synthetic dataset, only estimates the absorption at 555 nm (or a close green wavelength) and relies on a more complex combination of five different R_{rs} wavebands. The complex form of this estimation provides a more seamless transition between different water types and captures the variability seen in the Irish Sea more closely than a simple band ratio. Hence, QAAv5 was then applied to IS-2, again with the result for $a(488)$ shown in Figure 4.4 (b). This version of the algorithm significantly reduced the spread of the

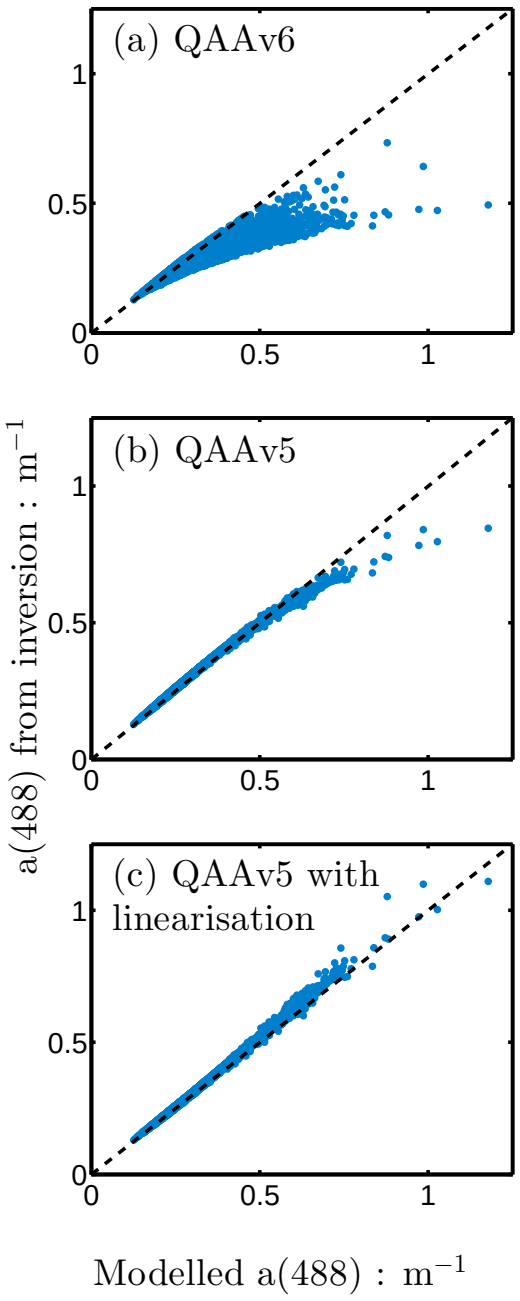

Figure 4.4: The performance of (a) QAAv6, (b) QAAv5 and (c) QAAv5 with a linearisation step, in recovering $a(488)$ from remote sensing reflectance for IS-2. The dashed lines are one-to-one lines.

recovery. However at the higher absorption values the algorithm began to saturate as the non-water term dominated the $a(555)$ estimation. Therefore, by applying a linearisation step to QAAv5 recovered absorption values, the saturation effect was removed (Figure 4.4 (c)). The linearisation step involved applying a cubic polynomials of the form

$$a(\lambda) = k_1 a_{\mathrm{QAA}}(\lambda) + k_2 a_{\mathrm{QAA}}(\lambda)^2 + k_3 a_{\mathrm{QAA}}(\lambda)^3, \tag{4.3}$$

to QAAv5 recovered $a(\lambda)$ values. The coefficients were determined from a least squares fit to the IS-2 dataset and are listed in Table 4.4. Regression results for QAAv5 plus subsequent linearisation are shown for $a(\lambda)$ and $b_b(\lambda)$ in Table 4.5.

Wavelength (nm)	k_1	k_2	k_3
412	0.88	0.22	-0.05
443	0.98	-0.15	0.32
488	1.06	-0.53	0.98
510	1.07	-0.72	1.57
531	1.09	-0.97	2.38
547	1.06	-0.93	3.03
555	1.10	-1.13	3.32
667	2.39	-4.75	4.06

Table 4.4: The coefficients of the cubic polynomials (Eq. 4.3) for linearising QAAv5 absorption coefficient recoveries.

Parameter	gradient	R^2	RMSE (m^{-1})	MPE
$a(412)$	1.03	0.99	0.014	3.1
$a(443)$	1.04	1.00	0.009	1.9
$a(488)$	1.05	1.00	0.005	3.1
$a(510)$	1.05	1.00	0.004	3.1
$a(531)$	1.05	1.00	0.004	3.0
$a(547)$	1.08	0.99	0.003	2.9
$a(555)$	1.04	0.99	0.003	3.8
$a(667)$	1.20	0.98	0.008	3.3
$b_b(412)$	1.00	1.00	0.001	4.3
$b_b(443)$	1.00	1.00	0.001	3.1
$b_b(488)$	1.00	1.00	0.001	2.8
$b_b(510)$	1.00	1.00	0.001	3.0
$b_b(531)$	1.00	1.00	0.0009	2.7
$b_b(547)$	0.99	1.00	0.0009	2.5
$b_b(555)$	0.99	1.00	0.0009	2.4
$b_b(667)$	0.99	1.00	0.0009	1.4

Table 4.5: Regression results for QAAv5 plus linearisation on synthetic dataset IS-2

4.4 Validation of QAAv5 with Linearisation and QAAv6 with Optimised Coefficients on Field Data

When validating the algorithms on the field data, QAA versions were applied to the SPMR measured $R_{rs}(\lambda)$ values and the resultant estimates of $a(\lambda)$ and $b_b(\lambda)$ were compared with the ac-9 and hs-2 measurements. Hence, not only were we testing the performance of an algorithm, but also the performance of three different instruments at measuring closely related properties, each with slightly different wavebands. It is worth noting that the centre of most wavebands only

differ by 3 nm or less, however the red wavebands differ by 9 nm (667 nm for the SPMR and 676 nm for the ac-9). To check the closure between the instruments, the relationship between $r_{rs}(\lambda)$ and $b_b/(a+b_b)$ for the field data was investigated. Figure 4.5 shows $r_{rs}(\lambda)$ plotted against $b_b/(a+b_b)$ for both the field and modelled data together, with the theoretical curve of Gordon et al. (1988) (Eq. (2.26)). For $b_b/(a+b_b) < 0.15$ m^{-1} the field data followed the theoretical curve. However above this limit, the field data significantly deviated from the theory. The stations which fell below the curve are the most turbid stations, located in the Bristol Channel. For turbid stations, standard scattering corrections of IOPs are subject to higher errors due to non-negligible absorption in the near-IR. In addition, the extrapolation of SPMR profiles to the surface is more challenging when the optical depth is so shallow, resulting in only a few data points for the extrapolation. Furthermore, the difficulty in obtaining optical closure between radiometric and inherent optical property measurements has been documented across the field for both modelling work and field data, with suggestions that further studies are required to understand the variability observed (Chang et al., 2007; Chang and Whitmire, 2009; Brewin et al., 2013).

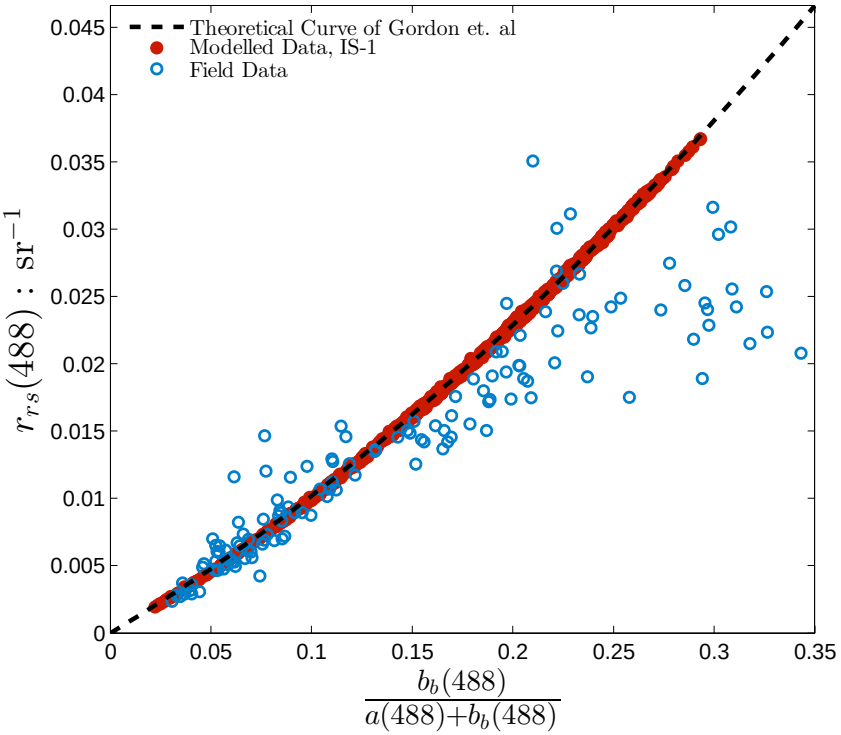

Figure 4.5: The relationship between the sub-surface remote sensing reflectance, r_{rs} and the absorption and backscattering coefficients at 488 nm. The filled red symbols represent the modelled data, IS-1, the unfilled blue symbols represent the field data and the dashed curve represents the theoretical curve of Gordon et al. (1988) with coefficients taken from Lee et al. (2002).

Absorption and Backscattering Coefficients

The two adjusted versions of the QAA, (i) QAAv5 with subsequent linearisation and (ii) QAAv6 with optimised coefficients, were applied to field data collected in the Irish Sea and surrounding waters. Details of the methods used to collect and analyse the field data are given in Section 3.1. The regression results for $a(\lambda)$ and $b_b(\lambda)$ are given in Table 4.6 and shown (for 488 nm) in Figure 4.6.

Parameter	Algorithm	gradient	y-intercept (m^{-1})	R^2	RMSE (m^{-1})
$a(412)$	QAAv5 + lin	1.94	-0.08	0.70	0.22
	QAAv6 opt	1.94	-0.055	0.75	0.19
$b_b(412)$	QAAv5 + lin	1.03	0.003	0.94	0.003
	QAAv6 opt	1.09	0.002	0.89	0.005
$a(443)$	QAAv5 + lin	1.09	0.017	0.80	0.08
	QAAv6 opt	1.18	0.021	0.86	0.068
$b_b(443)$	QAAv5 + lin	1.01	0.002	0.94	0.003
	QAAv6 opt	1.09	0.002	0.90	0.004
$a(488)$	QAAv5 + lin	1.03	0.022	0.84	0.043
	QAAv6 opt	1.16	0.013	0.87	0.042
$b_b(488)$	QAAv5 + lin	1.00	0.002	0.94	0.003
	QAAv6 opt	1.08	0.002	0.90	0.004
$a(510)$	QAAv5 + lin	0.90	0.027	0.82	0.035
	QAAv6 opt	1.04	0.017	0.85	0.037
$b_b(510)$	QAAv5 + lin	1.00	0.002	0.93	0.003
	QAAv6 opt	1.08	0.002	0.90	0.004
$a(555)$	QAAv5 + lin	0.91	0.021	0.84	0.022
	QAAv6 opt	1.06	0.008	0.85	0.025
$b_b(555)$	QAAv5 + lin	0.99	0.002	0.93	0.003
	QAAv6 opt	1.07	0.002	0.90	0.004
$a(667)$	QAAv5 + lin	0.65	0.22	0.057	0.10
	QAAv6 opt	0.75	0.17	0.15	0.068
$b_b(667)$	QAAv5 + lin	0.95	0.002	0.93	0.0029
	QAAv6 opt	1.02	0.002	0.91	0.004

Table 4.6: The regression results for QAAv5 with linearisation and the optimised QAAv6 for $a(\lambda)$ and $b_b(\lambda)$. The regression results for $b_b(\lambda)$ are determined for in situ values with $b_b(\lambda)$ smaller than 0.05 m^{-1} .

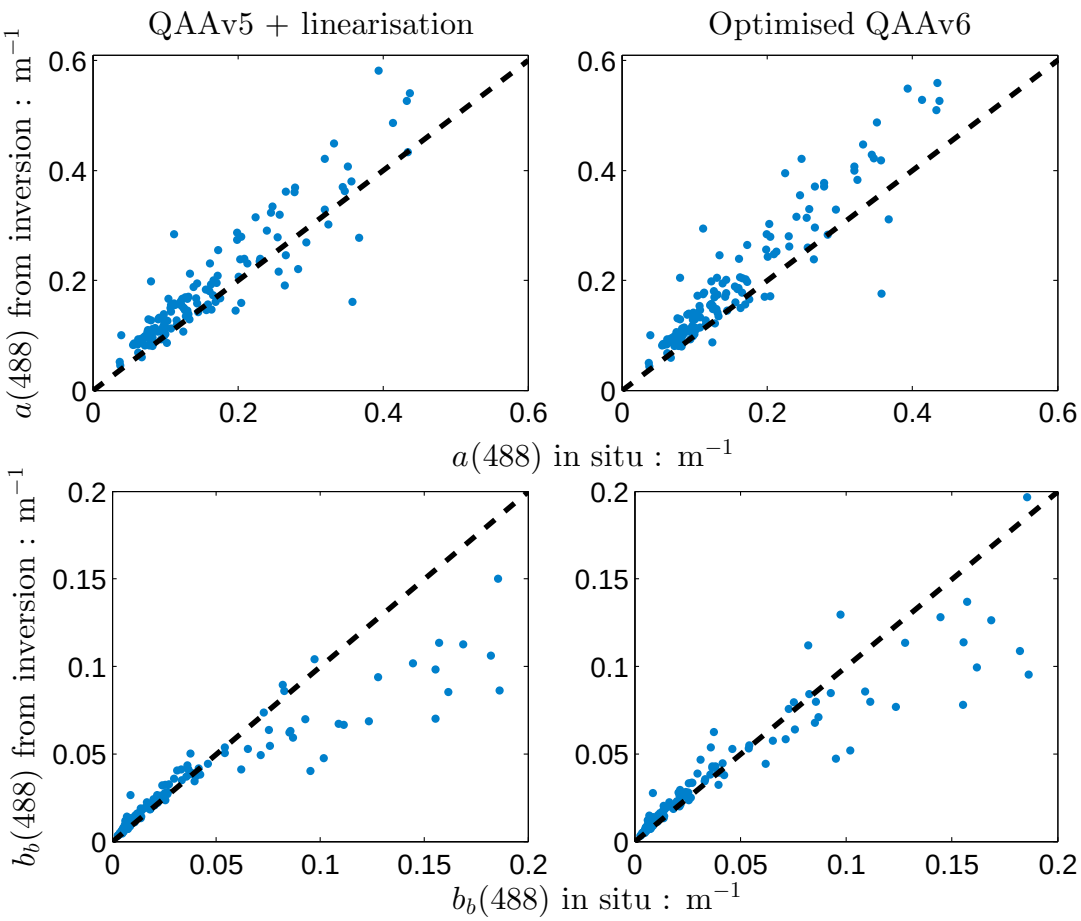

Figure 4.6: The performance of QAAv5 with linearisation and the optimised QAAv6 on in situ data, shown for 488 nm. The dashed lines are one-to-one lines.

The performance of the two different algorithms were very similar for the absorption coefficients. Generally, $a(\lambda)$ tended to be overestimated, however the gradients were close to unity for all wavebands except at 412 nm and 667 nm, and the R^2 and RMSE values were similar. The performance in the 412 nm waveband was poor, probably indicating a problem with the 412 nm channel in the SPMR instrument rather than a failure of the algorithm itself. The recovered values of $a(667)$ were also poor, partly because there was a mis-match in the wavelengths being compared (667 nm with 676 nm), and partly because QAA doesn't work for

wavelengths longer than the one that was initially used to estimate the absorption coefficient (Brewin et al., 2013). For the field data, 68 out of the 146 stations were determined from an absorption estimation at 667 nm, leaving 78 stations with an initial estimation of $a(555)$, hence recovered absorption coefficients at wavelengths longer than 555 nm for these stations cannot be trusted.

The recovered backscattering coefficients below 0.05 m^{-1} were well correlated with those measured in situ. However, for $b_b(\lambda) > 0.05$ m^{-1}, both versions of QAA significantly underestimated $b_b(\lambda)$. These underestimated stations are the turbid Bristol Channel stations, previously identified in Figure 4.5, for which there is not full closure between the optical and radiometry measurements. The regression results for the stations with $b_b(\lambda) < 0.05$ m^{-1} are given in Table 4.6, showing the gradients were consistently closer to unity for QAAv5 plus linearisation, however, the R^2 and RMSE values were very similar for both versions of the algorithm.

Overall, the performance of the adjusted QAAv5 and QAAv6 in the recovery of the absorption and backscattering coefficients in the Irish Sea were very similar. However, the QAAv5 plus linearisation did consistently perform marginally better across the majority of wavelengths when considering both the modelled datasets and the field data, and hence was selected for use in future analysis.

Mean Diffuse Attenuation Coefficients

The three different versions of the KdLee algorithm outlined at the start of this chapter were tested on the field data, by applying QAAv5 plus linearisation to SPMR calculated $R_{rs}(\lambda)$ and using the resultant $a(\lambda)$ and $b_b(\lambda)$ values to estimate $\overline{K}_d(\lambda)$. In this case, the algorithm validation is done using only one instrument (the SPMR), avoiding errors arising from closure between instruments. The three

algorithms performed similarly across all wavebands, with regression results given in Table 4.7 and recoveries plotted for the 490 nm waveband in Figure 4.7. The original (Lee et al., 2005b) and updated (Lee et al., 2013) algorithms produced a very similar performance, but the updated algorithm gave gradients closer to unity, except in the 412 nm waveband. On the other hand, the form of the simplified algorithm is suitable for examining the separate effects of absorption and scattering on the resultant light attenuation. Therefore, depending on the application, either of the three algorithms can be used without losing much in terms of accuracy of recovery.

Wavelength	Algorithm	gradient	y-intercept (m^{-1})	R^2	RMSE (m^{-1})
412	KdLee	1.49	-0.11	0.89	0.18
	KdLee_simp	1.44	-0.10	0.89	0.18
	KdLee_2013	1.50	-0.11	0.90	0.18
443	KdLee	0.97	0.03	0.89	0.11
	KdLee_simp	0.91	0.04	0.87	0.11
	KdLee_2013	0.98	0.03	0.89	0.11
490	KdLee	0.88	0.03	0.94	0.06
	KdLee_simp	0.81	0.05	0.92	0.06
	KdLee_2013	0.89	0.03	0.94	0.06
510	KdLee	0.82	0.03	0.95	0.05
	KdLee_simp	0.74	0.05	0.94	0.05
	KdLee_2013	0.83	0.03	0.95	0.05
555	KdLee	0.77	0.03	0.96	0.03
	KdLee_simp	0.70	0.05	0.96	0.03
	KdLee_2013	0.78	0.03	0.96	0.03
667	KdLee	0.41	0.50	0.24	0.1
	KdLee_simp	0.33	0.54	0.17	0.14
	KdLee_2013	0.42	0.50	0.25	0.14

Table 4.7: The regression results for the three different versions of the KdLee algorithm on the field data.

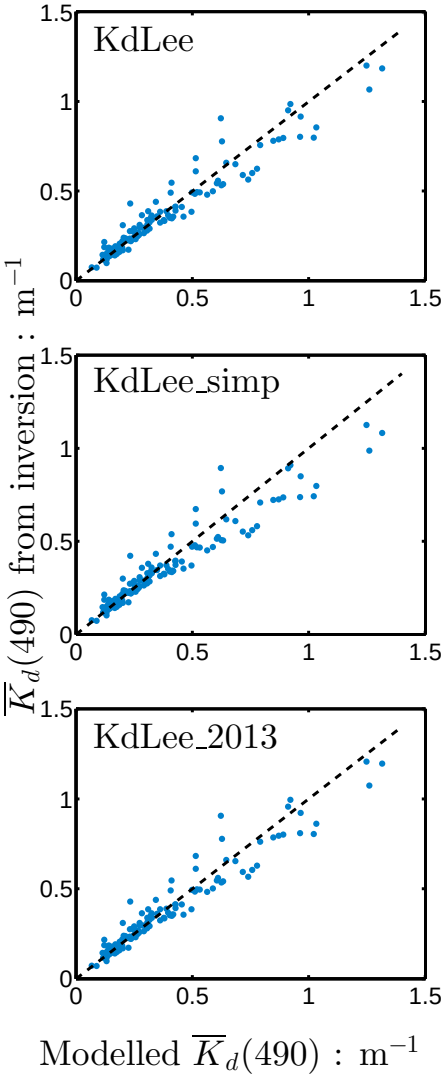

Figure 4.7: The performance of three different versions of the KdLee algorithm on in situ data. The dashed lines are one-to-one lines.

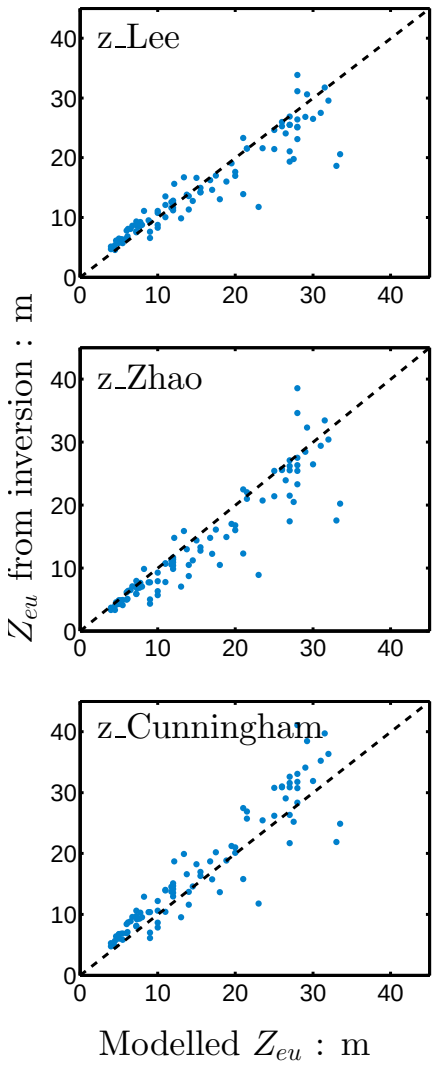

Figure 4.8: The performance of three different euphotic depth algorithms on in situ data. The dashed lines are one-to-one lines.

Euphotic Depth Algorithm Comparisons with Field Data

The three different euphotic depth algorithms outlined at the start of this chapter were tested on the field data. First, QAAv5 with linearisation was applied to the $R_{rs}(\lambda)$, then $\overline{K}_d(490)$ was estimated using the updated KdLee algorithm, and the resultant $a(490)$, $b_b(490)$ and $\overline{K}_d(490)$ were used to determine the euphotic depths. The Cunningham et al. (2013) algorithm was slightly adjusted to obtain new coefficients based on the modelled dataset, IS-1:

$$z = 5.52\overline{K}_d(490)^{-0.86}. \tag{4.4}$$

The algorithms all gave similar results (Table 4.8 and Figure 4.8), but the algorithm of Cunningham et al. (2013) gave a gradient closest to unity and so was selected to use for all the subsequent analysis.

Algorithm	gradient	y-intercept (m)	R^2	RMSE (m)
z_Lee	0.80	2.27	0.88	2.7
z_Zhao	0.91	-0.34	0.85	3.5
z_Cunningham	1.05	0.92	0.85	3.9

Table 4.8: The regression results for three different euphotic depth algorithms on the field data

4.5 Discussion

The main conclusions from this chapter can be summarised as follows:

1. The quasi-analytical approach of Lee et al., with relatively small adjustments, produced excellent results when applied to both modelled datasets for the Irish Sea. The quality of the $a(\lambda)$ and $b_b(\lambda)$ recoveries for the field data was lower, but this may have been due to measurement difficulties rather than the algorithm itself. QAAv5 with linearisation performed marginally better across the majority of wavelengths when considering both the absorption and backscattering coefficients, and hence this version was selected for use inl subsequent analyses.

2. Three different versions of the Lee et al. (2005b) algorithm for recovering $\overline{K}_d(\lambda)$ were evaluated: the original version, a simplified version (Lee et al., 2005b) and an updated version (Lee et al., 2013). All three versions of the algorithm recovered coefficients which were correlated with the field measurements between 443 and 555 nm. This was particularly encouraging, as a previous study in the Irish Sea (McKee et al., 2007) showed that the empirical $\overline{K}_d(490)$ algorithm (Mueller, 2000) performed poorly.

3. Euphotic depths estimated by the Lee et al. (2007), Zhao et al. (2013) and Cunningham et al. (2013) algorithms were well correlated with the field measurements, with average percentage errors similar to those reported by Lee et al. (2007). The Lee et al. (2007) algorithm had the highest coefficient of determination and RMSE, but was computationally expensive. However, both the Zhao et al. (2013) and Cunningham et al. (2013) algorithms have a simpler form and recovered the euphotic depth to a similar accuracy, with

the Cunningham et al. (2013) algorithm giving a gradient closest to one. Hence, this algorithm was chosen for future use.

5. Remote Sensing of Separate Absorption Coefficients for Phytoplankton Cells and Mineral Particles

The aim of deriving concentrations of the optically significant materials present in the water column directly from ocean colour imagery still poses significant challenges, particularly in optically complex waters (Aurin and Dierssen, 2012; Odermatt et al., 2012). However, the ability to quantify the contributions of phytoplankton cells and mineral particles to the total absorption coefficient without specifically deriving constituent concentrations has important potential applications. These include studies of the role of different particle classes on the attenuation of light (Devlin et al., 2008) and the detection of chlorophyll in regions where conventional algorithms are degraded by turbidity (Dall'Olmo and Gitelson, 2005).

In this chapter, an approach for recovering phytoplankton and mineral absorption coefficients from the remote sensing reflectance, is presented. This absorption partitioning procedure assumes CDOM has a relatively low and constant background influence on the total absorption, and phytoplankton and mineral particles are the main contributors to the optical variability. This condition appears to be met in many shelf sea areas including the Patagonian shelf (Ferreira et al., 2009),

certain regions in the North Sea (Tilstone et al., 2012) and the Irish Sea (Bowers et al., 2013)).

The absorption partitioning technique was initially developed using dataset IS-2 which was derived from a bio-optical model of the Irish Sea (see Section 4.1 for a full description). Eight years of MODIS data for the Irish Sea obtained from partially cloud-free images were then examined to investigate the variability in the IOPs, with application of the absorption partitioning procedure to a patch in the eastern Irish Sea to understand the observed patterns (see Section 3.3 for full details on the satellite data processing).

5.1 Methods

The absorption partitioning procedure separates the contribution of phytoplankton and mineral particles to the total absorption coefficient by examining the relationship between the particulate absorption and backscattering coefficients. Following the evaluation of Chapter 4, the total absorption and backscattering coefficients were derived from remote sensing reflectance using the QAAv5 with linearisation (see Section 4.3 for a full description and evaluation).

Absorption Partitioning

If we assume the optical properties of the water column are due to the effects of phytoplankton (CHL), suspended minerals (MSS) and CDOM, then

$$a(\lambda) = a_w(\lambda) + a_{\mathrm{CHL}}(\lambda) + a_{\mathrm{MSS}}(\lambda) + a_{\mathrm{CDOM}}(\lambda), \tag{5.1}$$

$$b_b(\lambda) = b_{bw}(\lambda) + b_{b\mathrm{CHL}}(\lambda) + b_{b\mathrm{MSS}}(\lambda). \tag{5.2}$$

The backscattering to absorption ratio for each particle class can be defined as,

$$\rho_1(\lambda) = \frac{b_{b\mathrm{MSS}}(\lambda)}{a_{\mathrm{MSS}}(\lambda)} \tag{5.3}$$

$$\rho_2(\lambda) = \frac{b_{b\mathrm{CHL}}(\lambda)}{a_{\mathrm{CHL}}(\lambda)}. \tag{5.4}$$

Therefore, by combining (5.2), (5.3) and (5.4), the particulate absorption and backscattering coefficients can be expressed in terms of $a_{\mathrm{CHL}}(\lambda)$ and $a_{\mathrm{MSS}}(\lambda)$,

$$a_p(\lambda) = a(\lambda) - a_w(\lambda) - a_{\mathrm{CDOM}}(\lambda) = a_{\mathrm{MSS}}(\lambda) + a_{\mathrm{CHL}}(\lambda) \tag{5.5}$$

$$\begin{aligned} b_{bp}(\lambda) = b_b(\lambda) - b_{bw}(\lambda) &= b_{b\mathrm{MSS}}(\lambda) + b_{b\mathrm{CHL}}(\lambda) \\ &= \rho_1(\lambda) a_{\mathrm{MSS}}(\lambda) + \rho_2(\lambda) a_{\mathrm{CHL}}(\lambda). \end{aligned} \tag{5.6}$$

From (5.5) and (5.6), we can derive expressions for $a_{\mathrm{CHL}}(\lambda)$ and $a_{\mathrm{MSS}}(\lambda)$:

$$a_{\mathrm{CHL}}(\lambda) = \frac{\rho_1(\lambda) a_p(\lambda) - b_{bp}(\lambda)}{\rho_1(\lambda) - \rho_2(\lambda)}, \tag{5.7}$$

$$a_{\mathrm{MSS}}(\lambda) = \frac{b_{bp}(\lambda) - \rho_2(\lambda) a_p(\lambda)}{\rho_1(\lambda) - \rho_2(\lambda)}. \tag{5.8}$$

Hence for a given $a_p(\lambda)$ and $b_{bp}(\lambda)$, if the ratio of the backscattering to absorption coefficients for each constituent is known, then the particulate absorption can be decomposed into its contributions. Further, if the specific absorption coefficients are known, the constituent concentrations can be estimated from their absorption contributions.

A plot of the backscattering coefficient against the absorption coefficient at one wavelength, λ_0, for a group of observations has an upper and lower bound (see Figure 5.1). These upper and lower bounds are the backscattering to ab-

sorption ratios for MSS (ρ_1) and CHL (ρ_2) respectively. The presence of CDOM, which is only an absorber, would shift a point along the absorption axis. Hence, for a system with a relatively constant influence from CDOM, the whole data cloud would be shifted along by approximately the same amount. Therefore from the offset along the absorption axis we can gain an estimation of the CDOM contribution, as shown in Figure 5.2. If we consider a point (A in Figure 5.2) that contains MSS (in addition to this CDOM contribution), then this point will lie on the ρ_1 line. Similarly, a point (B) containing CHL (and the background CDOM), will lie on the ρ_2 line. Then point C, containing a combination of MSS, CHL and CDOM, lies inbetween the two lines. This point can be thought of in two ways: (1) having been pulled down from the ρ_1 line because of the addition of CHL, hence the vertical distance between the ρ_1 line and C is proportional to the amount of CHL added, or (2) being pulled up from the ρ_2 line, with the vertical distance it is pulled up attributed to the amount of MSS added. Hence the form of Eqs. (5.7) and (5.8).

Determination of ρ_1 , ρ_2 and a_0

Figures 5.1 and 5.2 show how, for a given set of shelf sea observations, the backscattering to absorption ratios have upper and lower bounds. Hence, for a given dataset, if the space is well-populated the backscattering to absorption ratios for each particle class (ρ_1 and ρ_2) can be estimated from the data itself.

To determine ρ_1 and ρ_2 the first step is to obtain the particulate absorption and backscattering coefficients. For the backscattering this is a straightforward subtraction of the known water component (Smith and Baker, 1981) from the total backscattering. However, for the absorption both the water component

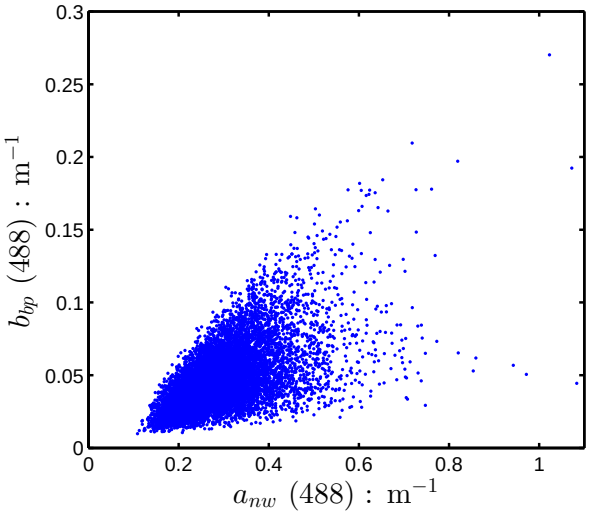

Figure 5.1: A plot of the particulate backscattering coefficient against non-water absorption coefficient at 488 nm for modelled dataset IS-2.

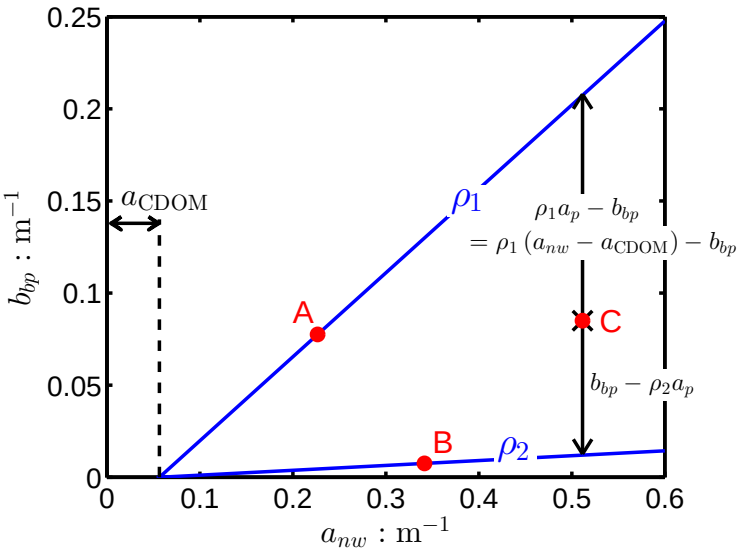

Figure 5.2: The relationship between $b_{bp}(\lambda_0)$ and $a_{nw}(\lambda_0)$ for a given wavelength, λ_0. The blue lines indicate the upper and lower bounds (which have gradients ρ_1 and ρ_2 respectively) for any data point. For the three points shown (A, B & C), CDOM = 0.1 m^{-1}, hence the offset from the origin is given by a_{CDOM}. Point A also has [MSS] = 5 g m^{-3}, point B has [CHL] = 5 mg m^{-3} and point C has both [MSS] = 5 g m^{-3} and [CHL] = 5 mg m^{-3}. Therefore A lies on the ρ_1 line, point B lies on the ρ_2 line and C is a distance, $\rho_1 a_p - b_{bp}$, below the ρ_1 line and a distance, $b_{bp} - \rho_2 a_p$, above the ρ_2 line.

(Pope and Fry, 1997) and the CDOM component must be subtracted. Without knowing the CDOM component a priori, a background estimate can be made from the offset of the data cloud from the origin along the absorption axis, as long as CDOM is relatively invariant. For a given set of observations the absorption offset, $a_0 = a_w + a_{\mathrm{CDOM}}$, is estimated by incrementally increasing a_0 from 0 to the minimum absorption value of the dataset. At each value of a_0, ρ_1 can be estimated from the gradient of a line (forced through a_0) which is fitted via the least squares method to the largest 1% of the b_{bp}/a_p values. The sum of the squared distances from every point to this least squares line, ε, is used as a descriptor for the effectiveness of the fit of this line to the whole dataset. For a given data point (a_i, b_{bi}), let d_i be the shortest distance of the point to the line and (a, b_b) be the point on the line at this shortest distance, then

$$\varepsilon = \sum_{i=1}^{n} d_i^2 = \sum_{i=1}^{n} (a - a_i)^2 + (b_b - b_{bi})^2 = \sum_{i=1}^{n} \frac{(b_{bi} - \rho_1 a_i + \rho_1 a_0)^2}{\rho_1^2 + 1}. \tag{5.9}$$

The values of a_0 and ρ_1 selected to use are those from the iteration where this descriptor is a minimum. Finally, ρ_2 is determined from the gradient of a line, forced through the chosen a_0, fitted through the smallest 1% of the b_{bp}/a_p values.

5.2 Performance of the Absorption Partitioning Method

When the procedure outlined in Section 5.1 was applied to IS-2, with $\lambda_0 =$ 488 nm, the derived parameters differed slightly from those used in creating the dataset, with $\rho_1 = 0.432$ (rather than 0.456), $\rho_2 = 0.057$ (rather than 0.026) and $a_0 = 0.082$ (rather than 0.072). These differences arose mainly from the fact that

the data cluster did not fully sample the available parameter space (Figure 5.3).

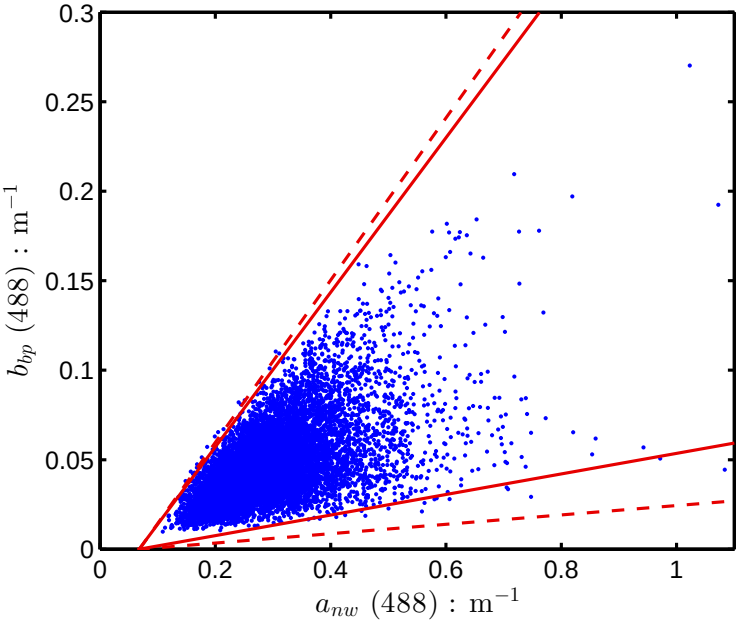

Figure 5.3: The QAA-derived particulate backscattering and non-water absorption for the modelled dataset, with the dashed lines indicating the boundaries defined by the SIOPs and the solid lines indicating the boundaries derived from the line fitting procedure described in the text.

Applying the absorption partitioning equations to the modelled dataset, with the values of ρ_1 , ρ_2 and a_0 obtained from the fitting procedure, $a_{\mathrm{CHL}}(488)$ and $a_{\mathrm{MSS}}(488)$ were recovered with gradients of 1.11 and 1.06 respectively and coefficients of determination of 0.94 and 0.97 (Figure 5.4).

5.3 Sensitivity of Absorption Partitioning to CDOM Variability

The absorption partitioning procedure was developed on the assumption that CDOM was not highly variable. The effect of this assumption on the recoveries of

$a_{\mathrm{CHL}}(488)$ and $a_{\mathrm{MSS}}(488)$ was investigated by altering the CDOM distributions used in the modelled dataset. Five different modal values of CDOM were selected, and in each case the coefficient of variation was varied. Figure 5.5 shows the RMSEs for the recovered $a_{\mathrm{CHL}}(488)$ and $a_{\mathrm{MSS}}(488)$ when the different CDOM distributions were used to generate the modelled dataset. For the CDOM distribution that is representative of the Irish Sea (CDOM mode $= 0.12$ m^{-1}, coefficient of variation $= 0.23$, see Table 4.1), the RMSEs were 0.009 m^{-1} for $a_{\mathrm{MSS}}(488)$ and 0.02 m^{-1} for $a_{\mathrm{CHL}}(488)$.

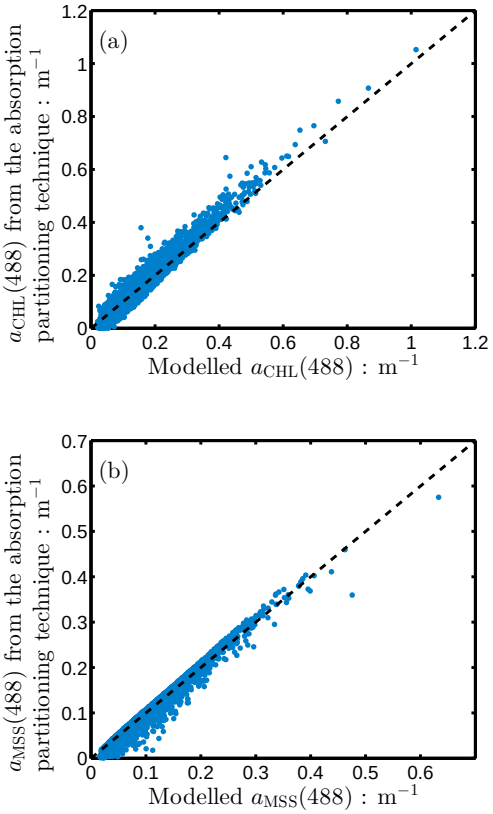

Figure 5.4: Recoveries of (a) $a_{\mathrm{CHL}}(488)$ and (b) $a_{\mathrm{MSS}}(488)$ for IS-2 using the absorption partitioning technique.

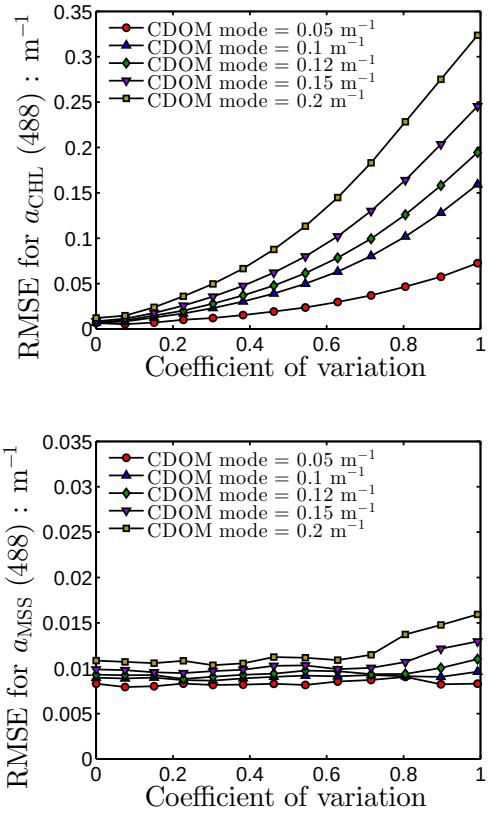

Figure 5.5: The effect of increasing variability in the CDOM distribution on the RMSE in the recovery of a_{CHL} (top figure) and a_{MSS} (bottom figure).

5.4 Application of QAA and Absorption Partitioning Procedure to Satellite Ocean Colour Observations

The QAAv5 plus subsequent linearisation was applied to remote sensing reflectance data obtained from eight years of MODIS data covering the Irish Sea and surrounding waters. Figure 5.6 shows the extent of the region considered. The full time series at the indicated location (A) is examined using the absorption partitioning procedure later in the chapter.

ρ_1, ρ_2 and a_0 Derived from MODIS Data

The values of $a(488)$ and $b_b(488)$ were determined using the QAAv5 with linearisation for all available observations. By subtracting the known water contributions, ρ_1, ρ_2 and a_0 were determined for all the available satellite data, see Figure 5.7. The value for ρ_1 was determined to be 0.413, close to the value of 0.456 which was determined from the mean SIOPs (Table 3.1). On the other hand, ρ_2 was significantly lower than the SIOP value (0.007 from MODIS data, 0.026 from SIOPs). This difference could arise from the difficulty in measuring the phytoplankton backscattering coefficients (McKee and Cunningham, 2006). The absorption offset (a_0) was lower from the MODIS data (0.024) than the modal value used in the modelling (0.072), supporting the low CDOM assumption.

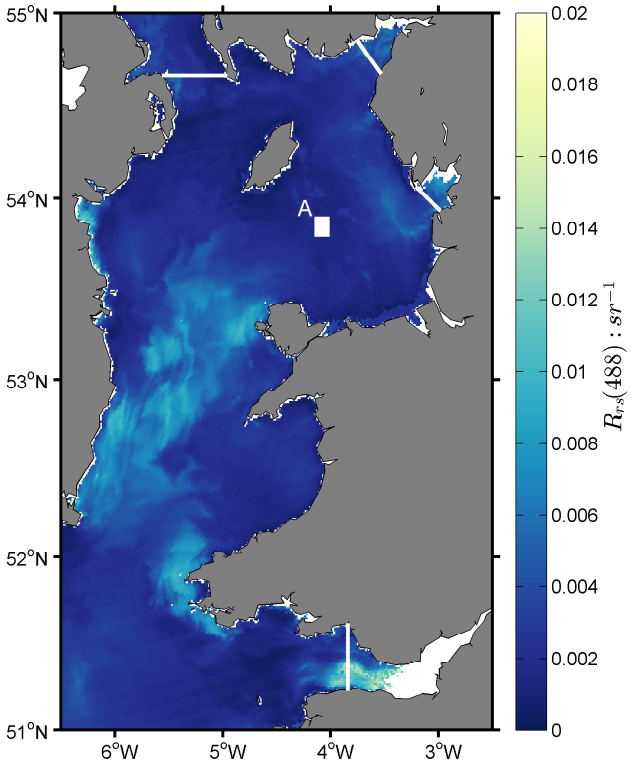

Figure 5.6: A typical MODIS $R_{rs}(488)$ image of the Irish Sea from 26th May 2012. The lines indicate areas indicate the boundaries of the region used in the absorption partitioning analysis. Point A was used for time series analysis, see later in text.

IOP Characteristics of the Irish Sea

By grouping all the $b_{bp}(488)$ and $a(488)$ data into two-week intervals according to the time of occurrence in the calendar year, the temporal variability in backscattering to absorption ratios (an indicator of particle class) was examined. Figure 5.8 shows plots of $b_{bp}(488)$ against $a(488)$ for the whole region for two-week intervals, with the boundary lines derived from the whole dataset. At the start of the year, all the data were clustered near the upper boundary, indicating the presence of mineral particles in the surface layer of the water column across

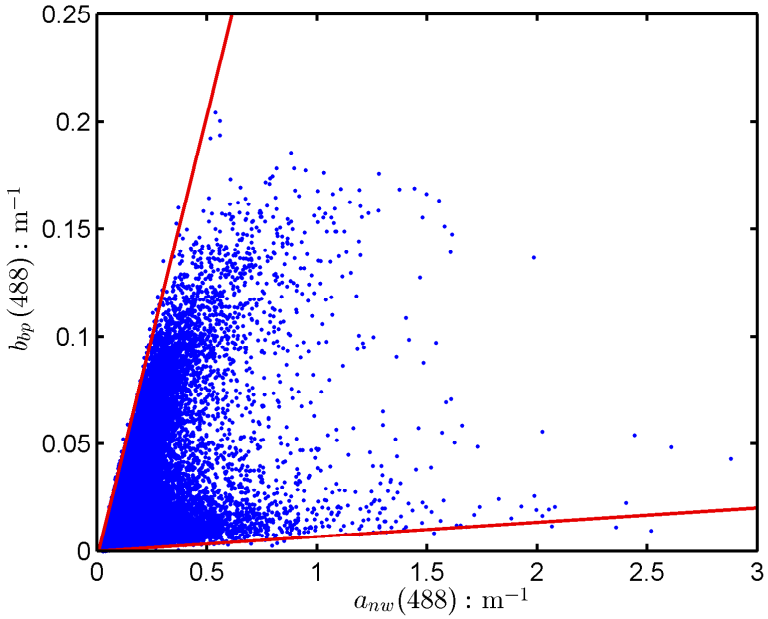

Figure 5.7: A plot of $b_{bp}(488)$ against $a_{nw}(488)$ for all the available MODIS observations within the region shown in Figure 5.6. The solid red lines indicate the ρ_1 and ρ_2, as determined from the fitting procedure, which were used for the absorption partitioning.

the region. During the spring a distinct separate group of points appeared close to the lower (phytoplankton) boundary when the spring phytoplankton bloom occurred. By late spring, when many of the mineral particles had dropped out of the surface layer, the data cluster had moved away from the upper boundary. During summer and into autumn, this process reversed, with points moving up from the lower boundary tying in with the decline in the phytoplankton population, although a small reappearance was seen in September, coinciding with the secondary phytoplankton bloom often observed in the autumn. Finally, at the end of the year we have a moved in a full cycle, and the water column was dominated by mineral particles in the surface layer.

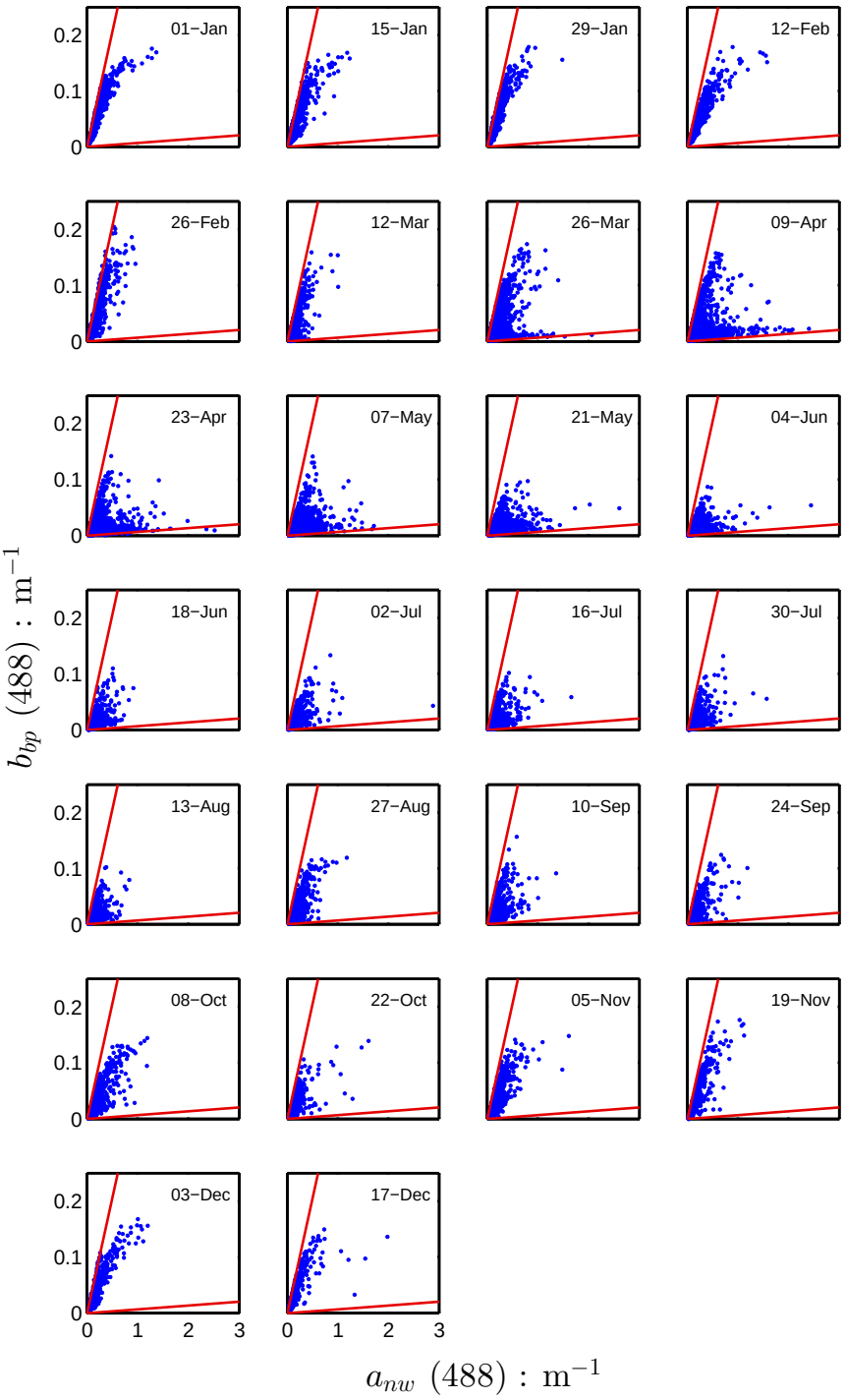

Figure 5.8: Fortnightly plots of $b_{bp}(488)$ against $a_{nw}(488)$ for all the available data within the region shown in Figure 5.6 between January 2005 and December 2012. The solid red lines are the ρ_1 and ρ_2 determined for all the data (see Figure 5.7), and the date is the start of each fortnight.

Time Series of $a_{\mathrm{CHL}}(488)$ and $a_{\mathrm{MSS}}(488)$

All the available MODIS observations of $R_{rs}(488)$, and the QAA derived values of $a(488)$ and $b_b(488)$ over the eight year period at location A are shown in Figure 5.9. The variables all showed annual cycles, with $R_{rs}(488)$ and $b_b(488)$

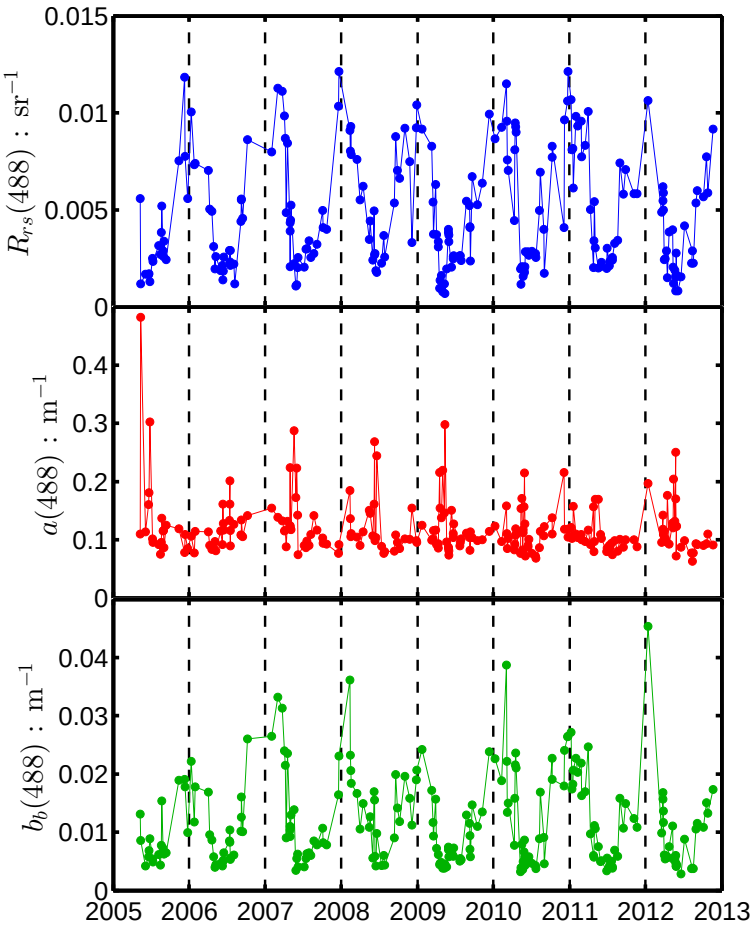

Figure 5.9: All the satellite observations available for $R_{rs}(488)$, $a(488)$ and $b_b(488)$ over the eight year period for the location A.

peaking over the winter months, and having a minimum over the summer. This is consistent with Bowers (2003) who showed wind-enhanced mixing brings min-

eral particles to the surface of the water column during the winter. $a(488)$ had a pronounced peak in the early spring, coinciding with the minima in $R_{rs}(488)$ and $b_b(488)$ cycles.

The $a(488)$ cycle can be examined in more detail by applying the absorption partitioning procedure. Figure 5.10 shows the fractional contribution of $a_{\mathrm{MSS}}(488)$ and $a_{\mathrm{CHL}}(488)$ to the total absorption coefficient at location A. These components were in antiphase, with the mineral particles dominating the total absorption during the winter months and conversely, phytoplankton particles dominating the absorption over the summer.

Since the time series showed no significant long-term trends, the mean annual cycle of the partitioned absorption coefficients was derived by averaging all the available observations for each two-week interval in the calendar year (Figure 5.11). The contrasting cycles of each particle class is evident from Figure 5.11, where the mineral absorption was at a maximum over the winter months and its reduction in the spring coincided with an increase in phytoplankton absorption during the spring bloom.

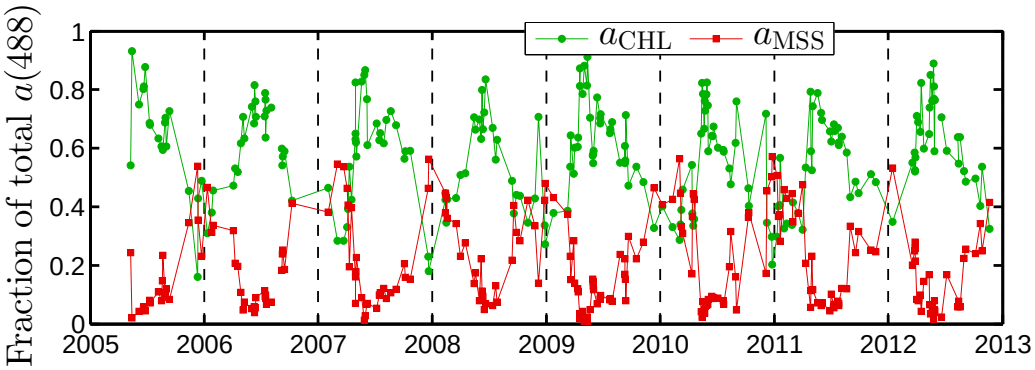

Figure 5.10: The fractional contribution of CHL and MSS to the total absorption coefficient for all the satellite observations from location A.

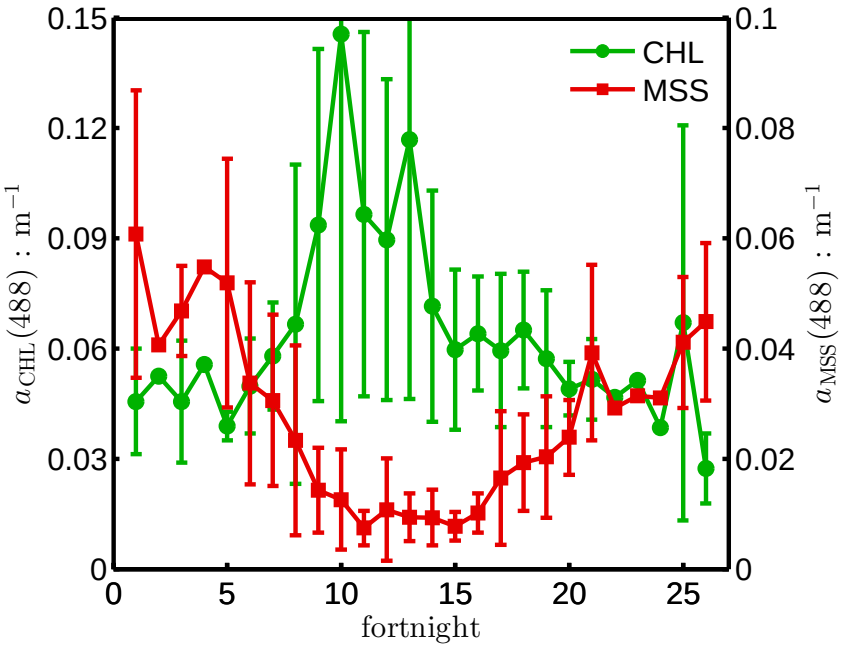

Figure 5.11: Seasonal averages for location A, where the satellite observations were binned by fortnight and the error bars are the standard deviations for each fortnight (which were only calculated when there were 5 or more observations within a given fortnight).

5.5 Discussion

The main points covered in this chapter can be summarised as follows:

1. The absorption partitioning procedure developed depends on two initial assumptions. First, that the contribution of CDOM to the total absorption coefficient is either low or constant, and second, that the remote sensing observations fully fill the parameter space, allowing ρ_1, ρ_2 and a_0 to be determined from the data cluster. There are probably other shelf sea areas where the influence of CDOM on total absorption may be similar to that observed in the Irish Sea. Additionally, if the backscattering to absorption ratios of the main particle classes are known a priori, the data coverage

restriction can be relaxed.

2. The absorption partitioning procedure proposed here was shown to work well using a synthetic data set generated for the Irish Sea using locally determined specific inherent optical properties. When it was applied to MODIS data, it recovered mineral and chlorophyll absorption coefficients which were consistent with previously published studies of the region (Gowen et al., 2008), and also revealed novel temporal relationships between the dynamics of these two particle classes.

6. Role of Different Particle Classes in Determining the Depth of Penetration of Solar Radiation in the Irish Sea

The depth of penetration of solar radiation is an important property in aquatic systems for both physical and biological processes (Bisset et al., 2001; Doron et al., 2007). The diffuse attenuation coefficient provides a measure of penetration depths and how these are affected by the presence of materials in the surface layer (Lee et al., 2005b; Doron et al., 2007; Wang et al., 2009), which is critical for determining heat budgets in the upper mixed regions of the oceans (Lewis et al., 1990; Sathyendranath et al., 1991a), underwater visibility (Doron et al., 2007) and photosynthesis (Platt et al., 1988; Sathyendranath et al., 1989b).

For growth and primary production, phytoplankton cells require adequate levels of both light and nutrients (Peeters et al., 1993; Jin et al., 2013). Mixing of the water column brings nutrients from deep in the water column to the surface layer and circulates phytoplankton through the light field, hence playing an important role in the growth cycle of phytoplankton (Bisset et al., 2001; Howarth et al., 2002). In shelf seas, there are further factors which can affect the phytoplankton growth, including the presence of suspended mineral particles and CDOM which modify the underwater light field (Vantrepotte et al., 2007) and stratification of

the water column which affects mixing (Peeters et al., 2013). The euphotic depth gives a measure of the depth of penetration of light in the water column. Hence studying the relationships between the euphotic depth, the diffuse attenuation coefficient and the distributions of different particle types is important for understanding the factors which affect the penetration of light, phytoplankton growth and primary production in shelf seas (Bisset et al., 2001; Capuzzo et al., 2013).

The previous two chapters demonstrated how, using remote sensing, the mean diffuse attenuation coefficient, the euphotic depth and the absorption coefficients of phytoplankton cells and mineral particles can be estimated for the Irish Sea. The methods developed relied on the assumption that the optical properties of the Irish Sea are driven by changes in the concentration of two particles classes, phytoplankton cells and mineral sediments, with a relatively invariant background level of CDOM. In this chapter, these methods are applied to satellite data to

1. Investigate the spatial and temporal variability of $\overline{K}_d(488)$, Z_{eu}, $a_{\mathrm{CHL}}(488)$ and $a_{\mathrm{MSS}}(488)$ over an 8 year period.

2. Determine how phytoplankton and mineral particles contribute to the attenuation of light in the water column.

3. Investigate the relationships between phytoplankton and mineral absorption and the euphotic depth.

6.1 Methods

The inversion procedure outlined in Figure 6.1 was carried out on all available MODIS observations from the Irish Sea spanning 2005 - 2012 (which were processed as described in Section 3.3).

The updated KdLee algorithm (Lee et al., 2013) was applied to the MODIS data as an intermediate step in the estimation of the euphotic depth. The simplified KdLee version (Lee et al., 2005b) was also considered, however, since it is a linear combination of $a(\lambda)$ and $b_b(\lambda)$,

$$\overline{K}_d(\lambda) = r_1 a(\lambda) + r_2 b_b(\lambda) \tag{6.1}$$

where r_1 is a function of the solar zenith angle, and r_2 is a constant. Use of Eq. (6.1) allows $\overline{K}_d(\lambda)$ to be partitioned into the contributions from the separate particle classes since, dropping the λ argument for brevity:

$$\begin{aligned}
\overline{K}_d &= r_1 a + r_2 b_b \\
&= r_1 \left(a_w + a_{\mathrm{CHL}} + a_{\mathrm{MSS}} + a_{\mathrm{CDOM}}\right) + r_2 \left(b_{bw} + b_{b\mathrm{CHL}} + b_{b\mathrm{MSS}}\right) \\
&= r_1 a_w + r_2 b_{bw} + r_1 a_{\mathrm{CHL}} + r_2 b_{b\mathrm{CHL}} + r_1 a_{\mathrm{MSS}} + r_2 b_{b\mathrm{MSS}} + r_1 a_{\mathrm{CDOM}} \\
&= \overline{K}_{d\mathrm{w}} + \overline{K}_{d\mathrm{CHL}} + \overline{K}_{d\mathrm{MSS}} + \overline{K}_{d\mathrm{CDOM}}.
\end{aligned} \tag{6.2}$$

The absorption coefficients of phytoplankton and mineral particles can be determined, along with an estimation of the CDOM absorption, using the partitioning procedure described in the previous Chapter. The backscattering coefficients of the two particle classes can then be estimated from the partitioned absorption coefficients and the backscattering to absorption ratios ($\rho_1,\ \rho_2$) which are derived

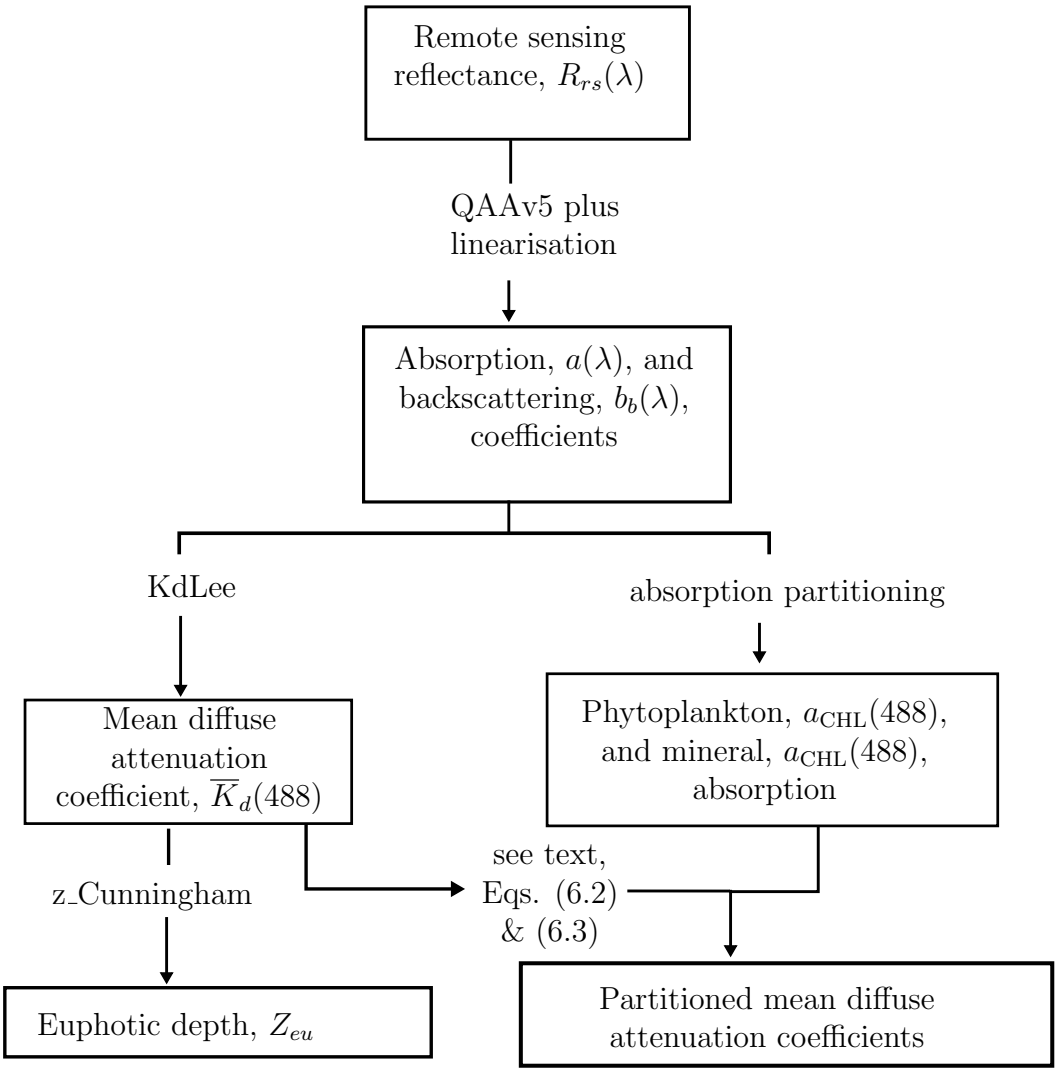

Figure 6.1: The inversion procedure applied to all available MODIS observations between 2005-2012.

as part of the partitioning method. Therefore, the fractional contribution of phytoplankton and mineral particles to the total mean diffuse attenuation coefficient at 488 nm can be determined,

$$\kappa_{\mathrm{CHL}} = \frac{\overline{K}_{d\mathrm{CHL}}}{\overline{K}_d} \qquad \text{and} \qquad \kappa_{\mathrm{MSS}} = \frac{\overline{K}_{d\mathrm{MSS}}}{\overline{K}_d}. \tag{6.3}$$

The euphotic depth can be estimated from $\overline{K}_d(488)$ using an empirically derived power law (Cunningham et al., 2013) (see Chapter 4). However, due to the non-linearity of this relationship, estimations of the individual contributions of phytoplankton and mineral particles to the euphotic depth are difficult. Hence the role each particle class plays on light attenuation was only considered in terms of $\overline{K}_d(488)$ and the variability in the euphotic depth was compared with seasonal variations of $a_{\mathrm{CHL}}(488)$ and $a_{\mathrm{MSS}}(488)$.

The temporal variability was studied at three contrasting locations within the Irish Sea shown in Figure 6.2: A is in shallower waters off the coast of Angelsey where there is strong tidal mixing and a patch of high turbidity (Bowers et al., 2002; Ellis et al., 2008), B is in the central region which remains well mixed throughout most of the year, and C is in the Celtic Sea, where the water column stratifies during the summer. Monthly composites and a transect from north to south across the whole region were used to examine the spatial variability. The data were both temporally and spatially averaged as described in Section 3.3.

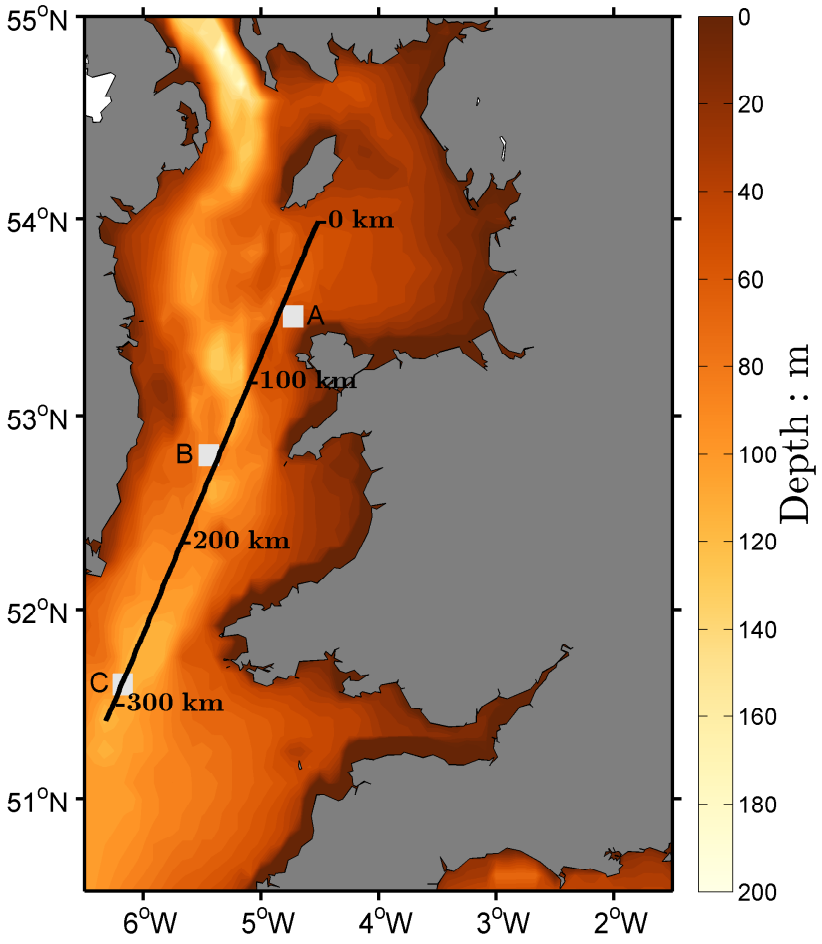

Figure 6.2: Bathymetry map of the Irish Sea and surrounding waters, with the 3 locations used for time series analysis and the transect considered for spatial variability indicated.

6.2 Application of Inversion Procedure to MODIS Data

Full Time Series for Three Contrasting Locations

The $a_{\mathrm{CHL}}(488)$, $a_{\mathrm{MSS}}(488)$, $\overline{K}_d(488)$, κ_{CHL}, κ_{MSS} and Z_{eu} data derived from the MODIS observations at each location are shown in Figures 6.3, 6.4 and 6.5, in which marked annual variability is visible for all three variables.

The general cycle of $a_{\mathrm{MSS}}(488)$ was similar at all three locations, peaking over the winter months and decreasing during the summer when mineral particles settle out of the surface layer. However, the amplitude and period of the annual cycle at each location was different. The $a_{\mathrm{MSS}}(488)$ values dropped earlier in the year at C, but by mid-summer $a_{\mathrm{MSS}}(488) < 0.05$ m^{-1} at all 3 locations. The highest values were observed at A, with a peak value of 0.29 m^{-1}, which was more than 5 times larger than the maximum value in the Celtic Sea at C (0.05 m^{-1}). At B, the amplitude was between that observed at A and C, with a maximum peak value of 0.16 m^{-1}.

The cycle of $a_{\mathrm{CHL}}(488)$ was similar at locations A and B, with the lowest observations during the winter months and a single peak occurring in the middle of the summer. Contrastingly, $a_{\mathrm{CHL}}(488)$ reached a maximum at C during the spring and often a smaller, secondary, peak was observed towards the end of the summer. The peaks of the phytoplankton cycles were significantly larger at C, with a maximum value of 0.5 m^{-1}, compared to B (0.13 m^{-1}) and A (0.25 m^{-1}).

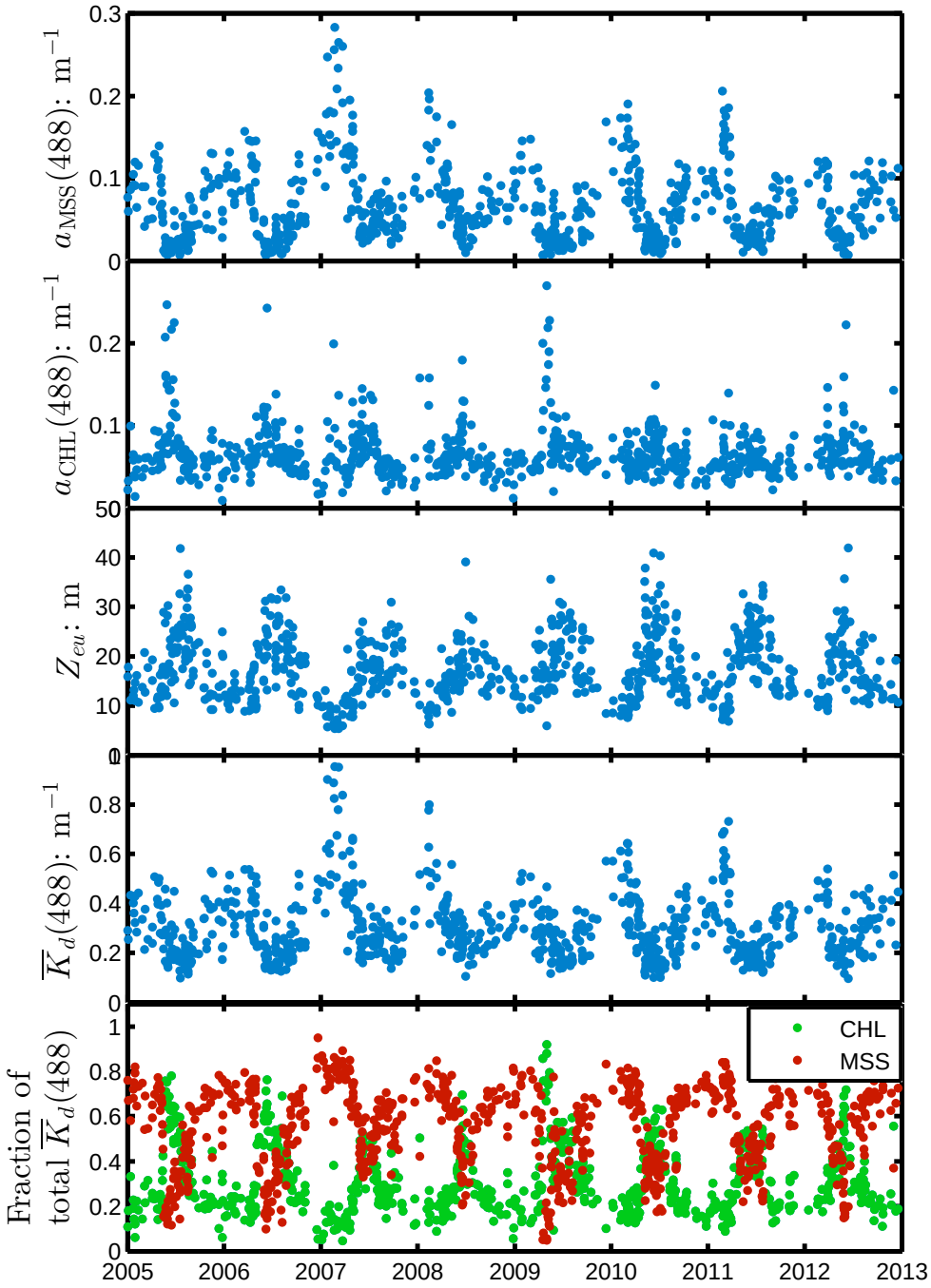

Figure 6.3: All the available MODIS observations at A during 2005 - 2012.

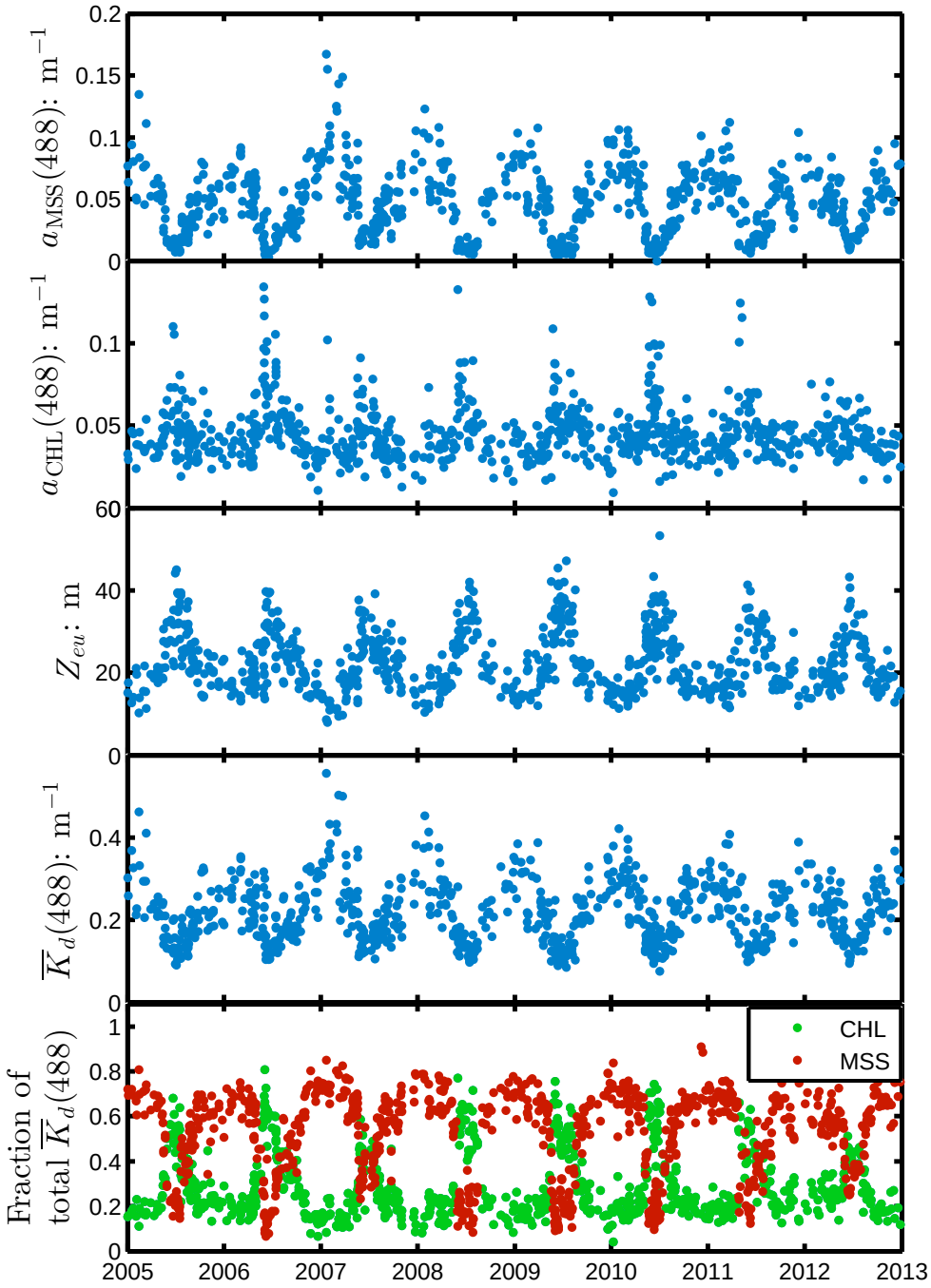

Figure 6.4: All the available MODIS observations at B during 2005 - 2012.

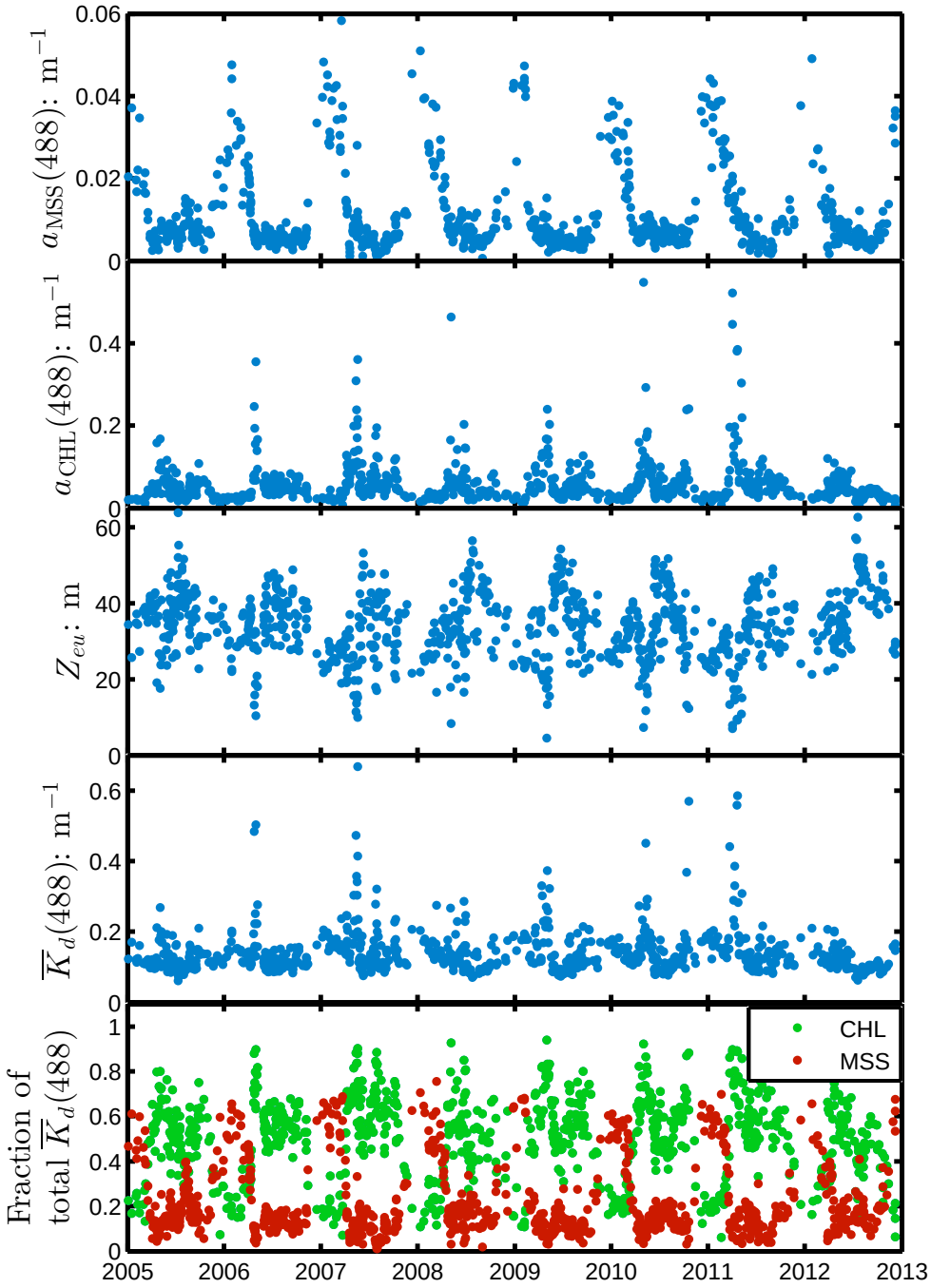

Figure 6.5: All the available MODIS observations at C during 2005 - 2012.

The timing and amplitude of the $a_{\mathrm{CHL}}(488)$ cycles appeared to vary more year on year compared to the $a_{\mathrm{MSS}}(488)$ cycles. This may be due to the irregular coverage provided by MODIS because of clouds, hence short-lived phytoplankton blooms may not be observed.

At location C, $\overline{K}_d(488)$ seemed to be correlated with $a_{\mathrm{CHL}}(488)$, peaking once in the spring and occasionally again in the autumn. Whereas, at A and B, $\overline{K}_d(488)$ was more correlated with $a_{\mathrm{MSS}}(488)$, reaching its maximum over the winter months and minimum in the summer. These correlations were reinforced by the fractional contributions of CHL and MSS to the total mean diffuse attenuation coefficient, κ_{CHL} and κ_{MSS} (see the bottom panel in Figures 6.3 - 6.5). At location C, for most of the year κ_{CHL} was larger than κ_{MSS} , which only dominated for a short period over the winter. In comparison, at A and B, the mineral particles were attenuating the most light for the majority of the year, with κ_{CHL} peaking above κ_{MSS} for a very short time over the summer.

The euphotic depths were generally lower in the winter and higher in the summer for all three locations. There was a fairly clear inverse relationship between $a_{\mathrm{MSS}}(488)$ and the euphotic depth at A and B, however this was less apparent at C. The range of euphotic depths was larger at C (5 - 60 m) compared to A (10 - 40 m) and B (10 - 45 m), but the minimum euphotic depth at C usually occurred during the spring, rather than the winter. By considering only one year of data, the relationships between $a_{\mathrm{CHL}}(488)$ and euphotic depth, particularly at location C, was seen more clearly (Figure 6.6).

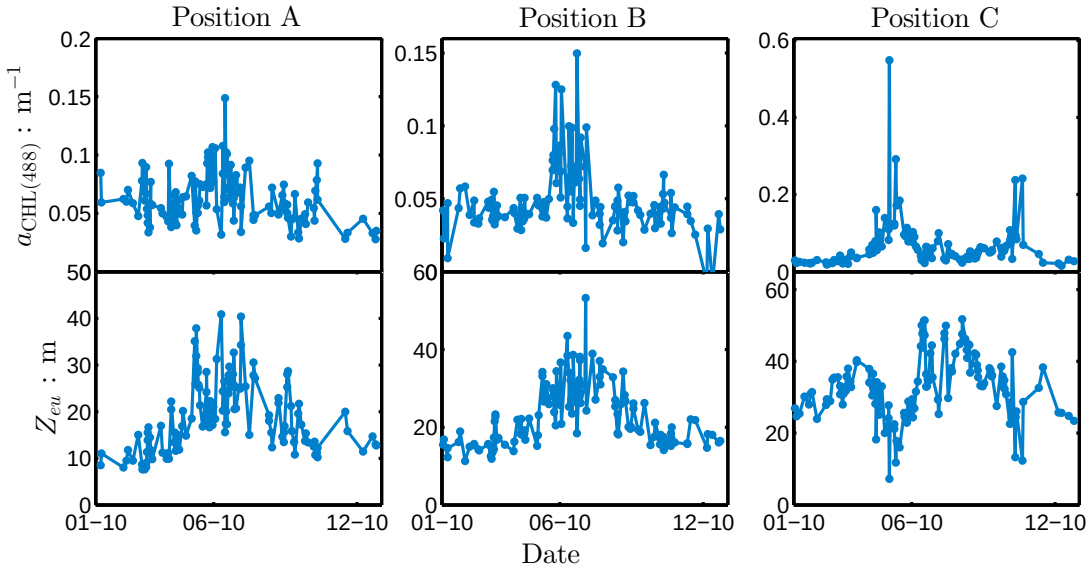

Figure 6.6: $a_{\mathrm{CHL}}(488)$ and euphotic depths at A, B and C during 2010.

Mean Annual Cycles at Three Contrasting Locations

Mean annual cycles for each variable were calculated at each location to emphasise any seasonality in the data.

Figure 6.7 shows the mean $a_{\mathrm{MSS}}(488)$ annual cycles. It was evident that the timing of mineral particles settling out of the surface layer was different at each location, with $a_{\mathrm{MSS}}(488)$ reaching its minimum summer value at C earlier than at A and B. Additionally, $a_{\mathrm{MSS}}(488)$ tended to stay at that minimum for a much longer duration at C, approximately 30 weeks, compared to at A and B where it remained at the minimum value for only 8 weeks.

The correlation between the $a_{\mathrm{MSS}}(488)$ and $\overline{K}_d(488)$ at A and B was evident from a comparison of the annual cycles (see Figures 6.7 and 6.8). At these two locations, both $a_{\mathrm{MSS}}(488)$ and $\overline{K}_d(488)$ were at a maximum over the winter months and a minimum during the summer. Whereas, at C, $\overline{K}_d(488)$ deviated from this general cycle. There were higher levels of $\overline{K}_d(488)$ over the winter

months compared to the summer, as observed at A and B, but the maximum $\overline{K}_d(488)$ values were observed during the spring and autumn while $a_{\mathrm{MSS}}(488)$ was low.

By considering the fractional contribution of CHL and MSS to total $\overline{K}_d(488)$ (Figure 6.9), it was evident that phytoplankton cells contribute over half of the $\overline{K}_d(488)$ term at C for most of the year, with mineral particles dominating briefly over the winter months. Contrastingly, MSS played the most significant role in the attenuation of light at 488 nm at A and B, apart from for a few weeks during mid-summer.

The phenology of the phytoplankton growth cycle at C was clearly shown in the mean annual cycle, with two pronounced peaks in the spring and autumn (Figure 6.10). At A and B the cycle was not so pronounced, but small mid-summer peaks in $a_{\mathrm{CHL}}(488)$ were present. The reduction in amplitude of the mean annual cycles at all three locations compared to the full time series may be due to the fact that the mean cycles were determined using a two week interval, while phytoplankton growth does not always happen at the exact same time every year. Hence if the bloom occurs within a different fortnight from one year to the next, the maximum value will be spread out.

The mean annual cycles of the euphotic depths are shown in Figure 6.10. There were sharp reductions in Z_{eu} at C coinciding with the peaks in phytoplankton absorption, but these were not visible at A and B (Figure 6.10). The seasonality in Z_{eu} at A and B was similar, with low winter values gradually increasing to a maximum during the summer, before decreasing back to the winter minimum.

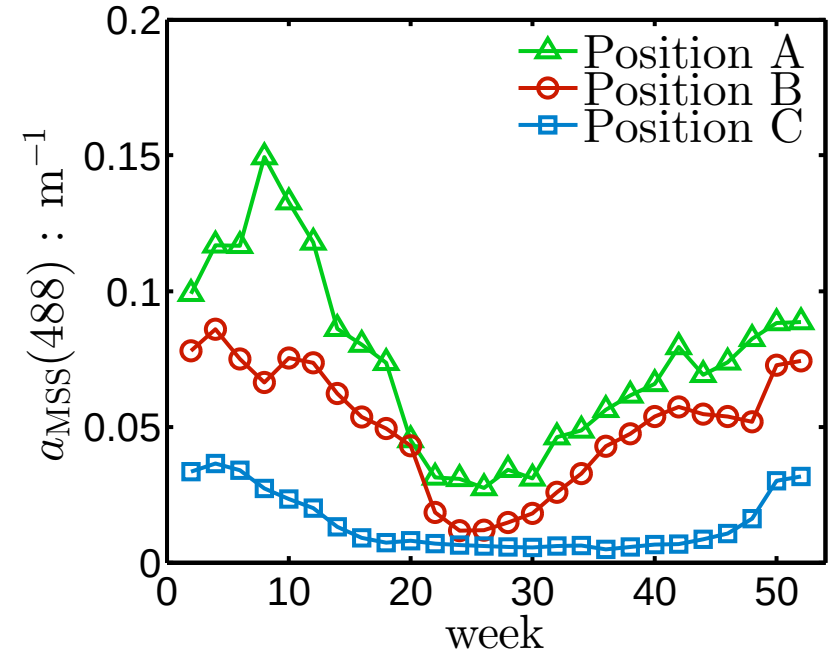

Figure 6.7: Mean annual cycles of $a_{\mathrm{MSS}}(488)$ at A, B and C.

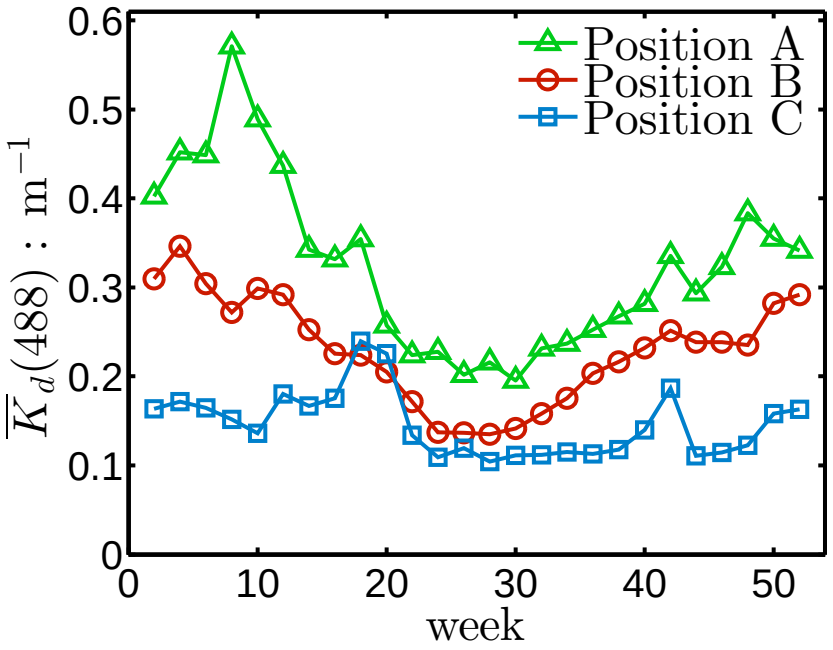

Figure 6.8: Mean annual cycles of $\overline{K}_d(488)$ at A, B and C.

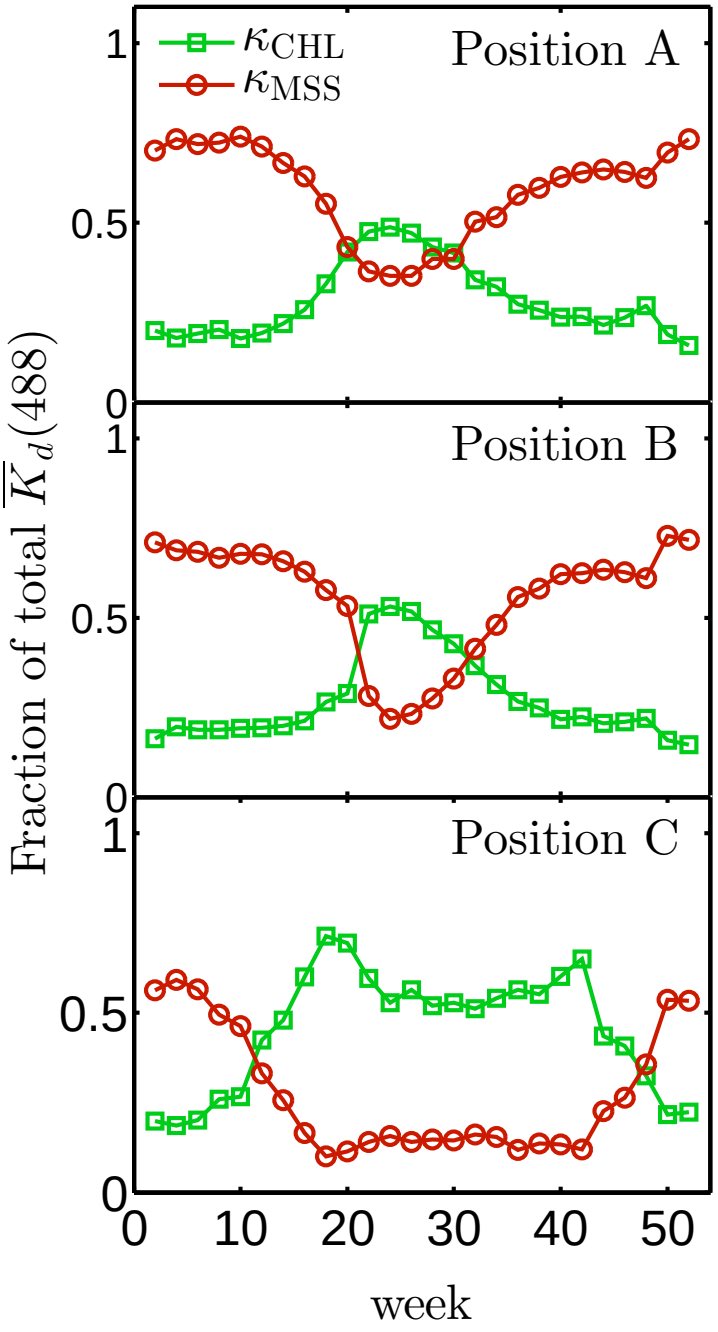

Figure 6.9: Mean annual cycles of κ_{CHL} and κ_{MSS} at A, B and C.

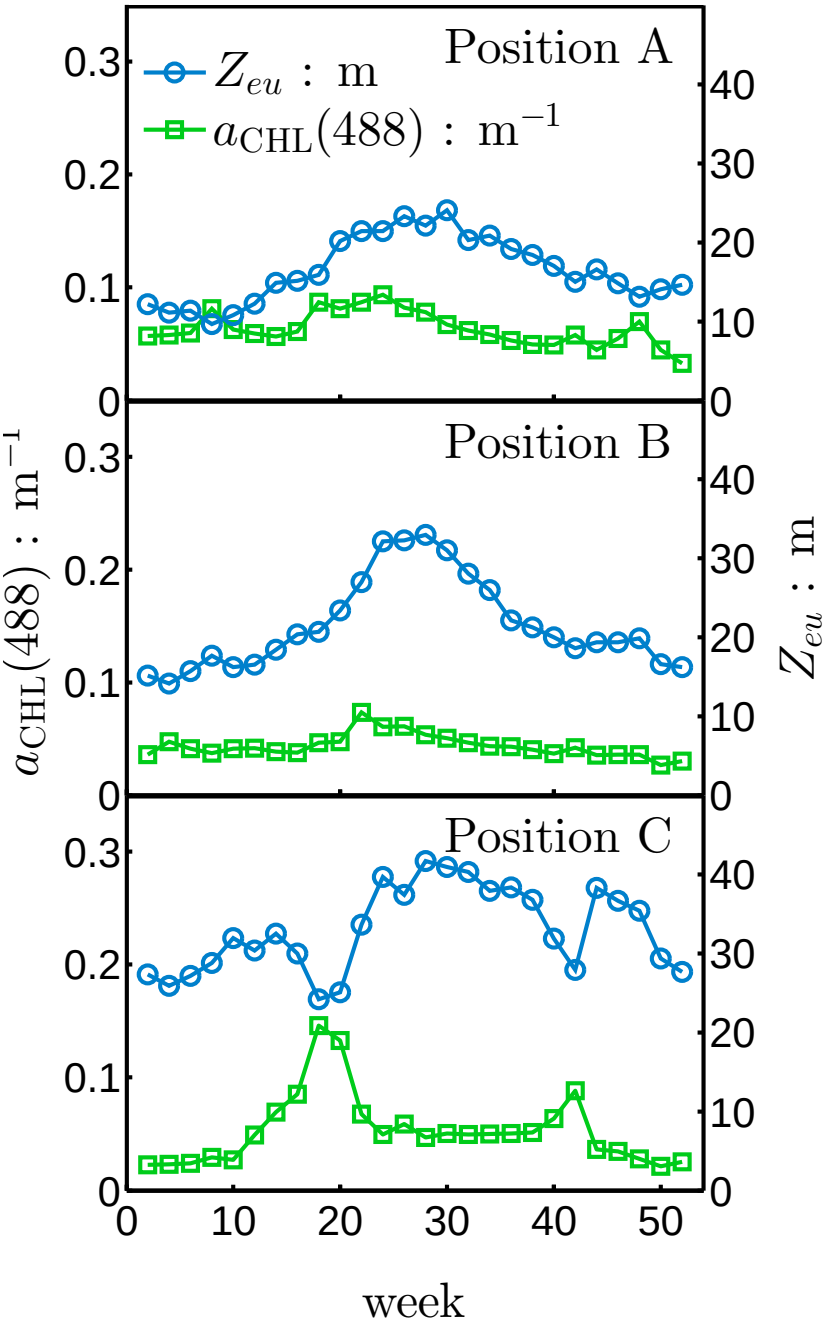

Figure 6.10: Mean annual cycles of $a_{\mathrm{CHL}}(488)$ and Z_{eu} at A, B and C.

Monthly Composite Maps of Remotely Sensed Optical Properties for the Irish Sea

Monthly averages for Z_{eu}, $a_{\mathrm{MSS}}(488)$, $a_{\mathrm{CHL}}(488)$, $\overline{K}_d(488)$, κ_{MSS} and κ_{MSS} were determined and mapped for January, April, July and October (Figures 6.11 - 6.16).

Figure 6.11 shows that the distribution of mineral absorption was broadly related to the bathymetry, with higher values along the coasts and in the estuaries and lower values in the deep central trough. Mineral absorption was highest during the winter, and lowest in the summer across the whole region, with the minimum occurring in the Celtic Sea during July.

The phytoplankton absorption maps are should be interpreted with care (Figure 6.12). The absorption partitioning procedure is sensitive to variable CDOM concentrations (see Figure 5.5). Bowers et al. (2013) mapped CDOM concentrations in the Irish Sea, demonstrating along the coastal regions that the CDOM concentration is likely to exceed 0.2 m^{-1}. Therefore the $a_{\mathrm{CHL}}(488)$ values recovered by the absorption partitioning procedure in these areas may be unreliable. Furthermore, in the time series plots the periods of phytoplankton growth were seen to be short-lived, and the large peak values of $a_{\mathrm{CHL}}(488)$ were lost in the monthly averaging process. However, a general pattern of phytoplankton growth was still seen. An increase of $a_{\mathrm{CHL}}(488)$ was observed during April in the stratified regions to the south and north. By July, there were elevated levels of $a_{\mathrm{CHL}}(488)$ across the whole region, except in the south, where $a_{\mathrm{CHL}}(488)$ had fallen from the peak observed during the spring. In October, $a_{\mathrm{CHL}}(488)$ had risen in the south again, whereas it had begun to fall across the rest of the region, back to the winter minimum.

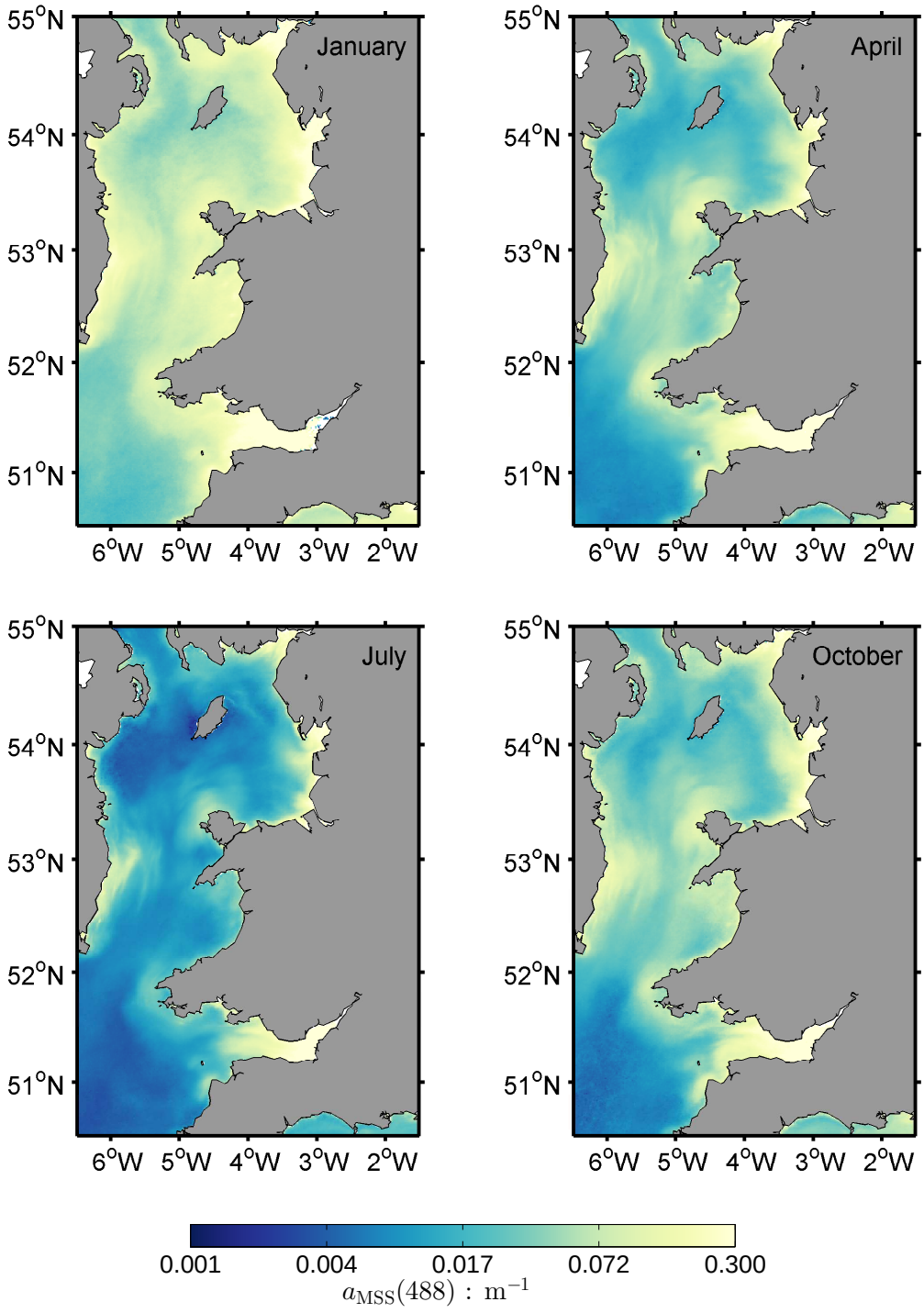

Figure 6.11: Monthly composites of $a_{\mathrm{MSS}}(488)$ calculated for four months during 2005-2012.

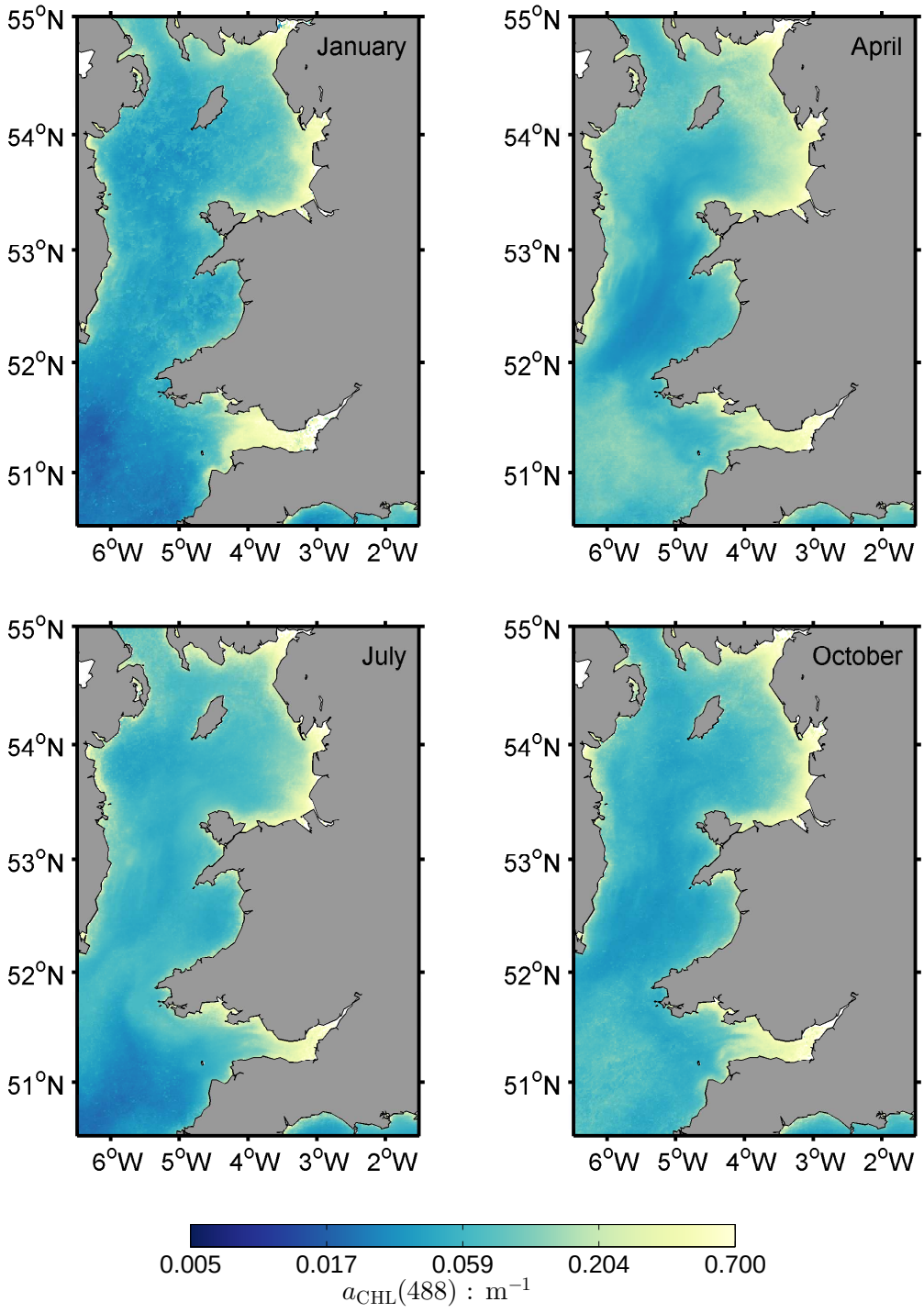

Figure 6.12: Monthly composites of $a_{\mathrm{CHL}}(488)$ calculated for four months during 2005-2012.

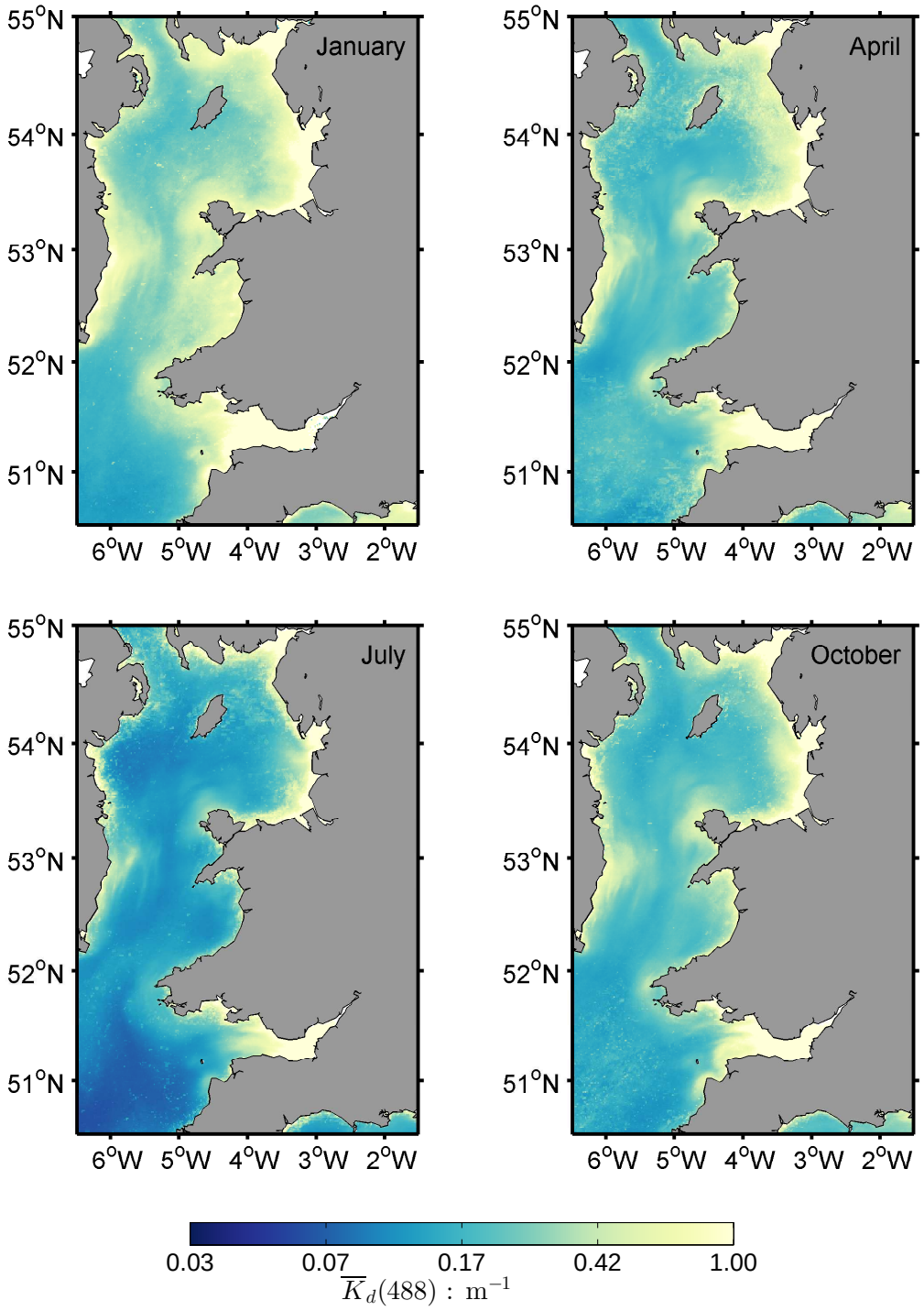

Figure 6.13: Monthly composites of $\overline{K}_d(488)$ calculated for four months during 2005-2012.

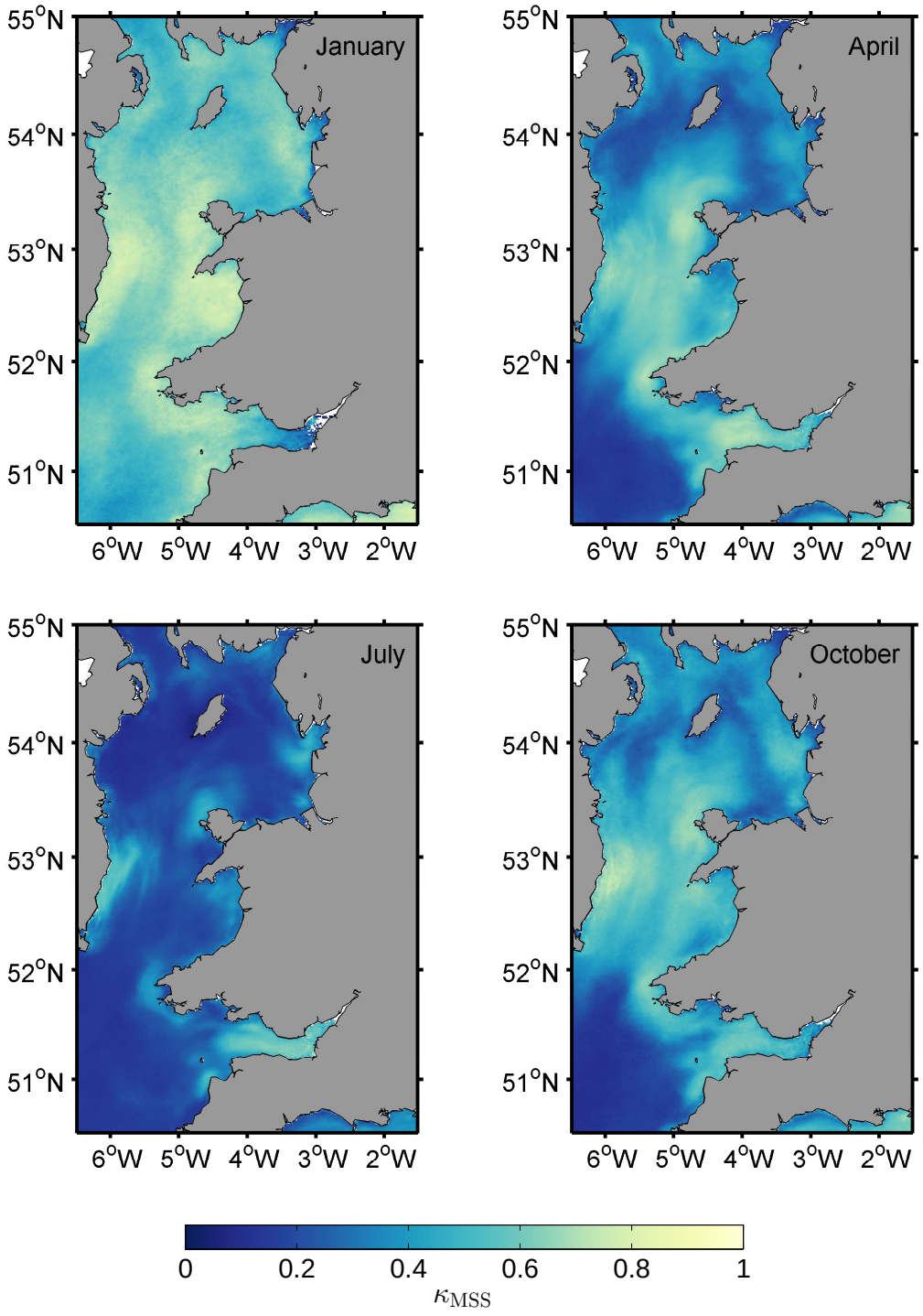

Figure 6.14: Monthly composites of κ_{MSS} calculated for four months during 2005-2012.

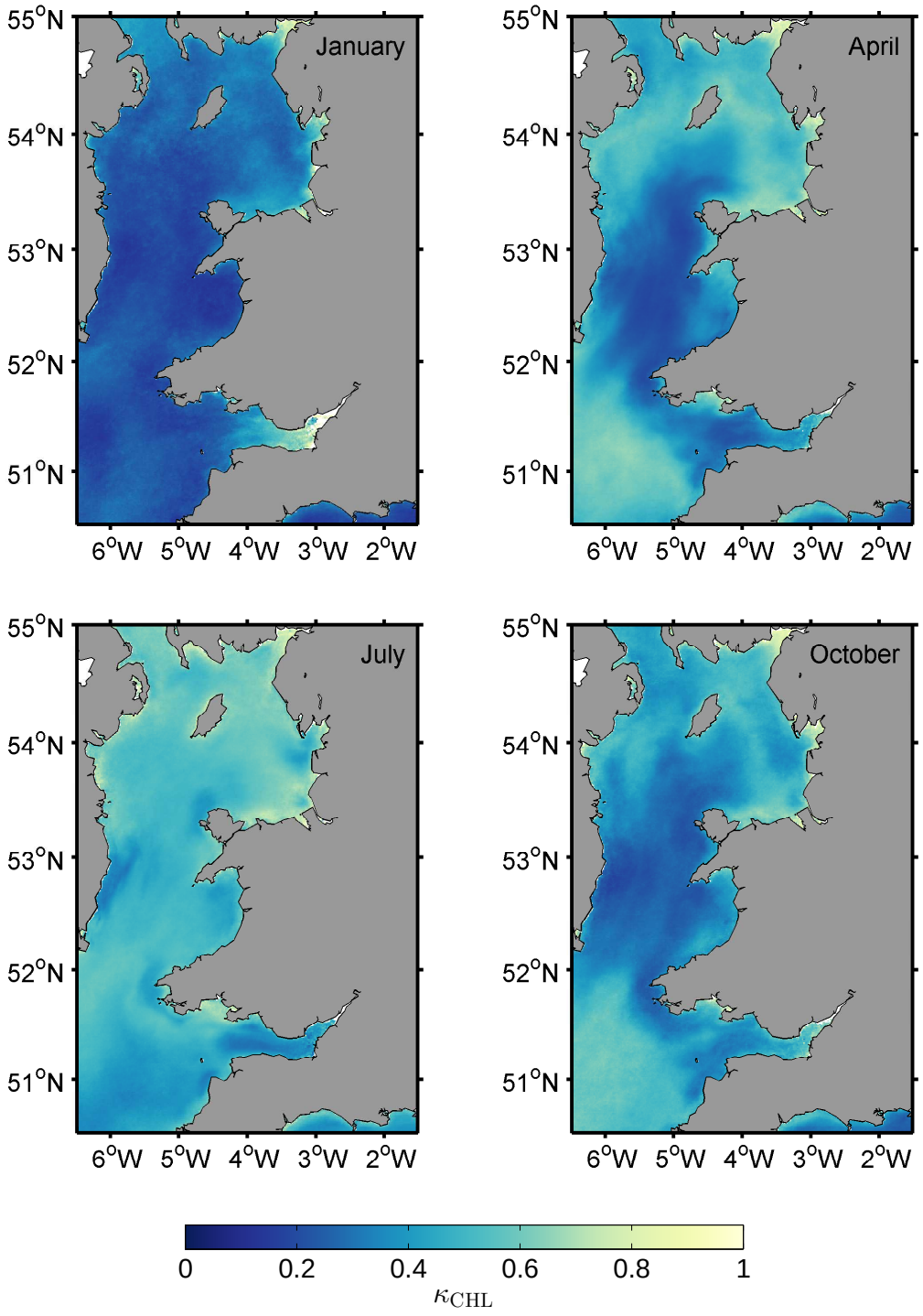

Figure 6.15: Monthly composites of κ_{CHL} calculated for four months during 2005-2012.

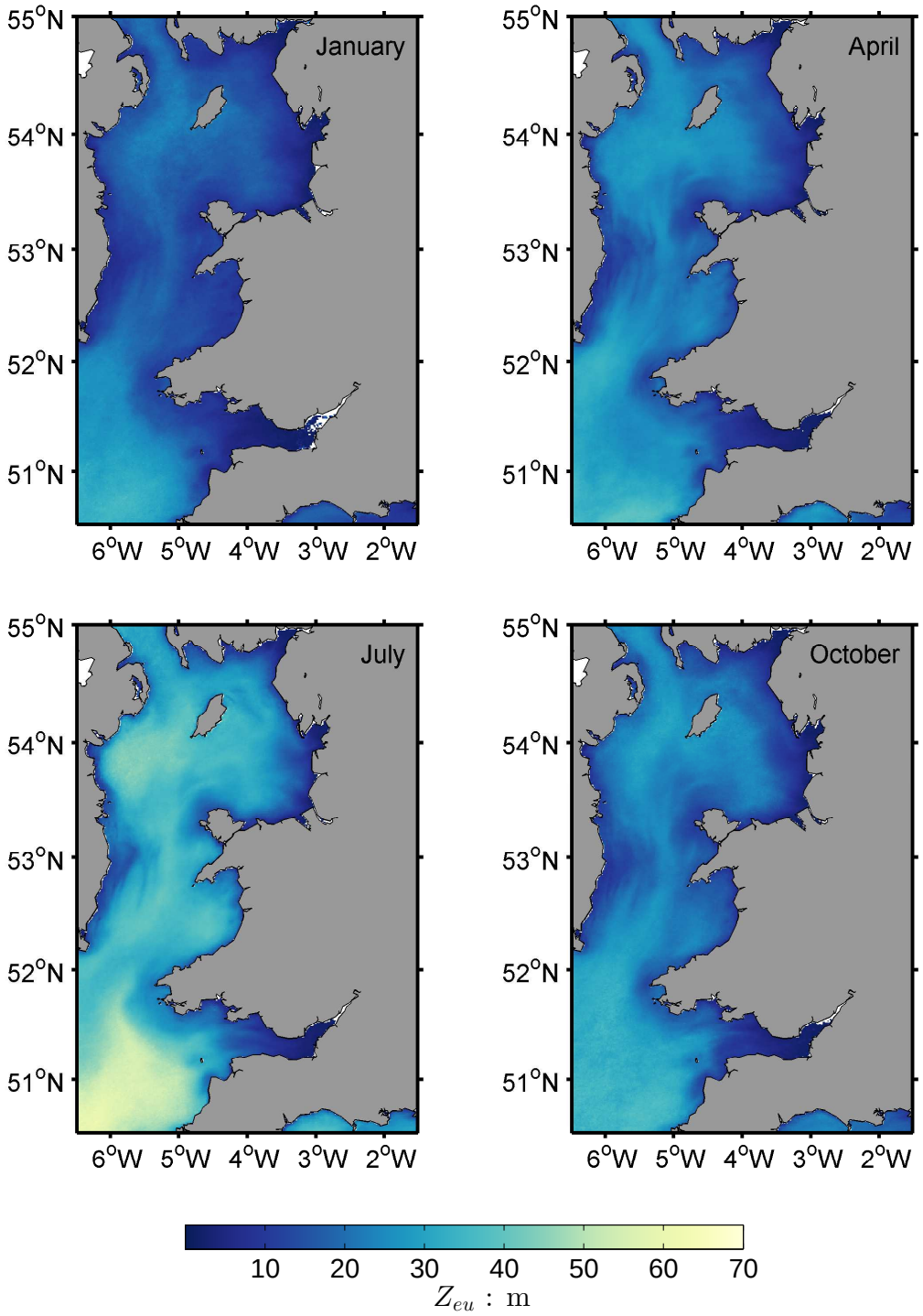

Figure 6.16: Monthly composites of Z_{eu} calculated for four months during 2005-2012.

Features from both the phytoplankton and mineral absorption maps were visible in the mean diffuse attenuation coefficient maps (Figure 6.13). There were raised levels of $\overline{K}_d(488)$ during the winter which decreased over the summer, with the highest values along the coast and in the estuaries, similar to the mineral absorption coefficient. However, in the regions which stratify in the north and south, $\overline{K}_d(488)$ is consistent with the patterns observed for $a_{\mathrm{CHL}}(488)$, with higher values in the spring and autumn compared to mid-summer. The relationship between $\overline{K}_d(488)$ and the absorption due to each particle class was emphasised in the maps of κ_{CHL} and κ_{MSS} (Figures 6.14 and 6.15). In January, $\kappa_{\mathrm{MSS}} \geq 0.5$, therefore mineral particles are contributing the most to the total mean diffuse attenuation coefficient across the whole region. The apparently large fractional contribution of phytoplankton cells to $\overline{K}_d(488)$ in the estuaries is probably an artefact, due to either the degrading effect of CDOM on the absorption partitioning procedure (see Figure 5.5) or to levels of suspended sediments larger than those considered in the development of the procedure. In the spring and autumn, mineral particles remained the main attenuators in the central mixed region, whereas to the stratified north and south phytoplankton cells were contributing most of the attenuation. During the summer, phytoplankton were attenuating the majority of the light across the whole region, with $\kappa_{\mathrm{CHL}} \geq 0.5$, apart from in the regions which were identified as turbidity maxima (Bowers et al., 2002; Ellis et al., 2008).

The euphotic depths in the monthly averaged maps seemed to be inversely correlated with the mineral absorption coefficient (see Figures 6.11 and 6.16), with the highest values in the central trough and Celtic Sea, and lowest values occurring in coastal waters throughout the year. The euphotic zone deepened over the spring and summer, reaching a maximum depth in July in the south-east. It should be noted that the periods of sharp reductions in Z_{eu} during phytoplankton

blooms were not visible in the monthly averaged maps.

6.3 Spatial Variability of κ_{CHL} and κ_{MSS} and Their Potential as an Indicator of Tidal Fronts

The spring and autumn monthly average maps of κ_{CHL} and κ_{MSS} showed distinct boundaries between the two contrasting regimes of fully mixed water where mineral particles dominated the attenuation of light and the stratified waters where phytoplankton cells dominated the attenuation. The boundaries between these regions are marked by fronts (Simpson and Hunter, 1974; Simpson and Bowers, 1981), hence the fractional contribution of CHL and MSS to the mean diffuse attenuation coefficient may act as a useful indicator to the frontal positions.

In Figure 6.17, κ_{CHL} and κ_{MSS} are compared with SST and $R_{rs}(667)$ along the transect shown in Figure 6.2, for two clear days in the spring and autumn. Simpson and Hunter (1974) observed a sharp discontinuity in SST across the fronts in the Irish Sea during the early summer, and Neil et al. (2012) demonstrated there was a sharp change in $R_{rs}(667)$ either side of the front in St George's Channel during the spring and autumn, with the waters being warmer and less reflective in the stratified region. These steps in SST and $R_{rs}(667)$ are visible in both the spring and autumn remote sensing transects, indicating the position of the front on those days. Additionally, there is a decrease in SST (and a corresponding increase in $R_{rs}(667)$) at the start of the spring transect, although this change occurs over a larger distance, perhaps suggesting a weaker front. The steps in SST and $R_{rs}(667)$ are coincident with a sharp change in the particle class which

is attenuating the most light. In the fully mixed waters, κ_{MSS} was larger than κ_{CHL}, but crossing the front the roles were reversed. The change in SST across the front was rapid, but relatively small in magnitude (~ 1.5°C) and the change in $R_{rs}(667)$ was relatively large (~ 0.0015 sr^{-1}) but happens over a longer distance, whereas the change κ_{MSS} and κ_{CHL} was both rapid and relatively large (~ 0.4 for both variables). Therefore, the fractional contribution of phytoplankton cells and mineral particles to the total mean diffuse attenuation coefficient could be used in the identification of the two contrasting regimes and possibly the position of the fronts in the Irish Sea.

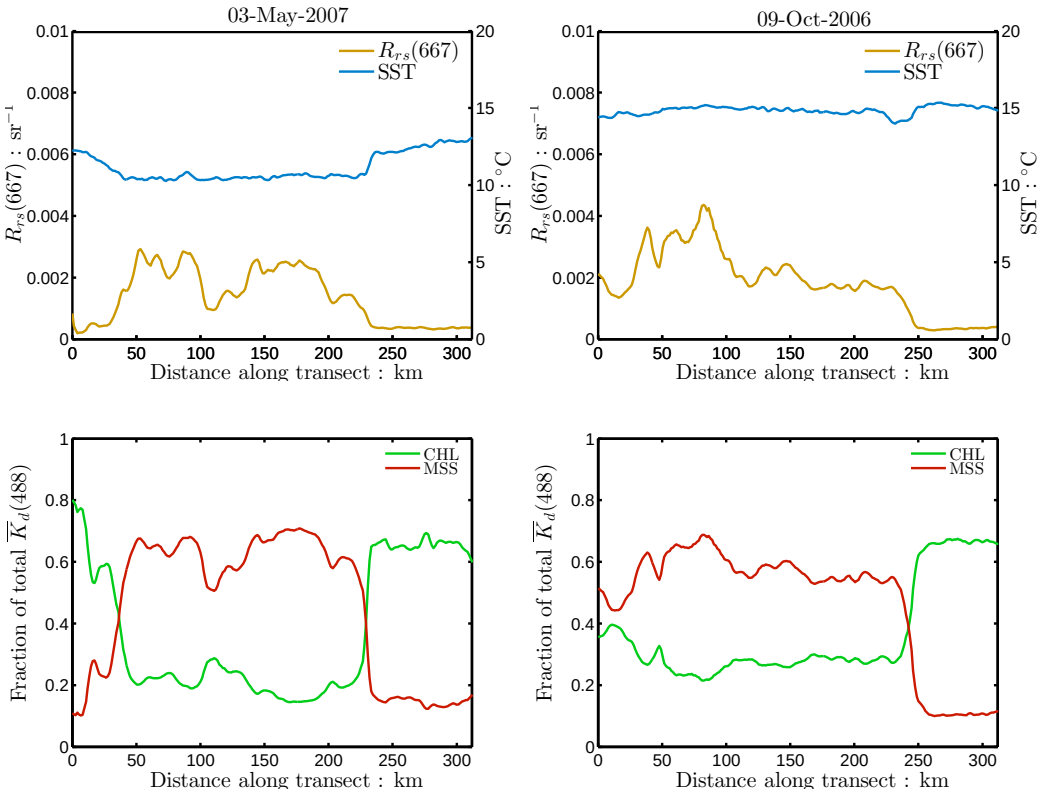

Figure 6.17: κ_{CHL}, κ_{MSS}, SST and $R_{rs}(667)$ along the transect shown in Figure 6.2, starting in the north, for 03-May-2007 (left hand side graphs) and 09-Oct-2006 (right hand side graphs).

6.4 Discussion

Three aims were outlined at the beginning of this Chapter, each of which is discussed individually:

1. *Investigate the spatial and temporal variability of* $\overline{K}_d(488)$*,* Z_{eu}*,* $a_{\mathrm{CHL}}(488)$ *and* $a_{\mathrm{MSS}}(488)$ *over an 8 year period.*

   By considering all the available MODIS observations for three contrasting sites within the Irish Sea, the temporal variability in $\overline{K}_d(488)$, Z_{eu}, $a_{\mathrm{CHL}}(488)$ and $a_{\mathrm{MSS}}(488)$ was examined, and mean annual cycles were calculated to emphasise the seasonality of each parameter. There was marked seasonality in all the parameters, but this differed by location. Generally, $\overline{K}_d(488)$ and $a_{\mathrm{MSS}}(488)$ peaked over the winter months, and were at a minimum during the summer, with Z_{eu} and $a_{\mathrm{CHL}}(488)$ following the inverse of this cycle. In the southern stratified region, however, $a_{\mathrm{CHL}}(488)$ peaked during the spring and autumn, with a coincident increase in $\overline{K}_d(488)$ and decrease in Z_{eu}.

   The spatial variability was examined by determining monthly composites of the whole region for four months, which were selected to capture the different seasons. These emphasised the patterns seen in the time series data, showing that the seasonality of $a_{\mathrm{CHL}}(488)$, Z_{eu} and $\overline{K}_d(488)$ in all stratified regions was similar to that observed at the southern location in the Celtic Sea. Additionally, the annual cycle of minimum $a_{\mathrm{CHL}}(488)$ and Z_{eu} in the winter with maximum values in the summer was observed in all the regions which stay fully mixed throughout the year.

2. *Determine how phytoplankton and mineral particles contribute to the attenuation of light in the water column.*

   The contrasting dynamical behaviour of phytoplankton and mineral particles contributes to complex spatial and temporal variations in the depth of penetration of solar radiation across the region. By considering the fractional contribution of MSS and CHL to the mean diffuse attenuation coefficient, the role of each particle class in determining the optical properties of the water column and the attenuation of light becomes clearer. In the central region which stays fully mixed throughout the year, mineral particles dominate light attenuation, apart from a brief spell during the summer. Whereas, in the stratified regions, phytoplankton cells are the primary attenuators from the spring through to the autumn. Maps of κ_{CHL} and κ_{MSS} were correlated with the two different mixing systems, with distinct boundaries coinciding with front positions, suggesting these parameters can provide an insight into how the physical mixing processes can be linked to the role each particle class plays in light attenuation.

3. *Investigate the relationships between phytoplankton and mineral absorption and euphotic depth.*

   From the MODIS observations it can be seen that mineral particles play a major role in the attenuation of light in the water column, consequently affecting the euphotic depth across the whole region throughout the year. In the Irish Sea wind and tides drive mixing of the water column, with increased mixing bringing mineral particles into the surface layer (Bowers, 2003; Neil et al., 2012). Therefore, the absorption due to mineral particles can give insights into both the euphotic depth and vertical mixing.

The time series data revealed differences in the relationship between the euphotic depth and the absorption of phytoplankton cells in fully mixed and seasonally stratified regimes. During periods of rapid phytoplankton growth, light attenuation was significantly altered, reducing the depth which light was available for photosynthesis. This was evident at location C (in the seasonally stratified system) during the spring and autumn phytoplankton blooms. Additionally at C, (1) $a_{\mathrm{CHL}}(488)$ was low when the euphotic zone was at its maximum depth in the middle of the summer, and (2) $a_{\mathrm{MSS}}(488)$ fell from its winter maximum in the early spring, remaining at a low level until the late autumn. These two observations suggest that at the start of the year whilst mineral particles were still present in the surface layer, phytoplankton growth in the southern Irish Sea was limited by light availability, however by mid-summer a factor other than light is limiting growth, potentially a depletion of nutrients after the spring bloom. On the other hand, in the fully mixed regime (A and B), mineral particles only drop out of the surface layer for a short period during the middle of the year. The phytoplankton absorption and euphotic depth both peak in mid-summer, suggesting light availability was inhibiting phytoplankton growth until later in the year than at C. This is consistent with the observations of Gowen et al. (1995).

7. Conclusions

This project has focussed on the remote sensing of optical properties in optically complex waters, applying the methods which have been developed to an archive of satellite data for the Irish Sea in order to interpret the variability in ocean colour found in shelf seas.

Initially, a bio-optical model of the Irish Sea was created using locally determined SIOPs and concentrations of optically significant materials that were typically observed in the region. The synthetic datasets produced were used in the evaluation of the quasi-analytical algorithm of Lee et al. (2002, 2009), which recovers both the absorption and backscattering coefficients from the remote sensing reflectance. The two most recent versions of the algorithm were tested, QAAv5 and QAAv6. These algorithms follow the same basic structure, but QAAv6 includes a switch in the reference wavelength to 667 nm for higher absorbing waters. Both versions required only slight adjustments for use in the Irish Sea: for QAAv5 a linearisation step was applied to the recovered absorption coefficients, while for the QAAv6 the coefficients of algorithm were optimised. These tuned algorithms were applied to field data gathered across the region. QAAv5 with linearisation provided the best performance, with gradients close to 1 and coefficients of determination above 0.8 for all wavelengths between 443 nm and 555 nm, hence this version of the algorithm was used for all further analysis.

The method of Lee et al. (2005b) for recovering the mean diffuse attenuation coefficient from the absorption and backscattering coefficients was evaluated on the field data. For this purpose, the absorption and backscattering coefficients

recovered from the QAAv5 with linearisation were used as inputs to three different versions of the Lee algorithm (2005b; 2013). All three algorithms performed similarly across all wavelengths, with the best recoveries between 443 nm and 555 nm, indicating that any of the algorithms could be used without much loss in accuracy.

Finally, three different euphotic depth algorithms, which use either the absorption and backscattering coefficients or the mean diffuse attenuation coefficient at 488 nm as inputs, were tested on the field data. The QAAv5 with linearisation was used as a starting point to initially recover the absorption and backscattering coefficients, and the mean diffuse attenuation coefficient was recovered using the most recent version of the KdLee algorithm (Lee et al., 2013). All the algorithms recovered euphotic depths which were well correlated with the field data, with the algorithm of Cunningham et al. (2013) returning a gradient closest to unity. Therefore this algorithm was used in subsequent chapters.

In Chapter 5, a method was developed to partition the total absorption coefficient into the phytoplankton and mineral components for regimes where phytoplankton and mineral particles are the main drivers of the optical properties, with a relatively low constant influence from CDOM. The method requires only four parameters, the total particulate absorption and backscattering coefficients, and the backscattering to absorption ratios for both phytoplankton and mineral particles. The QAA can be used to determine the total absorption and backscattering coefficients, then from a plot of the non-water absorption against particulate backscattering, the CDOM absorption and backscattering to absorption ratios for phytoplankton and mineral particles can be estimated. The partitioning method was evaluated on the Irish Sea modelled data with recovered phytoplankton and mineral absorption coefficients highly correlated with modelled values, with co-

efficients of determination of 0.94 and 0.97 respectively. The sensitivity of the method to variable CDOM absorption was evaluated, with the recovery of the phytoplankton absorption coefficient rapidly degrading. However, for the Irish Sea, the estimated root mean square errors were 0.009 m^{-1} for $a_{MSS}(488)$ and 0.02 m^{-1} for $a_{CHL}(488)$.

The backscattering and absorption coefficients for eight years of MODIS data covering the Irish Sea and surrounding waters were determined from the remote sensing reflectance using the QAAv5 with linearisation. Plots of the non-water absorption against particulate backscattering coefficients for two-week intervals showed the changes in particle types present in the surface layer of the water column. The absorption partitioning procedure was then applied to a patch in the eastern Irish Sea, showing the dominance of mineral particle absorption during the winter months and the absorption of phytoplankton particles over the summer.

In Chapter 6, the phytoplankton and mineral absorption coefficients, the mean diffuse attenuation coefficients and the euphotic depths were determined from the MODIS data for the Irish Sea. A method for partitioning the mean diffuse attenuation coefficient into phytoplankton and mineral parts was developed. Three contrasting locations were selected to investigate the temporal variability of the parameters and monthly composite maps were generated to show the spatial variability across the whole region. From the partitioned absorption coefficients it was seen that in the stratified waters phytoplankton growth occurred early in the year, often with a second peak in the autumn, but was at a minimum during the summer when the euphotic depth was at its maximum. Whereas in the regions which stay fully mixed throughout the year, the phytoplankton growth occurred later in the year, peaking in mid-summer. Initially, both the spatial and tempo-

ral variability of the mean diffuse attenuation coefficient looks complex, but by considering the fractional contribution of mineral and phytoplankton particles to the total mean diffuse attenuation coefficient, it becomes clearer how the attenuation due to the two different particles contribute to light attenuation in the water column. Additionally, the spatial variability of the fractional contributions suggests these parameters could be used as an indicator to distinguish between the two distinct mixing regimes.

Four main aims were stated in Chapter 1, each of which can now be addressed.

1. *Can ocean colour remote sensing be used in Case-2 shelf seas to quantitatively measure the optical properties of the water column?*

   The semi-analytical methods of Lee et al. (2002, 2005b, 2007, 2009, 2013) for deriving absorption, backscattering and depth-averaged diffuse attenuation coefficients and the empirical relationships of Cunningham et al. (2013) and Zhao et al. (2013) for the euphotic depth required little or no adjustments to recover all the parameters within the Irish Sea and surrounding waters. The adjusted QAA recovered the inherent optical properties with percentage errors similar to those reported by Lee et al. (2002) for the original QAA: $a(440)$ and $b_b(555)$ were recovered with mean percentage errors of (i) 14% and 19% respectively by Lee et al. (2002), (ii) 12% and 11% for the Irish Sea field data using QAAv5 with linearisation and (iii) 14% and 12% for the Irish Sea field data using the optimised QAAv6. Lee et al. (2005a) tested the KdLee algorithm on the oceanic and coastal waters of the Gulf of Mexico, the Arabian Sea and the Baltic Sea, recovering $\overline{K}_d(490)$ with an average percentage difference of 14%. The three versions of the KdLee

algorithm tested retrieved the mean diffuse attenuation coefficients at 490 nm to within a few percent of this value, with values of 12% for the original and updated algorthims, and 14% for the simplified version. The empirically derived euphotic depths and those derived using the semi-analytical method of Lee et al. (2007) were recovered for the Irish Sea field data with average percentage errors of 14% - 20%, which are comparable to the 14% found by Lee et al. (2007) for Monterey Bay, the Gulf of Mexico and the Arabian Sea. The recoveries for the field data were not as accurate as for the modelled data, but may partly be due to the difficulties in achieving closure between the field IOP and radiometry measurements. Similar difficulties were reported for the NOMAD dataset by Werdell et al. (2013), and for Mie modelling by Chang and Whitmire (2009).

2. *Can remote sensing be used to identify different particle classes?*

   The recovery of particle concentrations from ocean colour data still poses a major challenge in optically complex waters, with most algorithms based on empirical regressions. An alternative approach is to consider the contributions of different particle classes to inherent optical properties, in particular, the absorption coefficients for phytoplankton and mineral particles. By simplifying the problem to consider shelf seas where CDOM has a relatively constant background influence on the optical properties of the water column, a method was developed to recover these absorption coefficients from ocean colour data. On application to MODIS data, this method was seen to effectively separate the contribution of the two particle types. This separation of phytoplankton and mineral particle absorption is important in shelf seas where mineral particles affect the performance of chlorophyll-a algo-

rithms so that reported phytoplankton concentrations are frequently higher than are actually present. Additionally, the recovery of the phytoplankton absorption coefficient is particularly useful for shelf sea primary production estimations.

3. *Can the role of different types of particle on the attenuation of light in the water column be determined from ocean colour?*

   The mean diffuse attenuation coefficient can be estimated from the inherent optical properties of the water column. Therefore, by combining the method for recovering the absorption and backscattering coefficients with the absorption partitioning technique, the contribution to the total depth-averaged diffuse attenuation coefficient for each particle class can be determined. The fractional contribution of phytoplankton and mineral particles to the total mean diffuse attenuation coefficient is then a useful indicator of the role each particle plays in altering the depth of penetration of solar radiation, which is important for understanding the factors affecting both phytoplankton growth in shelf seas and heat transfer in the upper layer of the water column. Additionally, the fractional contributions provide an insight into which particles are driving the optical properties of the water column, potentially indicating different mixing dynamics and front positions across a region. During the summer, fronts are areas of enhanced primary production which influence the distribution of ichthyoplankton and zooplankton, potentially creating foraging sites for larger marine mammals. Additionally, frontal systems may have a significant role in determining circulation in shelf seas, therefore detection of fronts is important for further studies of these systems.

4. *Can ocean colour data be used to determine the temporal and spatial variability of optical properties in shelf seas, providing insights into the underlying physical dynamics of the region?*

   An archive of satellite data offers great potential for investigating the variability in ocean colour across shelf seas. In a region with a high incidence of cloud cover, analysis of a time series of ocean colour data is often more useful than studying single images. In this study, eight years of satellite data for the Irish Sea revealed spatial and temporal patterns in ocean colour which could be linked to changes in the optical properties of the water column. By considering temporal and spatial averages of the optical properties and subsequent parameters, the gaps in coverage due to clouds were minimised and clear annual cycles in all the parameters were observed. The accurate recovery of the optical properties of the water column and the identification of particle class in shelf seas can potentially provide benefits to a wide range of sectors. These include

   i) Data for Modelling Studies - Many areas of oceanography rely on modelling, including ecosystem and hydrodynamical modelling, to understand complex system dynamics and predict how they will change due to external impacts. The models need observations for validation and assimilation, and ocean colour can provide almost daily data for most of the world's oceans.

   ii) Monitoring Transient Events - Many transient events alter the colour of the water, such as sediment plumes resulting from stormy conditions and harmful algal blooms. Ocean colour data can be used to monitor these changes and track the progress of these events. Cur-

rently, the polar orbiting ocean-colour sensors don't provide the high temporal coverage and high spatial resolution required to track fast moving, fine scale events, but they can provide information on larger-scale events which are present for more than one day. Development of new sensors and remotely piloted aircrafts is showing the potential these new systems could have for monitoring hazards, particularly near to the coast.

iii) Water Quality - The pressures put on marine systems by human activities and changing climates may alter water quality. A set of water-quality indicators have been identified, including turbidity, biomass concentration, total suspended matter and primary production, many of which can be determined either directly or indirectly from ocean colour data. A major problem in coastal regions is eutrophication, which is the increased growth of phytoplankton due to excess nutrients enriching the water column. This growth in phytoplankton can severely alter the levels of oxygen, ultimately impacting the whole of the marine ecosystem. However, changes in the surface expression of phytoplankton biomass can be detected using ocean colour, so eutrophication can be monitored.

iv) Physical and Biological Processes - The mixing processes in the ocean transport phytoplankton and nutrients through the water column, bringing both into the surface layer where light is available for photosynthesis. Under the correct conditions, phytoplankton will grow, modifying the underwater light field and the rate of solar heating, which affects the stability and mixing processes of the water column. The feedback between the physical and biological processes can be

studied using ocean colour data, investigating the links between mixing and stratification on the phytoplankton spring bloom and phytoplankton phenology (Lee et al., 2010; Mahadevan et al., 2012; Racault et al., 2012).

Recommendations for Further Work

1. *Extend the methods developed in this study to different geographical regions and particle types.*

   The absorption partitioning procedure relies on the assumption that two materials, with differing absorption to backscattering ratios, driving the optical properties of the system. In this study, which focussed on the Irish Sea, these two materials were taken as phytoplankton cells and suspended mineral particles. However, there is scope for the identification of other particle classes which have different backscattering to absorption ratios, such as the highly scattering phytoplankton, coccolithophores. Application of the absorption partitioning procedure to new regions could therefore provide insights into the dynamics of multiple particle classes. In addition, further studies into the backscattering to absorption ratios of aggregated particles would be beneficial to investigate if these are distinguishable from finer suspended particles.

2. *Assimilation of satellite derived optical properties into shelf sea models.*

   As previously discussed, the assimilation of observational data into shelf sea hydrodynamic and ecosystem models is important to accurately predict and forecast the systems. Additionally, satellite derived properties could be used to validate existing models, such as the Proudman Oceanographic Laboratory Coastal Ocean Modelling System (POLCOMS) or NEMO, the Nucleus for European Modelling of the Ocean which was designed as a global ocean model.

3. *Investigation of the scope of these techniques when applied to planned hyperspectral satellite radiometers.*

   With the focus of future satellite missions on hyperspectral radiometers (NASA's Pre-Aerosol, Clouds and ocean Ecosystem, or PACE, mission), understanding the adaptability of current remote sensing methods is important. Additionally, there are opportunities for the development of new algorithms which make full use of the spectral information. The wavelength considered in this study was restricted to 488 nm for two reasons, firstly this waveband fell within the region of best performance of the QAA for the Irish Sea and secondly, it could be used subsequently to derive the euphotic depth. However, with hyperspectral radiometers there is potential for recovering the full absorption spectra for phytoplankton and mineral absorption. Additionally, the absorption partitioning procedure would benefit from accurate estimations of CDOM concentrations via remote sensing. Therefore, investigation of current CDOM algorithms and how these may be improved with hyperspectral measurements would be advantageous.

Bibliography

Aurin, D. A. and Dierssen, H. M. (2012). Advantages and limitations of ocean color remote sensing in CDOM-dominated, mineral-rich coastal and estuarine waters. *Remote Sensing of Environment*, 125(0):181 – 197.

Aurin, D. A., Dierssen, H. M., Twardowski, M. S., and Roesler, C. (2010). Optical complex in Long Island Sound and implications for coastal ocean color remote sensing. *J. Geophys. Res.*, 115(C07011). doi:10.1029/2009JC005837.

Babin, M., Stramski, D., Ferrari, G. M., Claustre, H., Bricaud, A., Obolensky, G., and Hoepffner, N. (2003). Variations in the light absorption coefficients of phytoplankton, nonalgal particles, and dissolved organic matter in coastal waters around Europe. *J. Geophys. Res.*, 108:254. doi:10.1029/2001JC000882.

Bailey, S. W. (2009). Radiometric corrections. http://oceancolor.gsfc.nasa.gov/forum/oceancolor/topic_show.pl?pid=12094;hl=551%20547.

Barnes, M. K., Tilstone, G. H., Smyth, T. J., Suggett, D. J., Astoreca, R., Lancelot, C., and Kromkamp, J. C. (2014). Absorption-based algorithm of primary production for total and size-fractionated phytoplankton in coastal waters. *Marine Ecology Progress Series*, 504:73–89.

Bisset, W. P., Schofield, O., Glenn, S., J., C., W., M., Plueddemann, A., and Mobley, C. D. (2001). Resolving the impacts and feedback of ocean optics on upper ocean ecology. *Oceanography*, 14:30–53.

Bowers, D., Ellis, K., and Jones, S. (2005). Isolated turbidity maxima in shelf seas. *Continental Shelf Research*, 25(9):1071 – 1080.

Bowers, D. and Mitchelson-Jacob, E. (1996). Inherent optical properties of the Irish Sea determined from underwater irradiance measurements. *Estuarine, Coastal and Shelf Science*, 43(4):433 – 447.

Bowers, D. G. (2003). A simple turbulent energy-based model of fine suspended sediments in the Irish Sea. *Continental Shelf Research*, 23:1495–1505.

Bowers, D. G., Boudjelas, S., and Harker, G. E. L. (1998). The distribution of fine suspended sediments in the surface waters of the Irish Sea and its relation to tidal stirring. *International Journal of Remote Sensing*, 19:2789–2805.

Bowers, D. G., Gaffney, S., White, M., and Bowyer, P. (2002). Turbidity in the southern Irish Sea. *Continental Shelf Research*, 22:2115–2126.

Bowers, D. G., Roberts, E. M., White, M., and Moate, B. D. (2013). Water masses, mixing, and the flow of dissolved organic carbon through the Irish Sea. *Continental Shelf Research*, 58:12–20.

Brewin, R. J., Sathyendranath, S., Muller, D., Brockmann, C., Deschamps, P.-Y., Devred, E., Doerffer, R., Fomferra, N., Franz, B., Grant, M., Groom, S., Horseman, A., Hu, C., Krasemann, H., Lee, Z., Maritorena, S., Melin, F., Peters, M., Platt, T., Regner, P., Smyth, T., Steinmetz, F., Swinton, J., Werdell, J., and III, G. N. W. (2013). The Ocean Colour Climate Change Initiative: III. A round-robin comparison on in-water bio-optical algorithms. *Remote Sensing of Environment*. In Press.

Bricaud, A., Babin, M., Morel, A., and Claustre, H. (1995). Variability in the

chlorophyll-specific absorption coefficients of natural phytoplankton: Analysis and parameterization. *J. Geophys. Res.*, 100:13321–13332.

Bricaud, A., Morel, A., Babin, M., Allali, K., and Claustre, H. (1998). Variations of light absorption by suspended particles with chlorophyll a concentration in oceanic (case 1) waters: Analysis and implications for bio-optical models. *Journal of Geophysical Research*, 103:31033–31044.

Capuzzo, E., Painting, S., Forster, R., Greenwood, N., Stephens, D., and Mikkelsen, O. (2013). Variability in the sub-surface light climate at ecohydrodynamically distinct sites in the North Sea. *Biogeochemistry*, 113(1-3):85–103.

Carder, K., Chen, R. F., Lee, Z. P., and Hawes, S. K. (1999). Semianalytical Moderate-Resolution Imaging Spectrometer algorithms for chlorophyll a and absorption with bio-optical domains based on nitrate-depletion temperatures. *Journal of Geophysical Research*, 104:5403–5421.

Carder, K., Hawes, S. K., Baker, K. A., Smith, R. C., Steward, R. G., and Mitchell, G. (1991). Reflectance model for quantifying chlorophyll a in the presence of productivity degradation products. *Journal of Geophysical Research*, 96:20,5999–20,611.

Chang, G., Barnard, A. H., and Zaneveld, J. R. V. (2007). Optical closure in a complex coastal environment: particle effects. *Appl. Opt.*, 46(31):7679–7692.

Chang, G. and Whitmire, A. (2009). Effects of bulk particle characteristics on backscattering and optical closure. *Optics Express*, 17(4):2132–2142.

Chen, Z., Hu, C., Conmy, R. N., Muller-Karger, F., and Swarzenski, P. (2007).

Colored dissolved organic matter in Tampa Bay, Florida. *Marine Chemistry*, 104:98 – 109.

Cherukuru, N., Brando, V. E., Schroeder, T., Clementson, L. A., and Dekker, A. G. (2014). Influence of river discharge and ocean currents on coastal optical properties. *Continental Shelf Research*, 84(0):188 – 203.

Cunningham, A., Ramage, L., and McKee, D. (2013). Relationships between the inherent optical properties and the depth of penetration of solar radiation in optically complex waters. *J. Geophys. Res.*, 118. doi:10.1002/jgrc20182.

Dall'Olmo, G. and Gitelson, A. (2005). Effect of bio-optical parameter variability on the remote estimation of chlorophyll-a concentration in turbid productive waters: Experimental results. *Appl. Opt.*, 44:412–422.

Doron, M., Babin, M., Mangin, A., and Hembise, O. (2007). Estimation of light penetration and horizontal and vertical visibility in oceanic and coastal waters from surface reflectance. *J. Geophys. Res.*, 112. doi: 10.1029/2006JC004007.

Druon, J.-N., Schrimpf, W., Dobricic, S., and Stips, A. (2004). Comparative assessment of large-scale marine eutrophication: North Sea area and Adriatic Sea as case studies. *Marine Ecology Progress Series*, 272:1–23.

Ellis, K., Binding, C., Bowers, D., Jones, S., and Simpson, J. (2008). A model of turbidity maximum maintenance in the Irish Sea. *Estuarine, Coastal and Shelf Science*, 76(4):765 – 774.

Feldman, G. C., Clark, D. K., and Halpern, D. (1984). Satellite color observations of the phytoplankton distribution in the eastern equatorial Pacific during the 1982-1983 El Nino. *Science*, 226:1069–1071.

Ferreira, A., Garcia, M. T., and Garcia, A. E. (2009). Light absorption by phytoplankton, nonalgal particles and dissolved organic matter at the Patagonia shelf-break in spring and summer. *Deep-Sea Research Part I*, 56:2162–2174.

Garver, S. A. and Siegel, D. A. (1997). Inherent optical property inversion of ocean color spectra and its biogeochemical interpretation 1. Time series from the Sargasso Sea. *Journal of Geophysical Research*, 102:18,607–18,625.

Gordon, H. R. (1973). Simple Calculation of the Diffuse Reflectance of the Ocean. *Appl. Opt.*, 12(12):2803–2804.

Gordon, H. R. (1989). Can the Lambert-Beer law be applied to the diffuse attenuation coefficient of ocean water? *Limnology and Oceanography*, 34:1389–1409.

Gordon, H. R., Brown, O. B., Evans, R. H., Brown, J. W., Smith, R. C., Baker, K. S., and Clark, D. K. (1988). A semianalytical radiance model of ocean color. *J. Geophys. Res.*, 93:10909–10924.

Gordon, H. R., Brown, O. B., and Jacobs, M. M. (1975). Computed relationships between the inherent and apparent optical properties of a flat homogeneous ocean. *Appl. Opt.*, 14(2):417–427.

Gordon, H. R. and Wang, M. (1994). Retrieval of water-leaving radiance and aerosol optical thickness over the oocean with SeaWiFS: a preliminary algorithm. *Appl. Opt.*, 33(3):443–452.

Gowen, R. J., Stewart, B. M., Mills, D. K., and Elliot, P. (1995). Regional differences in stratification and its effect on phytoplankton production and

biomass in the northwestern Irish Sea. *Journal of Plankton Research*, 17:753–769.

Gowen, R. J., Tett, P., Kennington, K., Mills, D. K., Shammon, T. M., Stewart, B. M., Greenwood, N., Flanagan, C., Devlin, M., and Wither, A. (2008). The Irish Sea: Is it euphotic? *Estuarine, Coastal and Shelf Science*, 76:239–254.

HOBILabs (2008). *HydroScat-2 Spectral Backscattering Sensor & Fluorometer: User's Manual*.

Howarth, M. J., Simpson, J. H., Sundermann, J., and van Haren, H. (2002). Processes of Vertical Exchange in Shelf Seas (PROVESS). *Journal of Sea Research*, 47:199–208.

IOCCG (2000). Remote Sensing of Ocean Colour in Coastal and Other Optically-Complex Waters. In Sathyendranath, S., editor, *Reports of the International Ocean-Colour Coordinating Group, No. 3*.

IOCCG (2006). Remote Sensing of Inherent Optical Properties: Fundamentals, Tests of Algorithms and Applications. In Lee, Z. P., editor, *Reports of the International Ocean-Colour Coordinating Group, No. 5*.

IOCCG (2008). Why Ocean Colour? The Societal Benefits of Ocean-Colour Technology. In Platt, T., Hoepffner, N., Stuart, V., and Brown, C., editors, *Reports of the International Ocean-Colour Coordinating Group, No. 7*.

Jin, J., Liu, S. M., Ren, J. L., Liu, C. G., Zhang, J., Zhang, G. L., and Huang, D. J. (2013). Nutrient dynamics and coupling with phytoplankton species composition during the spring blooms in the Yellow Sea. *Deep Sea Research Part II: Topical Studies in Oceanography*, 97(0):16 – 32.

Kirk, J. T. O. (1975a). A theoretical analysis of the contribution of algal cells to the attenuation of light wiwith natural waters I. Genral treatment of suspensions of pigmented cells. *New Phytol.*, 75:11–20.

Kirk, J. T. O. (1975b). A theoretical analysis of the contribution of algal cells to the attenuation of light wiwith natural waters II. Spherical cells. *New Phytol.*, 75:21–36.

Kirk, J. T. O. (1994). *Light and Photosynthesis in Aquatic Ecosystems*. Cambridge University Press.

Le, C., Hu, C., English, D., Cannizzaro, J., Chen, Z., Kovach, C., Anastasiou, C. J., Zhao, J., and Carder, K. L. (2013). Inherent and apparent optical properties of the complex estuarine waters of Tampa Bay: What controls light? *Estuarine, Coastal and Shelf Science*, 117(0):54 – 69.

Lee, Z. P. (2012). QAAv6. Personal Communication.

Lee, Z. P., Carder, K. L., and Arnone, R. A. (2002). Deriving inherent optical properties from water color: a multiband quasi-analytical algorithm for optically deep waters. *Appl. Opt.*, 41:5755–5772.

Lee, Z. P., Carder, K. L., and Arnone, R. A. (2009). An update of the quasi-analytical algorithm (QAA_v5). http://www.ioccg.org/groups/Software_OCA/QAA_v5.pdf.

Lee, Z. P., Carder, K. L., Mobley, C. D., Steward, R. G., and Patch, J. S. (1999). Hyperspectral remote sensing for shallow waters. 2. Deriving bottom depths and water properties by optimization. *Appl. Opt.*, 38:3831–3843.

Lee, Z. P., Darecki, M., Carder, K. L., Davis, C. O., Stramski, D., and Rhea, W. J. (2005a). Diffuse attenuation coefficient of downwelling irradiance: An evaluation of remote sensing methods. *J. Geophys. Res.*, 110. doi:10.1029/2004JC002573.

Lee, Z. P., Du, K. P., and Arnone, R. A. (2005b). A model for the diffuse attenuation coefficient of downwelling irradiance. *J. Geophys. Res.*, 110. doi:10.1029/2004JC002275.

Lee, Z. P., Du, K. P., Arnone, R. A., Liew, S. C., and Penta, B. (2005c). Penetration of solar radiation in the upper ocean: A numerical model for oceanic and coastal waters. *J. Geophys. Res.*, 110. doi:10.1029/2004JC002780.

Lee, Z. P., Hu, C., Shang, S., Du, K. P., Lewis, M., Arnone, R. A., and Brewin, R. (2013). Penetration of UV-visible solar radiation in the global oocean: Insights from ocean color remote sensing. *J. Geophys. Res.*, 118. doi:10.1002/jgrc.20308.

Lee, Z. P., Shang, S., Hu, C., Lewis, M., Arnone, R. A., Li, Y., and Lubac, B. (2010). Time series of bio-optical properties in a subtropical gyre: Implications for the evaluation of interannual trends of biogeochemical properties. *J. Geophys. Res.*, 115. doi:10.1029/2009JC005865.

Lee, Z. P., Weidemann, A., Kindle, J., Arnone, R. A., Carder, K., and Davis, D. (2007). Euphotic zone depth: Its derivation and implication to ocean-color remote sensing. *J. Geophys. Res.*, 112. doi:10.1029/2006JC003802.

Lewis, M., Carr, M., Feldman, G. C., Esaias, W., and McClain, C. (1990). Influence of penetrating solar radiation on the heat budget of the equatorial Pacific Ocean. *Nature*, 347:543 – 545.

Maffione, R. A. and Dana, D. R. (1997). Instruments and methods for measuring the backward-scattering coefficients of ocean waters. *Applied Optics*, 36(24):6057–6067.

Mahadevan, A., D'Asaro, E., Lee, C., and Perry, M. J. (2012). Eddy-driven stratificiation initiates North Atlantic spring phytoplankton blooms. *Science*, 337(54-58). doi:10.1126/science.1218740.

Maritorena, S., Siegel, D. A., and Peterson, A. R. (2002). Optimization of a semi-analytical ocean color model for global-scale applications. *Appl. Opt.*, 41(15):2705–2714.

McKee, D. and Cunningham, A. (2006). Identification and characterisation of two optical water types in the Irish Sea from in situ inherent optical properties and seawater constituents. *Estuarine, Coastal and Shelf Science*, 68:305–316.

McKee, D., Cunningham, A., and Dudek, A. (2007). Optical water type discrimination and tuning remote sensing band-ratio algorithms: Application to retrieval of chlorophyll and $K_d(490)$ in the Irish and Celtic Seas. *Estuarine, Coastal and Shelf Science*, 73:827–834.

McKee, D., Piskozub, J., and Brown, I. (2008). Scattering error correction for in situ absorption and attenuation measurements. *Optics Express*, 16(24):19480–19492.

McKee, D., Piskozub, J., Rottgers, R., and Reynolds, R. A. (2013). Evaluation and improvement of an iterative scattering correction scheme for in situ absorption and attenuation measurements. *Journal of Atmospheric and Oceanic Technology*, 30:1527–1541.

Mitchell, G. (1994). Coastal Zone Color Scanner retrospective. *J. Geophys. Res.*, 99:7291–7292.

Mobley, C. D. (1994). *Light and water: radiative transfer in natural waters*. Academic Press, San Diego, California.

Mobley, C. D. and Sundman, L. K. (2008). *HydroLight 5 EcoLight 5 User's Guide*. Sequoia Scientific Inc., Bellevue, U.S.A.

Morel, A. (1980). In-water and remote measurements of ocean color. *Boundary-Layer Meteorology*, 18:177–201.

Morel, A. and Prieur, L. (1977). Analysis of variations in ocean color. *Limnology and Oceanography*, 22(4):709–722.

Mueller, J. L. (2000). SeaWiFS algorithm for the diffuse attenuation coefficient K(490), using water-leaving radiances at 490 and 555 nm. In Hooker, S. and Firestone, E. R., editors, *NASA Technical Report Series*, volume 11, pages 24–27, NASA Goddard Space Flight Center, Greenbelt, Maryland.

NASA (1996). *Coastal Zone Color Scanner (CZCS) Instrument Guide*. http://disc.sci.gsfc.nasa.gov/oceans/documentation/scientific-documentation/CZCS_Sensor.gd.shtml.

Neil, C., Cunningham, A., and McKee, D. (2011). Relationships between suspended mineral concentration and red-waveband reflectances in moderately turbid shelf seas. *Remote Sens. Environ.*, 115:3719–3730.

Neil, C., Cunningham, A., McKee, D., and Polton, J. A. (2012). Remote sensing of seasonal stratificiation dynamics in the southern Irish Sea. *Remote Sens. Environ.*, 127:288–297.

Odermatt, D., Gitelson, A., Brando, V. E., and Schaepman, M. (2012). Review of constituent retrieval in optically deep and complex waters from satellite imagery. *Remote Sensing of Environment*, 118(0):116 – 126.

Oubelkheir, K., Clementson, L. A., Webster, I. T., Ford, P. W., Dekker, A. G., Radke, L. C., and Daniel, P. (2006). Using inherent optical properties to investigate biogeochemical dynamics in a tropical macrotidal coastal system. *Journal of Geophysical Research: Oceans*, 111(C7). doi:10.1029/2005JC003113.

Peeters, F., Haas, H. A., Peperzak, L., and de Vries, I. (1993). Nutrient and light as factors controlling phytoplankton biomass on the Dutch continental shelf (North Sea) in 1988-1990. DGW-93.004, The Hague.

Peeters, F., Kerimoglu, O., and Straile, D. (2013). Implications of seasonal mixing for phytoplankton production and bloom development. *Theoretical Ecology*, 6(2):115–129.

Piskozub, J., Stramski, D., Terril, E., and Kendall Melville, W. (2004). Influence of forward and multiple light scatter on the measurement of beam attenuation in highly scattering marine environments. *Appl. Opt.*, 43(24):4723–4731.

Platt, T., Sathyendranath, S., Caverhill, C. M., and Lewis, M. (1988). Ocean primarty production and available light: further algorithms for remote sensing. *Deep Sea Research*, 35(6):855–879.

Pope, R. M. and Fry, E. S. (1997). Absorption spectrum (380 - 700 nm) of pure water. II Integrating cavity measurements. *Applied Optics*, 36:8710–8723.

Preisendorfer, R. W. (1976). *Hydrologic Optics*, volume 5: Properties. National Technical Information Service, Springfield.

Racault, M., Le Quere, C., Buitenhuis, E., Sathyendranath, S., and Pla (2012). Phytoplankton phenology in the global ocean. *Ecological Indicators*, 14:152–163.

Robinson, I. S., Antoine, D., Darecki, M., Gorringe, P., L., P., Ruddick, K., Santoleri, R., Siegel, H., Patrick, V., Wernard, M. R., G., W., and Zibordi, G. (2008). Remote Sensing of Shelf Sea Ecosystems: State of the Art and Perspectives. Marine Board - European Science Foundation.

Roesler, C., Perry, M. J., and Carder, K. (1989). Modeling in situ phytoplankton absorption from total absorption spectra in productive inland marine waters. *Limnology and Oceanography*, 34(8):1510–1523.

Ruddick, K. G., Ovidio, F., and Rijkeboer, M. (2000). Atmospheric correction of SeaWiFS imagery for turbid coastal and inland waters. *Appl. Opt.*, 39(6):897–912.

Sathyendranath, S., Gouveia, A. D., Shetye, S. R., Ravindran, P., and Platt, T. (1991a). Biological control of surface temperature in the Arabian Sea. *Nature*, 349:54–56.

Sathyendranath, S. and Platt, T. (1988). The spectral irradiance field at the surface and in the interior of the ocean: A model for applications in oceanography and remote sensing. *Journal of Geophysical Research*, 93:9270–9280.

Sathyendranath, S., Platt, T., Caverhill, C. M., Warnock, R. E., and Lewis, M. (1989a). Remote sensing of oceanic primary prodution: computations using a spectral model. *Deep Sea Research*, 36(3):431–453.

Sathyendranath, S., Platt, T., Horne, E. P. W., Harrison, W., Ulloa, O., Outerbridge, R., and Hoepffner, N. (1991b). Estimation of new production in the ocean by compund remote sensing. *Nature*, 353:129–133.

Sathyendranath, S., Prieur, L., and Morel, A. (1989b). A three-component model of ocean colour and its application to remote sensing of phytoplankton pigments in coastal waters. *Int. J. Remote Sens.*, 10:1373–1394.

Simpson, J. (1997). Physical processes in the ROFI regime. *Journal of Marine Systems*, 12:3–15.

Simpson, J. and Bowers, D. (1981). Models of stratification and frontal movement in shelf seas. *Deep Sea Research Part A. Oceanographic Research Papers*, 28(7):727 – 738.

Simpson, J. and Hunter, J. (1974). Fronts in the Irish Sea. *Nature*, 250:404–406.

Smith, R. and Baker, K. (1982). Oceanic chlorophyll concentrations as determined by satellite (Nimbus-7 Coastal Zone Color Scanner). *Marine Biology*, 66(3):269–279.

Smith, R. C. and Baker, K. S. (1981). Optical properties of the clearest natural waters. *Appl. Opt.*, 20:177–184.

Song, D. and Wang, X. H. (2013). Suspended sediment transport in the Deepwater Navigation Channel, Yangtze River Estuary, China, in the dry season 2009: 2. Numerical simulations. *Journal of Geophysical Research: Oceans*, 118(10):5568–5590.

Stramski, D. and Piskozub, J. (2003). Estimation of scattering error in spec-

trophotometric measurements of light absorption by aquatic particles from three-dimensional radiative transfer simulations. *Appl. Opt.*, 42(18):3634–3646.

Stumpf, R. P., Arnone, R. A., Gould, R. W., Maritinolich, P. M., and Ransibrahmanakul, V. (2003). A partially coupled ocean-atmosphere model for retrieval of water-leaving radiance from SeaWiFS in coastal waters. Technical Report 22, NASA.

Sullivan, J. M., Twardowski, M. S., Zaneveld, J. R. V., Moore, C. M., Barnard, A. H., and Donaghay, P. L. a. (2006). Hyperspectral temperature and salt dependencies of absorption by water and heavy water in the 400-750 nm spectral range. *Applied Optics*, 45:5294–5309.

Tang, Z., Engel, B., Pijanowski, B., and Lim, K. (2005). Forecasting land use change and its environmental impact at a watershed scale. *Journal of Environmental Management*, 76(1):35 – 45.

Tilstone, G. H., Peters, S. W., van der Woerd, H. J., Eleveld, M. A., Ruddick, K., Schonfeld, W., Krasemann, H., Martinez-Vicente, V., Blondeau-Patissier, D., Rottgers, R., Sorensen, K., Jorgensen, P. V., and Shutler, J. D. (2012). Variability in specific-absorption properties and their use in a semi-analytical ocean colour algorithm for MERIS in North Sea and Western English Channel coastal waters. *Remote Sensing of Environment*, 118(0):320 – 338.

Tilstone, G. H., Smyth, T., Gowen, R. J., Martinez-Vicente, V., and Groom, S. (2005). Inherent optical properties of the Irish Sea and their effect on satellite primary production algorithms. *Journal of Plankton Research*, 27(11):1127–1148.

Vantrepotte, V., Brunet, C., Meriaux, X., Lecuyer, E., Vellucci, V., and Santer, R. (2007). Bio-optical properties of coastal waters in the Eastern English Channel. *Estuarine, Coastal and Shelf Science*, 72:201–212.

Wang, M., Son, S., and Harding Jr., L. W. (2009). Retrieval of diffuse attenuation coefficient in the Chesapeake Bay and turbid ocean regions for satellite ocean color applications. *J. Geophys. Res.*, 114. doi:10.1029/2006JC003802.

Weeks, A. and Simpson, J. H. (1991). The measurement of suspended particulate concentrations from remotely-sensed data. *International Journal of Remote Sensing*, 12(4):725–737. doi:10.1080/01431169108929689.

Werdell, P. J., Franz, B. A., Bailey, S. W., Feldman, G. C., Boss, E., Brando, V. E., Dowell, M., Hirata, T., Lavender, S. J., Lee, Z., Loisel, H., Maritorena, S., Mélin, F., Moore, T. S., Smyth, T. J., Antoine, D., Devred, E., d'Andon, O. H. F., and Mangin, A. (2013). Generalized ocean color inversion model for retrieving marine inherent optical properties. *Appl. Opt.*, 52(10):2019–2037.

WetLabs (2006). *ac-9 Plus User's Guide*.

Yentsch, C. (1960). The influence of phytoplankton pigments on the colour of sea water. *Deep Sea Research*, 7:1–9.

Zaneveld, J. R. V., Kitchen, J. C., and Moore, C. M. (1994). The scattering error correction of reflecting-tube absorption meters. *SPIE Ocean Optics XII*, 2258:44–55.

Zhao, J., Barnes, B., Melo, N., English, D., Lapointe, B., Muller-Karger, F., Schaeffer, B., and Hu, C. (2013). Assessment of satellite-derived diffuse atten-

uation coefficients and euphotic depths in south Florida coastal waters. *Remote Sens. Environ.*, 131:38–50.